

White Paper

Ver.1.0

Last Update: 2026 Mar. 11

CHRONOS Science Program

Yuki Inoue, Mario Juvenal S Onglao III, Vivek Kumar, Daiki Tanabe

on behalf of CHRONOS collaboration



Abstract

Cryogenic sub-Hz cROss torsion-bar detector with quantum NOn-demolition Speed meter(CHRONOS) is a proposed next-generation ground-based gravitational-wave observatory designed to explore the sub-Hz frequency band with unprecedented sensitivity. Utilizing a cryogenic torsion-bar interferometric configuration with quantum non-demolition speed-meter readout, CHRONOS targets a frequency window that bridges space-based missions and current high-frequency ground-based detectors, opening a new frontier in gravitational-wave astronomy. The observatory will enable long-duration tracking of compact binary inspirals well before merger, significantly improving source localization, parameter estimation, and tests of general relativity. In addition to transient signals, CHRONOS is optimized to probe the stochastic gravitational-wave background (SGWB) in the sub-Hz regime, providing powerful constraints on primordial gravitational waves, inflationary tensor spectra with red or blue tilts, first-order phase transitions, cosmic strings, and other relics of high-energy physics. By connecting gravitational-wave measurements across cosmological frequency scales—from cosmic microwave background polarization to pulsar timing arrays and high-frequency interferometers—CHRONOS will contribute to a coherent reconstruction of the gravitational-wave spectrum over more than twenty orders of magnitude. Crossing critical sensitivity thresholds in the sub-Hz band, CHRONOS will establish a new pillar of gravitational-wave astronomy and cosmology, enabling transformative advances in astrophysics and fundamental physics.

Acknowledgments

We thank S.Takano, M.Ando and T.Namikawa for providing the TOBA data and CMB data. We also thank K.W.Ng and M.Hazumi for their academic advice during the preparation of this manuscript. We thank M.Hasegawa, T.Kanayama, S.Matsushita, H.Murakami, M.Inoue, and R.Shibuya for support to establish CHRONOS team. Y.I. acknowledges support from NSTC, CHiP and Academia Sinica in Taiwan under Grant No.114-2112-M-008-006-, and No.AS-TP-112-M01.

Contents

Abstract	ii
Acknowledgements	iii
1 Overview of CHRONOS	1
1.1 Scientific Background and Objectives	1
1.2 Detection Principle	2
1.3 Optical Configuration	2
1.3.1 Noise Sources and Sensitivity	3
1.4 Development Strategy	3
1.5 Future Prospects	4
2 CHRONOS Collaboration	5
2.1 Definition and Purpose of the Collaboration	5
2.2 CHRONOS Science Program	6
2.3 Subsystem-Based Responsibility Allocation	7
2.4 Governance and Decision-Making Structure	8
2.4.1 Traceability and Strategic Coherence	10
2.5 Publication and Dissemination Policy	11
2.6 Membership and Expansion Policy	12
3 Gravitational Wave Science	15
3.1 Scientific Reach I: Intermediate-Mass Black Hole Binaries	17
3.2 Scientific Reach II: Stochastic Gravitational-Wave Background	19

3.3	Scientific Reach III: Quantum Measurement and Fundamental Physics . . .	22
3.4	Scientific Reach IV: Prompt Gravity Signals from Large Earthquakes . . .	26
4	Sensitivity	32
4.1	Principle	34
4.2	Quantum-noise description and physical interpretation	35
4.3	Bar Thermal Noise	40
4.3.1	Noise Model	41
4.3.2	Frequency Dependence in CHRONOS	42
4.3.3	Design Implications and Future Prospects	42
4.4	Coating Brownian noise	43
4.4.1	Interpretation based on the fluctuation–dissipation theorem . . .	43
4.4.2	Noise model	44
4.4.3	Frequency dependence and role in CHRONOS	44
4.4.4	Implications for coating development in CHRONOS	45
4.5	Seismic Noise	45
4.5.1	Coupling from Ground Motion to Rotational Noise	46
4.5.2	Role of Pre-Isolation and Suspension System	46
4.5.3	Underground Operation and Future Prospects	47
4.6	Rayleigh-wave Newtonian Noise	47
4.6.1	Gravitational Perturbation from Rayleigh Waves	48
4.6.2	Differential Gravity Gradient	49
4.6.3	Conversion to Torsional Angular Noise	49
4.6.4	Role in CHRONOS and Design Implications	50
5	CHRONOS Interferometer	52
5.1	Optical layout	52
5.1.1	Triangular Sagnac ring cavity	55
5.1.2	Coupling between the torsion bar and the ring cavities	56
5.1.3	Dual-recycling configuration with PR-dominated operation . . .	57
5.2	Torsion bar	58
6	Cavity Control	61
6.1	Operation method	61

6.1.1	Sideband Frequencies and Frequency Architecture	62
6.1.2	RF Sidebands and Degree-of-Freedom Separation	63
6.1.3	Input Mode Cleaner (IMC) Compatibility	64
6.1.4	Design Philosophy Summary	64
6.1.5	Control ports and control scheme	65
7	Input Optics	71
7.1	Pre-Mode Cleaner (PMC)	73
7.1.1	Scientific Role of the PMC	73
7.1.2	Pound–Drever–Hall Frequency Discrimination	75
7.1.3	Optical and Mechanical Parameters	76
7.1.4	Thermal Stability Considerations	76
7.1.5	Importance for Sub-Hz Operation	77
7.2	Intensity Stabilization	77
7.2.1	Physical Coupling of Intensity Noise	77
7.2.2	Intensity Stabilization Architecture	78
7.2.3	Optical-Follower Servo (OFS)	79
7.2.4	Control Loop Characteristics	79
7.2.5	Noise Suppression Performance	80
7.2.6	Role in Sub-Hz Speed-Meter Operation	81
7.3	Frequency Stabilization	81
7.3.1	Reference Cavity as Absolute Frequency Standard	82
7.3.2	Multi-Stage Control Hierarchy	84
7.3.3	Frequency Noise Requirement for CHRONOS	84
7.3.4	Importance for Sub-Hz Speed-Meter Sensitivity	85
7.4	Summary of the Input Optics	85
8	Output Optics	87
8.1	Purpose	87
8.2	Output Mode Cleaner	88
8.2.1	Principle	88
8.2.2	Higher Order Mode Suppression	89
8.2.3	Optical Design	90

8.2.4	Future Upgrade	91
8.3	Balanced Homodyne Detection	92
8.3.1	Principle	92
8.3.2	Readout Angle	92
8.3.3	Optical Design	93
8.3.4	Future Upgrade	94
9	Cryogenic System	95
9.1	Cryocooler and Heat Link	96
9.2	Cryogenic Performance	99
9.2.1	Active Vibration Isolation System	101
9.2.2	Photosensors	104
9.2.3	Piezoelectric Actuators	107
9.2.4	Control and Transfer Function	109
9.2.5	Noise Performance	110
10	Mirror Coating	113
10.1	Introduction	113
10.2	High-Low Dielectric Multilayer Coatings	115
10.2.1	Fresnel reflection at a single interface	115
10.2.2	Quarter-wave ($\lambda/4$) design	116
10.2.3	Transfer matrix formalism	116
10.2.4	Ideal quarter-wave stack	118
10.3	LPCVD fabrication	119
10.3.1	Growth Kinetics and Surface-Reaction Control	119
10.4	Material: a-Si, SiN, SiON	120
10.4.1	Material-Specific LPCVD Processes	121
11	Data analysis	125
11.1	Data Processing Framework	125
11.2	Compact Binary Coalescence (CBC) Analysis	127
11.2.1	Detector response and data model	127
11.2.2	Signal-to-noise ratio and matched filtering	128
11.2.3	SNR accumulation in the sub-Hz regime	129

11.2.4	Scientific implications for CHRONOS	130
11.3	Stochastic Gravitational-Wave Background (SGWB) Analysis	131
11.3.1	Statistical Description of the SGWB	131
11.3.2	Correlation-Based Detection Principle	132
11.3.3	General Correlation Estimator	134
11.3.4	Expectation Value and Relation to Ω_{GW}	135
11.3.5	Variance and Optimal Filtering	137
11.3.6	Cross-Correlation Between Independent Detectors	138
11.3.7	Internal Correlation Within a Detector	140
11.3.8	Systematic Effects and Correlated Noise	141
11.3.9	Application to CHRONOS	143
12	Calibration and Reconstruction	145
12.1	Gravitational Wave Strain	145
12.2	Model	147
12.3	Photon Calibrator	148
12.3.1	Optical configuration	151
12.3.2	Sensitivity comparison	153
12.4	Torque-coupled Gravitational Calibrator (GCal)	157
12.5	Reconstruction	164
12.5.1	Front-end (online) pipeline	165
12.5.2	High-latency (offline) pipeline	165
12.6	Error estimation	166
12.6.1	Residual response function	166
13	Cosmology	168
13.1	Basic principle of the analysis	169
13.1.1	Transfer function in radiation- and matter-dominated eras	171
13.2	Cosmological model and assumptions	172
13.2.1	Blue-tilted tensor spectrum	173
13.3	Observables	174
13.3.1	Bayesian framework and data combination	176
13.3.2	Sensitivity and statistical uncertainty	177

Contents

13.3.3 Likelihood for stochastic gravitational-wave constraints	178
13.3.4 Parameter inference	179
13.4 Conclusion	180
14 Summary	182

Overview of CHRONOS

1.1 Scientific Background and Objectives

The direct detection of gravitational waves from compact binary mergers by Advanced LIGO and Advanced Virgo [5, 1, 8] has opened a new observational window in astronomy and fundamental physics. KAGRA has further extended the global detector network into cryogenic interferometry [11]. Current ground-based detectors primarily operate above 10 Hz, while the future space-based observatory LISA will explore the millihertz band [15]. The intermediate sub-Hz band (0.1–10 Hz), located between these regimes, remains largely unexplored due to seismic noise, Newtonian noise, and suspension thermal noise [50].

Cryogenic sub-Hz cROss torsion-bar detector with quantum NOn-demolition Speed-meter (CHRONOS) [57] is a novel gravitational-wave detector concept designed to observe this unexplored frequency band from the ground. The project aims to bridge the observational gap between space-based detectors and kilometer-scale interferometers, enabling the detection of intermediate-mass black hole binaries, the early inspiral phase of stellar-mass binaries, and the stochastic gravitational-wave background [95]. The detail of project is explained on Inoue *et al.* [57].

1.2 Detection Principle

CHRONOS is based on the torsion-bar antenna concept [16, 75, 57, 58]. Unlike Michelson-type interferometers, which measure translational displacement, a torsion-bar detector measures relative angular motion. Several terrestrial efforts specifically target this regime, such as the torsion-bar antenna (TOBA) [16] and the Torsion Pendulum Dual Oscillator (TorPeDO) [75], both of which have demonstrated proof-of-principle operation of sub-hertz detectors. By exploiting the torsional degree of freedom, the mechanical resonant frequency can be significantly reduced, naturally extending sensitivity toward the sub-Hz regime.

The test masses are supported by a low-loss suspension system and operated under cryogenic conditions, which suppress thermal noise. The minute rotational motion induced by gravitational waves is read out interferometrically.

A key feature of CHRONOS is the adoption of a speed-meter-type interferometer realizing quantum non-demolition (QND) measurement [27, 35, 58]. In conventional position measurements, radiation-pressure noise dominates at low frequencies; however, in a speed-meter configuration that measures velocity, quantum back-action is significantly suppressed. This enables improved quantum noise performance in the low-frequency regime.

1.3 Optical Configuration

The CHRONOS detector employs a triangular Sagnac interferometer combined with power-recycling and signal-recycling cavities, as developed for advanced interferometers [76, 78, 58]. In the Sagnac topology, counter-propagating beams sample the test-mass motion at different times, naturally realizing a speed-meter response [27].

The optical design is guided by three primary requirements:

- quantum-noise optimization via power recycling detuning and homodyne detection angle,
- suppression of higher-order modes through cavity geometry control.

This integrated optical configuration enables high-sensitivity measurements within a compact experimental footprint of approximately $10\text{ m} \times 10\text{ m}$.

1.3.1 Noise Sources and Sensitivity

The sub-Hz sensitivity is limited by:

- quantum noise,
- suspension and substrate thermal noise,
- coating thermal noise,
- seismic noise,
- Newtonian noise

Newtonian noise represents a particularly severe limitation in the sub-Hz band [50]. The adoption of a speed-meter configuration suppresses radiation-pressure noise at low frequencies [35]. Cryogenic operation further reduces thermal noise.

The projected strain sensitivity approaches

$$h \sim 1 \times 10^{-18} \text{ Hz}^{-1/2}$$

around 2 Hz.

1.4 Development Strategy

The CHRONOS project adopts a stepwise development strategy. A system validates optical design, noise modeling, and calibration techniques. Subsequently, a larger-scale cryogenic system demonstrates suspension and thermal performance. This phased approach follows the successful path taken by advanced interferometers [1].

1.5 Future Prospects

CHRONOS will open a new observational window in the sub-Hz band, complementing both ground-based and space-based detectors [15]. This enables multi-band gravitational-wave astronomy [95] and long-duration tracking of compact binaries.

The cryogenic precision-measurement technologies and speed-meter interferometry developed here represent a technological stepping stone toward next-generation gravitational-wave observatories.

CHRONOS Collaboration

2.1 Definition and Purpose of the Collaboration

The CHRONOS Collaboration is established as an integrated implementation framework to execute the CHRONOS Science Program described in this White Paper.

All research activities, experimental planning, subsystem development, integration testing, and performance evaluations conducted under this collaboration shall be carried out in accordance with the scientific objectives, technical requirements, and milestones defined in the CHRONOS Science Program.

The collaboration does not function as a collection of independent research projects; rather, it operates as a responsibility-based governance structure designed to systematically and progressively realize the scientific roadmap.

Its objectives are summarized as follows:

- Ensuring consistency between implementation activities and scientific objectives
- Clearly defining responsibilities at the subsystem level
- Establishing a sustainable governance framework with future international expansion in view

This chapter defines the governance structure and decision-making framework of the collaboration.

2.2 CHRONOS Science Program

The CHRONOS Science Program serves as the scientific guideline and the highest-level foundational document of the collaboration.

This White Paper is positioned as the official document defining the scientific objectives, technical requirements, phased milestones, and long-term research vision. All implementation activities and decision-making processes shall be conducted in accordance with this White Paper.

(1) Revision of the White Paper

The White Paper may be revised in response to scientific progress or strategic necessity.

Revisions are classified into Minor Updates and Major Updates according to their scope and impact.

Minor Update Clarifications of technical specifications, editorial refinements, or minor adjustments to milestones that do not alter the fundamental scientific objectives shall be classified as Minor Updates.

Minor Updates shall be reviewed and approved by the Management Meeting.

Major Update Modifications involving changes to scientific objectives, addition of new research domains, or substantial alterations to the experimental configuration shall be classified as Major Updates.

Major Updates shall be scientifically reviewed and discussed during the Internal Session of the annual CHRONOS International Workshop, and approved upon consensus.

If necessary, final confirmation may subsequently be conducted at the Management Meeting.

Revision Record and Publication All revisions shall be assigned a version number and issue date, and the changes shall be clearly documented.

The latest version of the White Paper shall be published on the official CHRONOS website (<http://chronos.phy.ncu.edu.tw>) to ensure transparency and international credibility.

(2) Transparency and Public Availability

The latest version of the White Paper shall be made publicly available on the official CHRONOS website (<http://chronos.phy.ncu.edu.tw>).

This ensures transparency of scientific objectives and governance principles, and strengthens the foundation for international research collaboration.

2.3 Subsystem-Based Responsibility Allocation

To ensure clarity of accountability, research and implementation activities are structured at the subsystem level.

Each subsystem shall designate a Subsystem Lead responsible for design coordination, development planning, implementation management, performance verification, and progress reporting.

The lead institution shall be responsible for:

- Design and maintenance of the overall experimental architecture
- Definition of interfaces between subsystems
- Oversight of system integration and integration testing
- Verification of alignment with the CHRONOS Science Program

Each participating institution shall assume responsibility for its assigned subsystem, including:

- Definition of subsystem design and technical specifications

- Development schedule planning and management
- Reporting of milestone progress
- Submission of performance evaluation and validation data

Major subsystem milestones shall be reviewed during Weekly Meetings and formally evaluated at the annual CHRONOS International Workshop. Significant design or specification changes require approval by the Management Meeting.

This responsibility structure enables institutions to contribute according to their expertise while ensuring overall system coherence and accountability.

2.4 Governance and Decision-Making Structure

The collaboration operates under a three-tier governance structure that clearly separates operational management, strategic alignment, and executive decision-making.

(1) Weekly Meeting (Operational Level)

The Weekly Meeting serves as the operational coordination body responsible for routine technical adjustments and progress management.

Its primary roles include:

- Monitoring progress of each subsystem
- Sharing milestone status updates
- Verifying interface consistency
- Identifying technical issues and determining provisional responses

While the Weekly Meeting enables agile decision-making, modifications affecting scientific objectives or major specifications require approval at higher governance levels.

(2) CHRONOS International Workshop (Strategic Level)

The CHRONOS International Workshop is held annually and serves as the forum for scientific alignment and long-term strategic review.

The Workshop consists of two components:

- **Internal Session** Detailed technical reviews, milestone evaluations, roadmap updates, and planning for the subsequent year are conducted among collaboration members.
- **Open Session** A public session dedicated to dissemination of results, academic exchange with the international community, and exploration of potential future collaborations.

Alignment with the scientific objectives defined in the White Paper is reviewed annually at the Workshop.

(3) Management Meeting (Executive Level)

The Management Meeting serves as the highest decision-making body of the collaboration.

It consists of the Principal Investigator (PI) and Board Members.

Board Members are elected from among the collaboration participants. Approval of members is conducted at the Management Meeting.

Its primary authorities include:

- Allocation of budget and resources
- Approval of major design changes
- Final decisions on schedule adjustments
- Determination of risk mitigation policies
- Approval of new participating institutions
- Approval of Minor Updates to the White Paper

- Decisions regarding suspension or termination of membership in cases of policy violations

Decision-making shall, in principle, be based on consensus, with majority voting applied when necessary.

This three-tier structure ensures operational agility, strategic coherence, and clear accountability.

2.4.1 Traceability and Strategic Coherence

All research and development activities shall remain traceable to the scientific objectives and milestones defined in the CHRONOS Science Program.

Each subsystem shall establish development plans aligned with corresponding scientific objectives and performance requirements. Progress shall be reported based on quantitative indicators and technical evaluations.

To ensure traceability:

- The mapping between subsystems and scientific objectives shall be explicitly defined
- Achievement criteria shall be specified for each milestone
- Systematic annual reviews shall be conducted at the Workshop
- Significant specification changes shall be documented and formally approved

If design modifications or planning revisions are required, their scientific impact shall be evaluated and alignment with the CHRONOS Science Program confirmed before approval by the Management Meeting.

This framework ensures that independent institutional activities converge toward unified scientific objectives.

2.5 Publication and Dissemination Policy

The collaboration adopts a clear Publication Policy to ensure transparency, fairness, and scientific integrity.

(1) Opt-in Authorship Principle

Authorship of journal publications and international conference presentations shall be granted to members who have made substantial intellectual or technical contributions and who explicitly opt in to participate in manuscript preparation and submission.

The collaboration does not adopt an automatic inclusive authorship model, but instead follows a contribution-based opt-in principle.

(2) Internal Review Procedure

Prior to submission, manuscripts shall be circulated internally to verify:

- Technical validity
- Consistency with the CHRONOS Science Program
- Compliance with intellectual property and confidentiality requirements

Revisions shall be made as necessary before submission.

(3) Definition and Publication of Official Outputs

Peer-reviewed publications and official presentations shall be recognized as official outputs of CHRONOS.

These outputs shall be published on the CHRONOS website to ensure international visibility and transparency.

(4) Intellectual Property and Publication Restrictions

If intellectual property protection or confidentiality considerations apply, appropriate protective measures shall be taken prior to public disclosure. Publication timing may be adjusted when necessary.

This policy ensures equitable recognition of contributions while maintaining credibility as an international collaboration.

(5) Suspension and Termination of Membership

To maintain fairness and transparency, the collaboration defines procedures for addressing violations of its policies.

Corrective measures may apply in cases of:

- Significant violations of governance or publication policies
- Breach of confidentiality obligations
- Scientific misconduct
- Persistent failure to fulfill responsibilities

Upon confirmation of a violation, a written warning shall first be issued, providing an opportunity for correction.

If corrective actions are not taken, or in cases of serious violations, the Management Meeting may decide to suspend or terminate membership.

All such decisions shall be formally documented and implemented in accordance with governance principles.

2.6 Membership and Expansion Policy

The collaboration adopts a structured participation model designed to maintain governance integrity while enabling future international expansion.

(1) Eligibility for Participation

Institutions or researchers may apply to join the collaboration if they:

- Demonstrate alignment with the CHRONOS Science Program
- Agree to the governance and Publication policies
- Present a clearly defined technical or scientific contribution plan

(2) Approval Process

Applications shall be evaluated based on the proposed contribution and subsystem alignment, and approved by the Management Meeting.

Provisional participation may be granted when appropriate.

(3) Rights and Responsibilities of Members

Members have the right to:

- Participate in relevant meetings
- Opt in to publications and presentations
- Access shared information platforms

Members are obligated to:

- Contribute substantively toward scientific objectives
- Report milestone progress
- Comply with confidentiality and Publication policies

(4) Scalability and Sustainability

This framework is designed with future multinational expansion in mind. By maintaining subsystem-based responsibility and a three-tier governance structure, the col-

laboration preserves operational efficiency and strategic coherence even as the number of participating institutions increases.

Gravitational Wave Science

CHRONOS is an interferometric gravitational-wave detector designed to enable observations in the previously unexplored frequency band of 0.1–10 Hz, thereby filling the observational gap between existing and planned gravitational-wave detectors. Current observations span two major regimes: the millihertz band targeted by the space-based mission LISA [15], and the tens-of-hertz band observed by ground-based detectors such as Advanced LIGO, Advanced Virgo, and KAGRA [5, 1, 8, 11].so The intermediate sub-Hz band remains largely inaccessible due to seismic and Newtonian noise limitations By opening this frequency window, CHRONOS introduces a new observational domain in gravitational-wave astronomy [57, 58].

The first science goal is the observation of intermediate-mass black hole (IMBH) binaries [57]. IMBHs bridge the gap between stellar-mass and supermassive black holes, yet their formation mechanisms and population remain poorly understood [77]. The sub-Hz band corresponds to the late inspiral phase of IMBH binaries with total masses of 10^2 – $10^4 M_{\odot}$. CHRONOS enables multi-band gravitational-wave observations, linking LISA and ground-based detectors [95]. Such multi-band measurements provide precise parameter estimation, improved sky localization, and stringent constraints on black hole formation channels.

The second science goal is the search for the stochastic gravitational-wave background (SGWB) [57]. The SGWB arises from the superposition of unresolved astrophysical sources and potentially from processes in the early Universe [73]. Cosmological mechanisms such as first-order phase transitions and cosmic strings can generate gravitational waves peaking in the sub-Hz regime [24]. Ground-based detectors have placed

upper limits on the SGWB at higher frequencies [7]. By extending sensitivity into the sub-Hz band, CHRONOS probes a complementary portion of the spectrum. Joint observations with LISA and terrestrial detectors would enable broadband reconstruction of the gravitational-wave background energy density spectrum, providing a unique probe of early-Universe physics.

The third science goal concerns fundamental physics and quantum measurement [57]. The sensitivity of gravitational-wave interferometers is limited by quantum noise, and surpassing the standard quantum limit (SQL) is a central objective for next-generation detectors [19, 35]. CHRONOS adopts a speed-meter interferometer configuration [27], which suppresses quantum back-action at low frequencies. Demonstrating quantum non-demolition (QND) measurements in the sub-Hz band would constitute an experimental test of quantum measurement on macroscopic mechanical systems. Beyond its immediate impact on CHRONOS, this achievement would inform the design of future low-frequency gravitational-wave observatories.

The fourth science goal is the observation of prompt gravitational signals associated with large earthquakes [57]. Rapid mass redistribution during seismic events induces changes in the gravitational potential that propagate at the speed of light, preceding the arrival of elastic waves. Such signals have been theoretically predicted and discussed as potential early-warning probes [79]. By detecting these gravity perturbations, CHRONOS could enable earthquake detection prior to the arrival of destructive surface waves. This research also improves understanding of low-frequency gravity-gradient noise, which directly impacts sub-Hz detector design.

These four science goals are interconnected through a shared observational band and a common measurement principle. IMBH observations and SGWB searches advance astrophysics and cosmology, while quantum measurement studies extend the foundations of precision interferometry. Observations of earthquake-induced gravity signals provide insight into terrestrial gravity fluctuations that are directly relevant to low-frequency detectors. In this sense, CHRONOS integrates gravitational-wave astronomy, cosmology, fundamental physics, and geophysics within a unified experimental framework.

3.1 Scientific Reach I: Intermediate-Mass Black Hole Binaries

The first major science goal of CHRONOS is the observation of gravitational waves emitted from IMBH binaries. IMBHs are expected to occupy the mass range of 10^2 – $10^5 M_\odot$, bridging the gap between stellar-mass black holes and the supermassive black holes found at galactic centers. However, both electromagnetic and gravitational-wave observations to date have left significant uncertainties regarding their population and formation mechanisms [77, 47]. IMBHs may form through hierarchical mergers in dense stellar clusters or originate as direct-collapse black hole seeds in the early Universe, but observational evidence remains limited. Constraining the IMBH population is therefore a key step in understanding black hole formation and galaxy evolution.

CHRONOS is designed to achieve high sensitivity in the 0.1–10 Hz frequency band, which corresponds to the gravitational-wave signals emitted by IMBH binaries during the late inspiral phase prior to merger. The characteristic gravitational-wave frequency at the innermost stable circular orbit scales as $f_{\text{ISCO}} \propto M^{-1}$, placing binaries with total mass $M \sim 10^4$ – $10^5 M_\odot$ in the sub-Hz regime as shown in Fig 3.1 [74]. This band lies between the low-frequency regime probed by LISA [15] and the high-frequency regime observed by ground-based detectors such as LIGO and Virgo. CHRONOS thus enables multi-band gravitational-wave observations, in which a single source is tracked continuously across distinct frequency ranges [95].

Such multi-band observations significantly improve parameter estimation, including mass, spin, luminosity distance, and sky localization, and provide stringent tests of general relativity through consistency checks of inspiral-merger-ringdown waveforms.

Figure 3.2 shows the detectable luminosity distance for IMBH binaries as a function of total mass, assuming the design sensitivity of CHRONOS. The signal-to-noise ratio (SNR) is computed using the standard matched-filter formalism [39, 74],

$$\text{SNR}^2 = 4 \int_{f_{\text{min}}}^{f_{\text{max}}} \frac{|\tilde{h}(f)|^2}{S_n(f)} df,$$

where $\tilde{h}(f)$ is the frequency-domain waveform and $S_n(f)$ is the one-sided noise power spectral density. The sensitivity peaks in the mass range $M \sim 10^4\text{--}10^5 M_\odot$, where the merger frequency enters the sub-Hz band. For example, a 300 m-scale configuration is expected to detect binaries of $M \sim 4 \times 10^4 M_\odot$ out to approximately 80 Mpc at $\text{SNR} = 3$.

The low-frequency sensitivity of CHRONOS is enabled by a speed-meter interferometer implementing QND measurement [27, 35]. In displacement-based interferometers, quantum radiation-pressure noise dominates at low frequencies, leading to the sSQL. By measuring velocity rather than position, the quantum back-action contribution is suppressed, preserving sensitivity in the sub-Hz regime.

Maintaining QND performance requires careful optical cavity design. Increasing finesse enhances storage time but increases coating thermal noise and optical loss. Instead, CHRONOS extends the effective arm length to realize the required time delay with fewer reflections, reducing coating-induced dissipation while preserving low-frequency quantum performance.

In gravitational-wave searches, a standalone detection typically requires $\text{SNR} \sim 8$ for high-confidence identification. However, CHRONOS operates within a global network context. When prior information on source parameters is available from LISA or ground-based detectors, the parameter space volume is significantly reduced, allowing subthreshold signals to contribute to Bayesian inference and population studies [106]. Signals with $\text{SNR} \sim 1$ can therefore provide statistically meaningful information when incorporated into joint analyses.

The mass distribution and redshift evolution of IMBH binaries directly constrain black hole seed formation scenarios and hierarchical merger models [77, 47]. By probing the unexplored sub-Hz band, CHRONOS provides the missing link between LISA and LIGO, establishing a continuous observational pathway from early inspiral to final merger. In this sense, CHRONOS plays a pivotal role in the development of true multi-band gravitational-wave astronomy.

3.2 Scientific Reach II: Stochastic Gravitational-Wave Background

The second scientific objective of CHRONOS is the search for the SGWB. The SGWB is a statistical gravitational-wave signal formed by the superposition of many independent sources. While individual events cannot be resolved, it can be observed through its energy-density spectrum. The SGWB reflects the integrated history of astrophysical activity in the Universe and may also contain signatures of new physics from the early Universe, making it a key target in both gravitational-wave astronomy and cosmology.

Astrophysical sources of the SGWB include unresolved mergers of binary black holes and neutron stars, as well as the formation and evolution of supermassive black-hole binaries. These produce a broadband, continuous background from the overlap of many sub-threshold events. In contrast, cosmological SGWB sources may arise from first-order phase transitions, cosmic strings, inflationary tensor perturbations, or primordial black-hole formation, offering potential probes of physics beyond the Standard Model. The sub-Hz band is particularly important, as many of these cosmological signals are expected to peak in this frequency range, which remains largely unexplored.

CHRONOS is designed to achieve sensitivity to the SGWB in the frequency band of 0.1–10 Hz. This band lies between the mHz range probed by LISA and the ~ 10 Hz band observed by ground-based detectors such as LIGO, and thus plays a crucial role in bridging the gravitational-wave spectrum. Since the spectral shape of the SGWB strongly depends on its origin, multi-band observations are essential for disentangling astrophysical and cosmological contributions.

Figure 3.3 shows the projected energy-density sensitivity $\Omega_{\text{GW}}(f)$ of CHRONOS assuming five years of observation. The figure includes predictions for CHRONOS, along with current observational constraints such as LIGO O3, LISA Pathfinder, CMB B-mode polarization, CMB lensing, and the Sachs–Wolfe effect. Representative theoretical models—such as those from cosmic strings, primordial gravitational waves, and primordial black-hole formation—are also shown for comparison.

CHRONOS is expected to reach a sensitivity of $\Omega_{\text{GW}} \sim 3 \times 10^{-4}$ around $f \sim 2$ Hz. This corresponds to providing new direct constraints in a previously unexplored frequency band. In particular, signals from first-order phase transitions and cosmic strings often exhibit characteristic spectra in the sub-Hz range, and CHRONOS has the potential to place significant observational constraints on these models.

In SGWB searches, a key element is not only the sensitivity of a single detector but also cross-correlation analysis between multiple detectors. Because the SGWB is intrinsically stochastic, it must be distinguished from detector-specific noise by extracting correlated signals observed in independent instruments. CHRONOS may share its frequency band with TOBA-type detectors and future atom-interferometer-based GW detectors, and cross-correlation with these systems can significantly enhance the reliability of SGWB detection. Furthermore, by bridging the frequency ranges of LISA and ground-based interferometers, CHRONOS enables broadband reconstruction of the SGWB spectrum [57].

CHRONOS also plays an important role in probing astrophysical SGWB sources. In particular, intermediate-mass black-hole (IMBH) binaries and high-mass black-hole binaries emit long-duration signals in the sub-Hz band, and a large number of unresolved events may contribute to a stochastic background. Measuring this background provides independent constraints on black-hole formation rates and mass functions, offering statistical information complementary to individual event detections.

In this way, CHRONOS explores the SGWB in the previously uncharted frequency band between LISA and ground-based detectors, opening a new observational window for both astrophysics and cosmology. In particular, the search for primordial GW backgrounds offers a direct probe of early-Universe physics inaccessible to electromagnetic observations, and CHRONOS represents a crucial step toward this goal.

Astrophysical sources of the SGWB include unresolved mergers of binary black holes and neutron stars [7], as well as the cosmic population of supermassive black-hole binaries [94]. These produce a broadband background from the overlap of sub-threshold events. In contrast, cosmological SGWB sources may arise from first-order phase transitions [24], cosmic strings [115], inflationary tensor perturbations [61], or primordial black-hole formation. The sub-Hz band is particularly important, as many early-

Universe mechanisms predict peak frequencies in this regime.

CHRONOS is designed to achieve sensitivity to the SGWB in the frequency band of 0.1–10 Hz [57]. This band lies between the mHz range probed by LISA [15] and the ~ 10 Hz band observed by ground-based detectors such as LIGO and Virgo [7]. Because the spectral shape of $\Omega_{\text{GW}}(f)$ depends strongly on its physical origin, multi-band observations are essential for distinguishing astrophysical from cosmological contributions.

The stochastic background is quantified by

$$\Omega_{\text{GW}}(f) = \frac{1}{\rho_c} \frac{d\rho_{\text{GW}}}{d \ln f}, \quad (3.1)$$

where ρ_c is the critical energy density of the Universe [73]. Figure 3.3 shows the projected energy-density sensitivity of CHRONOS assuming five years of observation. The sensitivity estimate follows the standard cross-correlation formalism [14], in which the detectable Ω_{GW} scales with observation time as $T^{-1/2}$.

The projected CHRONOS sensitivity reaches $\Omega_{\text{GW}} \sim 3 \times 10^{-4}$ at $f \sim 2$ Hz. For comparison, LIGO O3 places upper limits of order $\Omega_{\text{GW}} \sim 10^{-9}$ – 10^{-8} near 25 Hz [7], while CMB observations constrain inflationary backgrounds at $f \sim 10^{-17}$ Hz through B-mode polarization. The sub-Hz regime remains largely unconstrained, and CHRONOS provides the first direct access to this frequency window.

In SGWB searches, cross-correlation between independent detectors is essential for distinguishing stochastic signals from instrumental noise [14]. Future TOBA-type detectors [16] and atom-interferometric gravitational-wave detectors [46] may operate in overlapping frequency bands, allowing correlated measurements that significantly enhance detection confidence. By bridging the frequency ranges of LISA and terrestrial interferometers, CHRONOS enables broadband reconstruction of the SGWB spectrum.

CHRONOS also probes the astrophysical SGWB generated by unresolved intermediate-mass black hole binaries. Population models predict that high-mass systems produce extended inspiral signals in the sub-Hz band, which may overlap to form a confusion

background [94]. Measuring this background provides statistical constraints on black-hole formation rates and mass functions, complementing individual event detections.

CHRONOS also probes the astrophysical SGWB generated by unresolved intermediate-mass black hole binaries. Population models predict that high-mass systems produce extended inspiral signals in the sub-Hz band, which may overlap to form a confusion background [94]. Measuring this background provides statistical constraints on black-hole formation rates and mass functions, complementing individual event detections.

3.3 Scientific Reach III: Quantum Measurement and Fundamental Physics

The third scientific objective of CHRONOS is to demonstrate quantum measurement with a macroscopic-scale interferometer operating in a regime limited by quantum noise, and to establish new measurement principles for gravitational-wave observation.

The sensitivity of gravitational-wave interferometers is fundamentally limited by quantum noise [26, 19]. At high frequencies photon shot noise dominates, while at low frequencies radiation-pressure noise becomes the primary limitation. Both originate from the quantum uncertainty inherent in continuous measurement. Traditionally, a trade-off between measurement imprecision and back-action is expressed as

$$S_x^{\text{imp}}(\Omega) S_F^{\text{BA}}(\Omega) \geq \hbar^2, \quad (3.2)$$

leading to the so-called SQL [19]. The SQL has long been regarded as the fundamental sensitivity limit of interferometric displacement measurements.

However, this relation does not represent the most general limit of quantum measurements. Within the general framework of quantum measurement theory, the relationship between measurement error $\epsilon(A)$ and disturbance $\eta(B)$ is described by the Ozawa inequality [80, 81]:

$$\epsilon(A)\eta(B) + \epsilon(A)\sigma(B) + \sigma(A)\eta(B) \geq \frac{1}{2} \left| \langle [\hat{A}, \hat{B}] \rangle \right|. \quad (3.3)$$

This generalized inequality shows that the measurement limit is governed not only by error-disturbance products, but also by intrinsic quantum fluctuations. Therefore, appropriately engineered measurement schemes can surpass the conventional SQL without violating quantum mechanics.

In conventional position-meter interferometers, the angular displacement θ is directly measured. Because

$$\dot{\theta} \propto [\hat{\theta}, \hat{H}] \neq 0, \quad (3.4)$$

the measurement back-action perturbs the subsequent system dynamics. Within the Ozawa framework, both $\epsilon(\theta)$ and $\eta(p)$ remain finite, leading to an unavoidable trade-off. In gravitational-wave interferometers, this manifests as radiation-pressure noise limiting low-frequency sensitivity [35].

In contrast, angular momentum L satisfies

$$\dot{L} \propto [\hat{L}, \hat{H}] = 0, \quad (3.5)$$

and therefore

$$[\hat{L}(t), \hat{L}(t')] = 0. \quad (3.6)$$

Thus L is a QND observable [19]. In this case,

$$|\langle [\hat{L}, \hat{L}] \rangle| = 0, \quad (3.7)$$

and the right-hand side of Eq. (3.3) vanishes. The constraint linking measurement error and back-action is relaxed, allowing both $\epsilon(L)$ and $\eta(L)$ to be simultaneously suppressed in principle.

This is not merely theoretical. While experimental verifications of generalized quantum measurement limits have been performed primarily in microscopic systems, direct tests in macroscopic mechanical oscillators remain rare. CHRONOS provides a unique opportunity to probe this regime [57].

The torsion-bar interferometer realizes a macroscopic QND system with large moment of inertia and low-frequency dynamics. By independently characterizing radiation-pressure torque fluctuations and readout noise, it becomes possible to experimentally access the terms

$$\epsilon(L), \quad \eta(L), \quad \sigma(L), \quad (3.8)$$

and directly test Eq. (3.3) at macroscopic scales.

Such experiments address fundamental questions about the quantum-to-classical transition and the applicability of quantum mechanics to large-mass systems. Demonstrating generalized quantum measurement limits in gravitational-wave-scale apparatus would represent a major advance in fundamental physics.

By exploiting these principles, it becomes possible to evade the conventional trade-off between shot noise and radiation-pressure noise, enabling measurements beyond the SQL. Representative QND approaches include quantum squeezing [26, 25] and speed-meter interferometry [19, 85, 27, 64]. In particular, speed-meter schemes measure velocity (or momentum), intrinsically suppressing back-action noise [27, 35].

CHRONOS adopts the speed-meter interferometer concept to suppress radiation-pressure noise in the low-frequency regime and to realize quantum non-demolition (QND) measurements [19, 85, 27, 35]. A key feature of CHRONOS is that this principle is implemented and tested in the sub-Hz frequency band.

In existing ground-based interferometers, quantum noise dominates only above several tens of Hz, as seismic and Newtonian noise limit the sensitivity at lower frequencies [1, 50]. In contrast, CHRONOS is designed such that quantum noise remains a dominant limitation even in the low-frequency regime, enabling direct experimental access to quantum measurement effects in macroscopic test masses.

This establishes CHRONOS as a unique experimental platform with the potential to test generalized quantum measurement theory, including the Ozawa inequality [80, 81], in a macroscopic mechanical system. Such a demonstration would represent a significant advance in both quantum measurement science and fundamental physics.

The realization of QND measurements in the low-frequency regime critically depends on the optical design. In a speed-meter interferometer, the goal is to extract a quantity proportional to the time derivative of the test-mass position, i.e., its velocity [27, 35]. To achieve this, the optical field must interact with the test mass multiple times, thereby introducing a finite time delay in the measurement process. This delay encodes the difference between phase shifts at different times and allows construction of an observable less sensitive to measurement back-action.

In conventional implementations, such a delay is achieved by increasing the effective number of round trips using a high-finesse cavity [19]. However, increasing finesse enhances coating loss and optical absorption, which increases thermal noise and degrades quantum-limited performance. This limitation becomes particularly severe in the sub-Hz regime, where mechanical and coating dissipation dominate [91, 100].

In CHRONOS, we instead adopt a long optical path design incorporating triangular cavities [58], geometrically extending the effective propagation time of light. This realizes the required time delay without relying on high finesse. The number of reflections remains low, minimizing coating loss and absorption-induced thermal noise. The combination of long optical paths and low-loss design enables CHRONOS to maintain a quantum-noise-dominated regime even at low frequencies.

This strategy represents a fundamentally different design paradigm from the conventional high-finesse delay approach, establishing a new optical architecture tailored for low-frequency gravitational-wave detection. It provides an important design guideline for implementing QND techniques in future long-baseline interferometers.

Furthermore, CHRONOS enables precise observations of the transition region between quantum and classical noise. In practical interferometers, quantum noise, thermal noise, and environmental noise dominate in different frequency ranges [35]. Measurements in the crossover regime provide direct insight into the quantum-to-classical transition in macroscopic mechanical systems. In particular, observing radiation-pressure-driven motion of a test mass offers a unique probe of quantum optomechanical effects [26].

The establishment of such quantum measurement techniques has direct implications for next-generation gravitational-wave detectors. Future facilities such as the Einstein Telescope [84] and Cosmic Explorer [86] identify low-frequency quantum noise suppression as a central technological challenge. Speed-meter architectures based on long optical paths and low optical loss may therefore form a core strategy for quantum noise reduction in these detectors.

CHRONOS serves as a unique experimental platform to demonstrate speed-meter interferometry and quantum noise suppression at the scale of a full interferometer. The

present effort therefore goes beyond incremental sensitivity improvements, aiming instead at the implementation and validation of new principles of quantum measurement.

In summary, by realizing quantum non-demolition measurements in the gravitational-wave observation band, CHRONOS opens a new experimental frontier at the interface between quantum mechanics and gravitational-wave physics. This constitutes the third scientific pillar of CHRONOS, alongside IMBH observations and stochastic background searches, and contributes to establishing foundational technologies for future gravitational-wave astronomy.

3.4 Scientific Reach IV: Prompt Gravity Signals from Large Earthquakes

The fourth scientific objective of CHRONOS is the detection of gravity-gradient perturbations associated with large earthquakes, known as prompt gravity signals [57]. When a major earthquake occurs, rapid mass redistribution due to fault rupture induces a change in the gravitational potential. Unlike elastic waves, this gravitational perturbation propagates at the speed of light and can therefore be observed before destructive seismic surface waves arrive [79, 111]. This enables a fundamentally new approach to earthquake early detection that is not accessible with conventional seismometers.

Gravitational-wave interferometers are intrinsically sensitive to temporal variations in the gravitational potential and thus have the capability to directly detect gravity-gradient signals generated by seismic mass redistribution [50]. Such signals have traditionally been treated as Newtonian noise, a limiting factor in GW observations [91]. However, for detectors like CHRONOS with high sensitivity in the sub-Hz band, these signals can instead be utilized as a target of observation. This establishes a new interdisciplinary connection between gravitational-wave detection technology and seismology.

Figure 3.4 compares the ASD of gravity-gradient signals from earthquakes with mag-

magnitudes $M = 5$ – $M = 9$ with CHRONOS sensitivity. As magnitude increases, the gravitational perturbation becomes stronger at low frequencies. For large events around $M \sim 7$, detectable signals are expected within the CHRONOS band.

Numerical simulations assuming realistic geological conditions near the ASGRAF site indicate detection efficiency within approximately 100 km. Because gravity perturbations propagate at the speed of light, a lead time of up to ~ 8 seconds is achievable for large earthquakes [79]. This time margin is sufficient for automated infrastructure protection systems.

Beyond early warning, such measurements directly probe time-varying gravitational fields generated by macroscopic mass redistribution. They also provide essential validation of Newtonian-noise models, which represent a primary limitation for sub-Hz ground-based detectors [50].

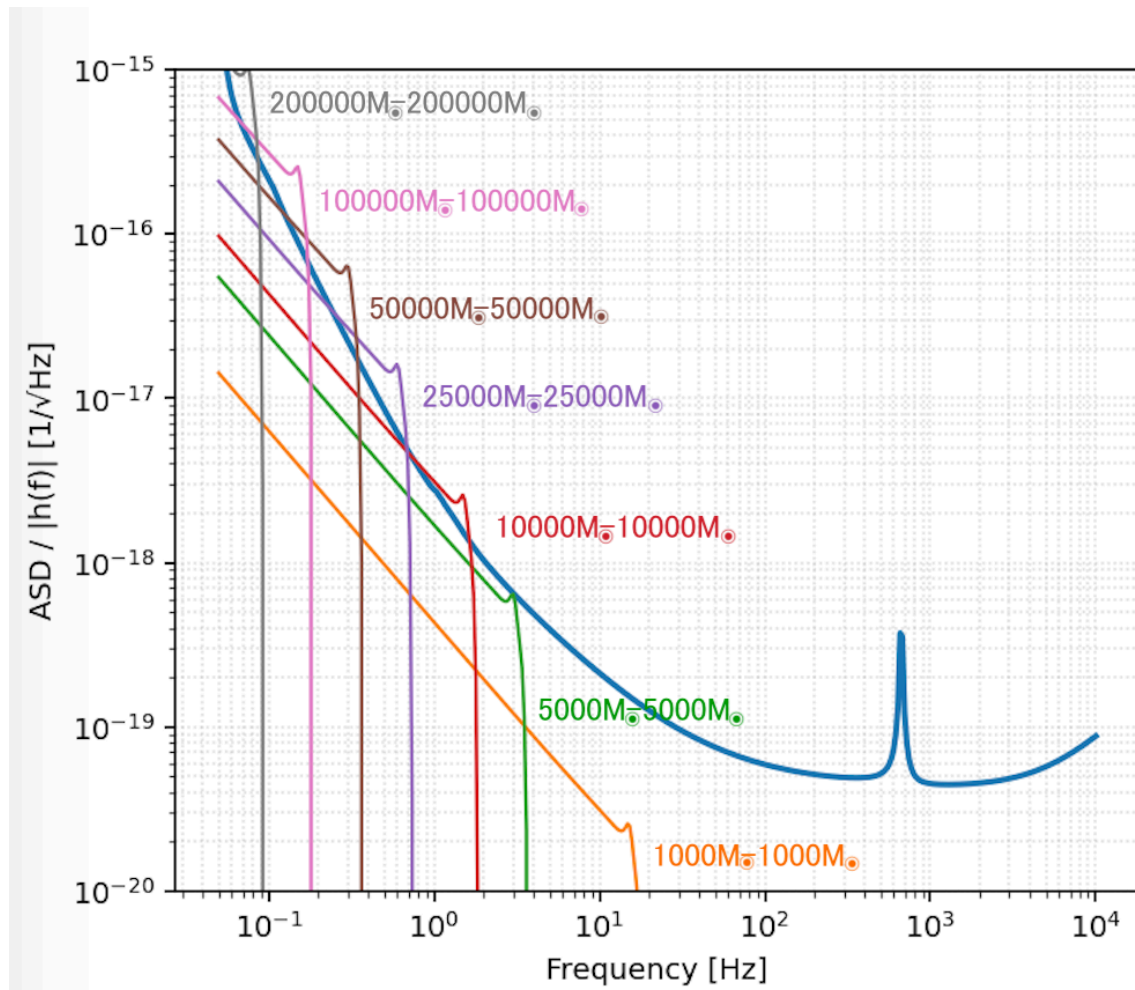


Figure 3.1: Strain amplitude spectral density (ASD) of the detector (blue curve) overlaid with the frequency-domain inspiral waveforms of equal-mass binary black hole systems with component masses ranging from $10^3 M_\odot$ to $2 \times 10^5 M_\odot$. In the inspiral regime the waveform amplitude follows a power-law frequency dependence, appearing as straight lines in the log-log plot. The vertical lines indicate the approximate termination frequency of the inspiral, which shifts toward lower frequencies for higher total masses. The figure shows that the detector is particularly sensitive to intermediate- and heavy-mass black hole binaries in the sub-Hz band, with optimal overlap occurring for masses of order 10^4 – $10^5 M_\odot$.

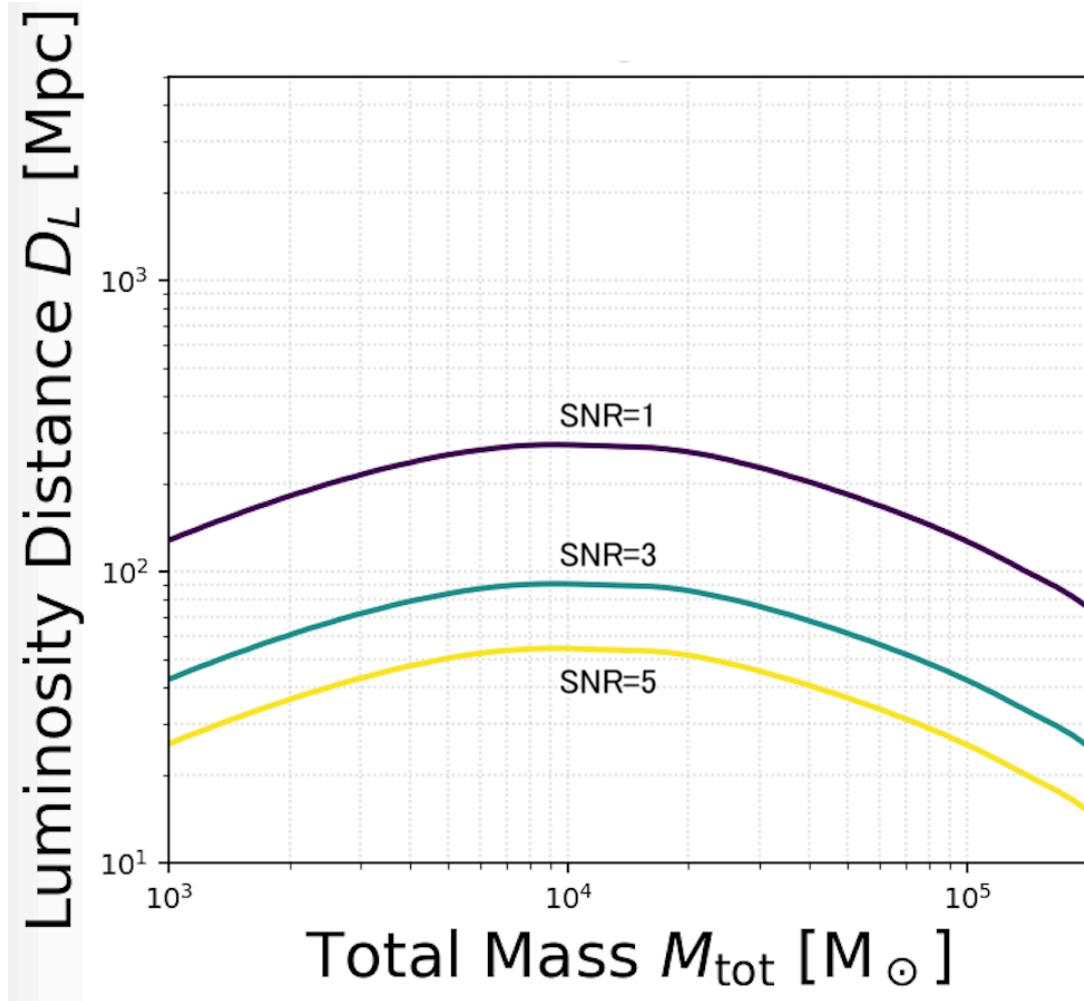


Figure 3.2: Estimated SNR reach for IMBH binary mergers observable with CHRONOS. The vertical axis shows the luminosity distance corresponding to fixed SNR values, and the horizontal axis denotes the total binary mass. Solid, dashed, and dotted curves correspond to $\text{SNR} = 1, 3,$ and $5,$ respectively. The SNR is computed using the standard matched-filter formalism [39, 74]: $\text{SNR}^2 = 4 \int \frac{|\tilde{h}(f)|^2}{S_n(f)} df$. Sensitivity peaks in the mass range $M \sim 10^4$ – $10^5 M_{\odot}$, where the merger frequency enters the sub-Hz band covered by CHRONOS. Increasing arm length improves low-frequency sensitivity without requiring a proportional increase in cavity finesse, thereby reducing coating loss while preserving QND conditions.

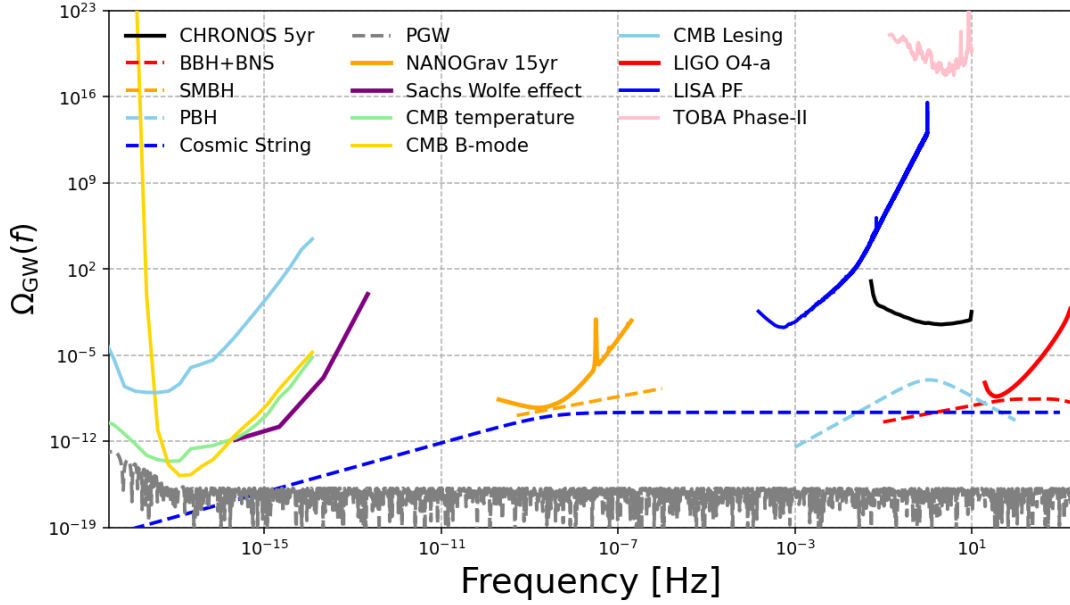


Figure 3.3: Expected sensitivity of CHRONOS to the stochastic gravitational-wave background (SGWB), expressed in terms of the gravitational-wave energy density $\Omega_{\text{GW}}(f)$ as a function of frequency. The sensitivity curve assume five years of integration time. The shaded and colored regions indicate current observational constraints from existing experiments, including LIGO O4a, LISA Pathfinder, CMB temperature and polarization measurements, CMB lensing, and the Sachs-Wolfe effect. Representative theoretical predictions are also shown for comparison, including stochastic backgrounds produced by unresolved binary black hole and binary neutron star populations, supermassive black hole binaries, primordial black holes, cosmic strings, and primordial gravitational waves. These models span a wide range of spectral shapes and amplitudes, illustrating the importance of broad-band observations in identifying the physical origin of a detected background. CHRONOS operates in the 0.1-10 Hz band, bridging the frequency gap between space-based interferometers such as LISA and ground-based detectors such as LIGO. This frequency range remains largely unexplored and is particularly sensitive to stochastic signals originating from early-Universe processes, including first-order phase transitions and cosmic string networks. The figure demonstrates that CHRONOS not only improves sensitivity in an unexplored frequency band but also plays a critical role in reconstructing the full spectral shape of the stochastic background when combined with detectors operating at lower and higher frequencies. Such multi-band measurements are essential for separating astrophysical and cosmological contributions to the SGWB and for probing physics beyond the standard cosmological model.

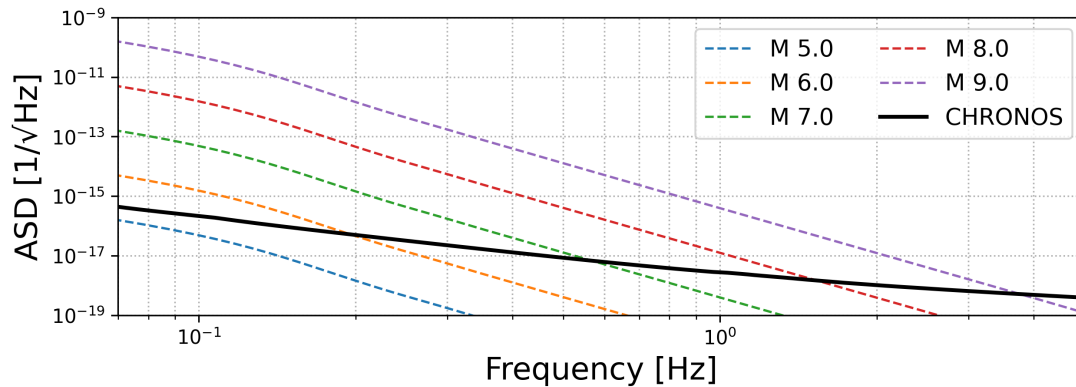


Figure 3.4: Predicted sensitivity of CHRONOS to prompt gravity signals generated by large earthquakes. The vertical axis shows the amplitude spectral density (ASD) of the induced gravitational perturbation, while the horizontal axis represents frequency. Colored dashed curves indicate expected gravity-gradient signals for earthquakes with magnitudes $M = 5.5$ to $M = 9$, based on rapid mass-redistribution models [79, 111]. Prompt gravity signals arise from time-dependent changes in the gravitational potential caused by fault rupture and propagate at the speed of light, in contrast to seismic waves traveling at km/s speeds [79]. Therefore, gravity perturbations can in principle be detected seconds before the arrival of destructive surface waves. Longer arm-length configurations improve low-frequency sensitivity, enhancing detection capability. Detection of such signals provides both a potential earthquake early-warning mechanism and a direct measurement of terrestrial gravity-field variations.

Sensitivity

The sensitivity of CHRONOS is determined by the combined contributions of quantum noise and various technical noise sources, environmental background noise, each of which dominates in different frequency ranges [92, 74, 57].

For interferometers targeting the sub-Hz band, the dominant noise sources vary significantly with frequency, reflecting the interplay between quantum noise, thermal noise, and environmental disturbances [9, 104]. In particular, at low frequencies the sensitivity is typically limited by radiation-pressure noise, seismic noise, and Newtonian (gravity-gradient) noise, while at higher frequencies shot noise becomes dominant [26, 19, 57].

Therefore, before presenting detailed derivations of individual noise terms, it is important to first provide an overview of the overall noise budget, as commonly adopted in the sensitivity studies of advanced gravitational-wave detectors [1, 12, 57].

Figure 4.1 shows the expected strain sensitivity for an optimized CHRONOS configuration, together with the contributions from individual noise sources. The black curve represents the total sensitivity obtained by taking the quadrature sum of all noise components [92], including shot noise and radiation-pressure noise (collectively forming quantum noise) [26, 66], coating Brownian noise [51, 52], torsion-bar thermal noise [16], seismic noise [90], and Newtonian noise arising from Rayleigh waves [50].

The optical and mechanical parameters used in this evaluation are summarized in Table 4.1.

As seen in the figure, the sensitivity of CHRONOS is limited by different physical pro-

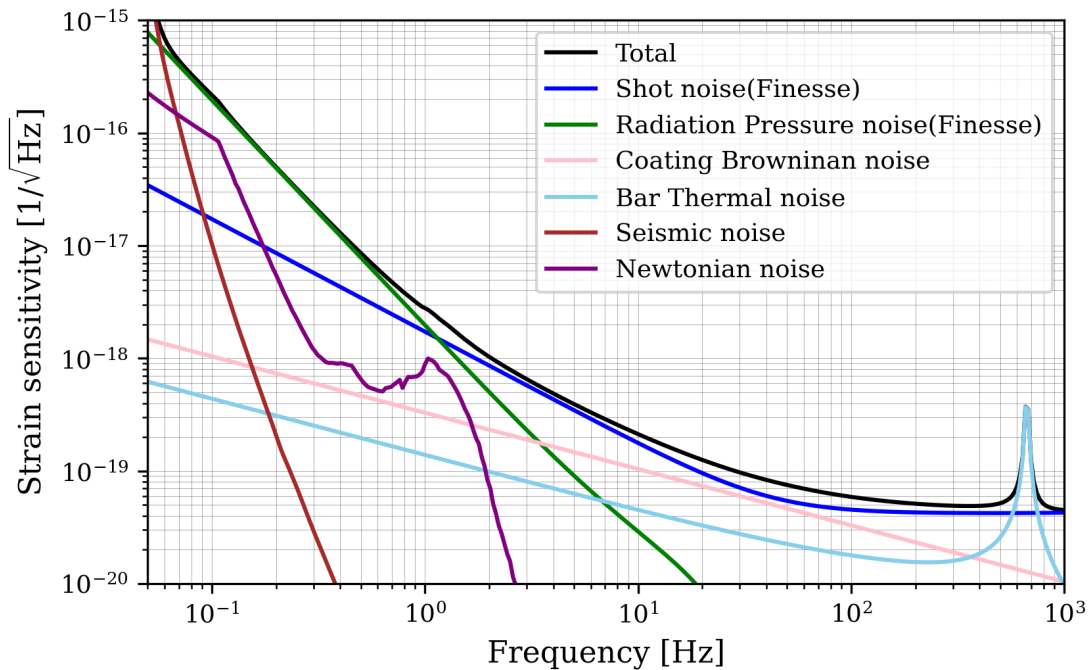


Figure 4.1: Expected strain sensitivity of the CHRONOS interferometer. The black curve represents the total sensitivity obtained by combining all noise sources. Individual contributions are shown for shot noise, radiation-pressure noise, coating Brownian noise, torsion-bar thermal noise, seismic noise, and Newtonian noise arising from Rayleigh waves. The dominant noise source changes with frequency, illustrating the hierarchical structure of sensitivity limitations in a sub-Hz interferometer.

cesses depending on the frequency band. At high frequencies, shot noise—originating from optical phase fluctuations—is dominant, representing a fundamental limitation of quantum measurement [26, 19].

At lower frequencies, radiation-pressure noise increases; however, the Sagnac speed-meter configuration adopted in CHRONOS suppresses the rapid degradation typically observed in position-meter interferometers [27, 85, 35].

In the intermediate frequency range around 1–10 Hz, coating Brownian noise becomes the primary limiting factor [51, 52]. This region corresponds to the transition from quantum-noise-dominated to thermal-noise-dominated sensitivity, where the mechanical loss of coating materials and the beam size design directly determine the performance [71].

At even lower frequencies, rotational thermal noise of the torsion bar becomes dominant [16, 58]. Since CHRONOS directly measures the rotational degree of freedom, thermal fluctuations of the torsional mode appear directly in the observation band and set a key sensitivity limit in the sub-Hz regime.

In the lowest frequency region, Newtonian noise arising from ground density fluctuations induced by Rayleigh waves dominates [90, 50]. Because this noise originates from gravitational coupling itself, it cannot be mitigated by mechanical isolation and thus represents the ultimate environmental noise limit for ground-based sub-Hz detectors.

In the following sections, each of these noise contributions is formulated in detail. We derive the quantum noise model based on the input–output relations of the Sagnac interferometer [66, 27], as well as evaluation methods for thermal and environmental noise. This provides a quantitative understanding of how the total sensitivity shown in Fig. 4.1 is determined.

4.1 Principle

The readout in this study follows the TOBA framework [16], which is based on the torsional degree of freedom around the z axis. The angular displacement θ of a bar-shaped test mass with moment of inertia I , torsional spring constant κ , and loss coefficient γ obeys

$$I \ddot{\theta}(t) + \gamma \dot{\theta}(t) + \kappa \theta(t) = N_{\text{gw}}(t), \quad (4.1)$$

where the torque from the gravitational-wave tidal acceleration $a_i = \frac{1}{2} \ddot{h}_{ij} x^j$ is given by [92, 40]

$$N_{\text{gw}}(t) = \frac{1}{2} \ddot{h}_{ij}(t) \epsilon_{zki} Q_{kj}, \quad (4.2)$$

with

$$Q_{ij} \equiv \int_V \rho \left(x_i x_j - \frac{1}{3} r^2 \delta_{ij} \right) dV. \quad (4.3)$$

In the frequency domain, this becomes

$$\theta(\Omega) = \chi_\theta(\Omega) \left[-\frac{I_{\text{eff}}}{2} \Omega^2 (h_+ F_+ + h_\times F_\times) \right], \quad (4.4)$$

$$\chi_\theta(\Omega) \equiv \frac{1}{\kappa - I\Omega^2 + i\gamma\Omega}, \quad (4.5)$$

where the torsional resonance $\Omega_t = \sqrt{\kappa/I}$ is taken to be well below the observational band (0.1–10 Hz). In the regime $\Omega \gg \Omega_t$, the susceptibility reduces to $\chi_\theta \simeq (-I\Omega^2)^{-1}$, yielding

$$\theta(\Omega)_i \simeq \frac{\eta_g}{2} (h_+ F_+ + h_\times F_\times), \quad (4.6)$$

where $i = \{X, Y\}$. The total and effective moments of inertia are

$$I = \int \rho(x^2 + y^2) dV, \quad I_{\text{eff}} = \int \rho(x^2 - y^2) dV, \quad (4.7)$$

such that $\eta_g \equiv I_{\text{eff}}/I = 0.936$ for an ideal thin rod. In the long-wavelength limit with z -axis incidence, the antenna patterns are [40]

$$F_+ = \sin 2\alpha, \quad F_\times = -\cos 2\alpha. \quad (4.8)$$

By combining two orthogonal bars (X and Y) into a differential readout,

$$\theta(\Omega) = \theta_X - \theta_Y = \eta_g (h_+ F_+ + h_\times F_\times), \quad (4.9)$$

common-mode noise sources such as translational motion and laser intensity fluctuations are suppressed, while retaining sensitivity to linear combinations of the two polarizations [16].

4.2 Quantum-noise description and physical interpretation

In this section, we clarify the physical interpretation of the quantum noise described by Eqs. (4.11) and (4.16), and elucidate the mechanism that determines the sensitivity of the CHRONOS interferometer.

Quantum noise in an interferometer originates from vacuum fluctuations entering through the detection port, and is described in terms of fluctuations of the optical field

quadratures. Following the Buonanno–Chen formalism [21], we adopt the two-photon representation [26], in which the input and output quadrature vectors are defined as

$$\mathbf{a} \equiv \begin{pmatrix} a_1 \\ a_2 \end{pmatrix}, \quad \mathbf{b} \equiv \begin{pmatrix} b_1 \\ b_2 \end{pmatrix}. \quad (4.10)$$

Here, a_1 and a_2 represent the amplitude (in-phase) and phase (out-of-phase) quadratures, respectively.

Within this framework, quantum noise can be understood as the interplay of two fundamental contributions:

- shot noise (measurement noise), arising from phase quadrature fluctuations,
- radiation-pressure noise (back-action noise), arising from amplitude quadrature fluctuations.

The former directly appears in the readout signal, while the latter couples to the motion of the test mass (in this work, the angular displacement θ) via radiation pressure. The total quantum noise is therefore determined by the balance between these two contributions, which is governed by the optical response and the optomechanical coupling.

Under these definitions, the input–output relation of the interferometer is given by

$$\mathbf{b} = \frac{1}{M} \left[e^{2i(\beta_{\text{sag}} + \Phi_s)} C \mathbf{a} + \sqrt{2\mathcal{K}_{\text{sag}}} t_s e^{i(\beta_{\text{sag}} + \Phi_s)} \mathbf{D} \frac{\theta}{\theta_{\text{SQL}}} \right], \quad (4.11)$$

where the first term describes how the input vacuum fluctuations \mathbf{a} are transformed by the optical response of the interferometer, characterized by the matrix C and phase factors. The second term represents the signal transfer, in which the test-mass motion θ is imprinted onto the optical field through the optomechanical coupling \mathcal{K}_{sag} .

The transmittance of the signal recycling mirror (SRM) is $t_s = \sqrt{1 - R_s}$, and its phase detuning is Φ_s .

To evaluate the quantum noise, we introduce the matrices

$$G = CC^\top, \quad (4.12)$$

$$Q = \Re(\mathbf{D}) \Re(\mathbf{D})^\top + \Im(\mathbf{D}) \Im(\mathbf{D})^\top, \quad (4.13)$$

where the matrix $C = [c_{ij}]$ and the column vector $\mathbf{D}^\top = (D_1, D_2)$ are defined following Eqs. (2.22)–(2.24) of Ref. [21].

The quantum-noise spectrum given by Eq. (4.16) is fully determined by the optical response matrix C and the signal response vector \mathbf{D} . The matrix $G = CC^\top$ characterizes how vacuum fluctuations propagate and are amplified through the interferometer, while the matrix Q quantifies how efficiently the signal (angular displacement) is transduced into the optical readout.

Therefore, the quantum-noise spectrum can be physically interpreted as the ratio between the ‘noise propagation strength’ and the ‘signal response efficiency.’

The standard quantum limit (SQL) for angular displacement is defined as [35]

$$\theta_{\text{SQL}}(\Omega) = \sqrt{\frac{2\hbar}{I\Omega^2}}. \quad (4.14)$$

In conventional position-meter interferometers, radiation-pressure noise dominates at low frequencies, while shot noise dominates at high frequencies. The SQL corresponds to the frequency at which these two noise contributions become equal, representing the fundamental sensitivity limit set by quantum mechanics.

In contrast, the Sagnac topology adopted in CHRONOS operates as a speed meter, responding to the velocity rather than the position of the test mass [27, 85]. In this configuration, counter-propagating light beams probe the test mass at different times, effectively measuring the time derivative of motion. As a result, the radiation-pressure back-action is partially canceled at low frequencies [35].

This property is explicitly reflected in the phase response of the Sagnac interferometer. The phase accumulated in the arm cavity is given by

$$\beta(\Omega) = \arctan\left(\frac{\Omega}{\gamma}\right), \quad \beta_{\text{sag}}(\Omega) = 2\beta(\Omega) + \frac{\pi}{2},$$

following the standard input–output formalism of signal-recycled interferometers [66, 21].

In the Sagnac topology, the effective optomechanical coupling is given by

$$\mathcal{K}_{\text{sag}}(\Omega) = 4\mathcal{K}(\Omega) |H_{\text{PRC}}(\Omega)|^2 \sin^2 \beta_{\text{sag}}(\Omega), \quad (4.15)$$

where $\mathcal{K}(\Omega)$ is the frequency-dependent optomechanical coupling, and γ is the cavity bandwidth, defined as in Ref. [21].

In the low-frequency limit, $\beta(\Omega) \rightarrow 0$, which leads to $\sin^2 \beta_{\text{sag}}(\Omega) \rightarrow 0$. As a consequence, the effective coupling \mathcal{K}_{sag} is intrinsically suppressed. This directly implies that radiation-pressure back-action is naturally reduced at low frequencies, providing a key advantage of the Sagnac speed-meter configuration [27].

In addition to this intrinsic suppression, the overall magnitude and frequency dependence of the coupling are strongly modified by the power-recycling cavity (PRC), whose transfer function is given by

$$H_{\text{PRC}}(\Omega) = \frac{\sqrt{1 - R_p}}{1 - \sqrt{R_p} e^{2i\tau_p\Omega} r_{\text{ifo}}}.$$

Here, the effective interferometer reflectivity, including the Sagnac propagation, is expressed as

$$r_{\text{ifo}} = i|r_{\text{loop}}| \sin(\beta_{\text{sag}} + \tau_{\text{sag}}\Omega),$$

where τ_{sag} is the one-way propagation time in the Sagnac loop, and $r_{\text{loop}} \sim r_i$ represents the effective reflectivity of the ring cavities and the Sagnac loop.

Therefore, while the $\sin^2 \beta_{\text{sag}}$ term determines the fundamental low-frequency suppression of back-action, the PRC transfer function $H_{\text{PRC}}(\Omega)$ plays a dominant role in shaping the overall quantum-noise spectrum [21, 35]. In particular, by tuning the PRC detuning phase, one can control both the effective optomechanical coupling and the quadrature rotation, enabling optimization of the quantum noise without requiring excessive circulating power.

From the above discussion, the Sagnac speed-meter configuration intrinsically suppresses radiation-pressure noise at low frequencies, thereby enabling stable and controllable quantum-noise behavior even in the sub-Hz band. This feature provides a fundamental advantage over conventional position-meter interferometers and is essential for low-frequency gravitational-wave observations targeted by CHRONOS.

The resulting quantum-noise spectral density for angular displacement is

$$\theta(\Omega) = \frac{\theta_{\text{SQL}}(\Omega)}{\sqrt{2\mathcal{K}_{\text{sag}}(\Omega)(1 - r_s^2)}} \sqrt{\frac{\boldsymbol{\nu}^T G \boldsymbol{\nu}}{\boldsymbol{\nu}^T Q \boldsymbol{\nu}}}, \quad (4.16)$$

where the homodyne detection vector is defined as $\boldsymbol{\nu}^T = (\cos \zeta, \sin \zeta)$ [66, 35].

This expression shows that the quantum noise is governed by three independent elements: (i) the standard quantum limit θ_{SQL} , (ii) the optomechanical coupling \mathcal{K}_{sag} , and (iii) the choice of detection quadrature.

Because shot noise and radiation-pressure noise are generally correlated, an appropriate choice of ζ allows partial cancellation between them, leading to a reduction of the total quantum noise [66]. The value adopted in this work, $\zeta = 46^\circ$, corresponds to the optimal effective detection angle derived from the principal axes of G and Q .

In addition to the readout optimization, the detuning phase of the power-recycling cavity (PRC), ϕ_p , plays a central role in shaping the quantum-noise spectrum. The PRC detuning introduces a frequency-dependent quadrature rotation, which simultaneously modifies the effective optomechanical coupling and the readout basis. This enables optimization of the quantum noise around 1 Hz without requiring excessive circulating optical power.

In contrast, detuning of the signal-recycling cavity (SRC) primarily induces an overall quadrature rotation [21, 35], and its impact on sensitivity improvement is relatively limited within the parameter regime considered here. This clearly indicates that, for CHRONOS, quantum-noise optimization is predominantly achieved through PRC tuning, rather than SRC detuning.

Based on these considerations, the quantum noise of CHRONOS can be characterized in three distinct frequency regions as shown in Fig. 4.1:

1. At high frequencies, the sensitivity is limited by shot noise, originating from quantum phase fluctuations [26]. It can be improved by increasing the circulating power P_{arm} , which reduces phase uncertainty.
2. Around ~ 1 Hz, shot noise and radiation-pressure noise become comparable, and the quantum noise approaches the standard quantum limit (SQL) [19, 66]. The design parameters listed in Table 4.1 are chosen to achieve optimal sensitivity in this frequency band, where quantum back-action and measurement noise are balanced.

3. At low frequencies, radiation-pressure noise is strongly suppressed due to the Sagnac speed-meter effect [27]. This prevents the rapid Ω^{-2} degradation of sensitivity that typically occurs in position-meter interferometers [35]. Such low-frequency stability is a defining feature of CHRONOS and is crucial for sub-Hz gravitational-wave detection.

The total sensitivity curve is obtained by combining the quantum-noise spectrum with thermal noise [71, 51] and Newtonian noise [50] as summarized in following sections. For the optimized 2.5 m configuration, quantum noise and thermal noise become comparable around 1 Hz. This indicates that further sensitivity improvement will depend less on increasing laser power, and more critically on reducing optical losses and suppressing material-related thermal noise. The optimization detail is explained in Inoue *et al.* [58].

4.3 Bar Thermal Noise

Torsion-bar thermal noise is one of the dominant noise sources that determine the sensitivity of the CHRONOS interferometer in the sub-Hz frequency band. This noise originates from thermal fluctuations associated with internal mechanical dissipation in the torsion bar and its suspension system, and is described by the fluctuation–dissipation theorem (FDT) [22, 91].

In CHRONOS, the test mass is supported by a torsional degree of freedom, and gravitational-wave signals are read out as small angular displacements of the bar. Therefore, thermally excited torsional motion directly couples to the observable signal, constituting a fundamental sensitivity limit. In particular, due to the speed-meter topology suppressing low-frequency radiation-pressure noise, torsion-bar thermal noise becomes the dominant noise source in the low-frequency regime [27].

According to the fluctuation–dissipation theorem, thermal fluctuations are directly related to mechanical dissipation through the mechanical impedance:

$$S_\tau(\Omega) = 4k_B T \operatorname{Re}[Z(\Omega)], \quad (4.17)$$

where S_τ is the power spectral density of the thermal torque, and $Z(\Omega)$ is the mechan-

ical impedance [22].

The angular fluctuation spectrum is then expressed as

$$S_\theta(\Omega) = |\chi(\Omega)|^2 S_\tau(\Omega). \quad (4.18)$$

4.3.1 Noise Model

The torsion-bar thermal noise in CHRONOS can be decomposed into two contributions [91]:

$$S_{\text{bar,bg}}(\Omega) = \sqrt{\frac{4k_{\text{B}}T}{\sqrt{\pi}} \frac{1 - \sigma_s^2}{\Omega Y_s}} \phi_s^{\text{eff}}, \quad (4.19)$$

$$S_{\text{bar,rot}}(\Omega) = \sqrt{\frac{4k_{\text{B}}T}{I} \frac{\Omega \omega_{\text{tb}}/Q}{(\omega_{\text{tb}}^2 - \Omega^2)^2 + (\omega_{\text{tb}}\Omega/Q)^2}}. \quad (4.20)$$

The total noise converted to the interferometer readout is

$$S_{\text{bar}}(\Omega) = \frac{\eta_g}{L_{\text{bar}}} \sqrt{S_{\text{bar,bg}}^2 + S_{\text{bar,rot}}^2}. \quad (4.21)$$

Broadband component The term $S_{\text{bar,bg}}$ represents structural damping originating from internal friction in the material and suspension system. Under the structural damping model [91], it typically exhibits a frequency dependence of

$$S \propto \Omega^{-1/2}. \quad (4.22)$$

Resonant component The term $S_{\text{bar,rot}}$ arises from thermal excitation of the torsional eigenmode and shows the following behavior:

- $\Omega \ll \omega_{\text{tb}}$: $S \propto \Omega^{-1}$
- $\Omega \approx \omega_{\text{tb}}$: resonant peak
- $\Omega \gg \omega_{\text{tb}}$: $S \propto \Omega^{-3}$

Such behavior is characteristic of thermally driven harmonic oscillators with finite mechanical loss [91].

4.3.2 Frequency Dependence in CHRONOS

In the optimized CHRONOS design, torsion-bar thermal noise dominates in the frequency range of approximately 1 Hz. In this band,

- seismic noise is sufficiently suppressed by multi-stage isolation,
- radiation-pressure noise is reduced by the speed-meter topology,

leaving thermal noise associated with mechanical dissipation as the limiting noise source.

This behavior is fundamentally different from that of conventional Michelson-type interferometers. In detectors such as LIGO, suspension thermal noise appears as a secondary contribution, whereas in CHRONOS the torsional degree of freedom itself is the signal channel, and thus thermal noise directly enters the observation band.

4.3.3 Design Implications and Future Prospects

From the above expressions, reduction of torsion-bar thermal noise requires:

- minimizing the effective loss angles ϕ_s^{eff} and ϕ_0 ,
- achieving a high mechanical quality factor Q ,
- increasing the moment of inertia I ,
- lowering the operating temperature T .

In particular, cryogenic operation reduces thermal noise as

$$S \propto \sqrt{T}, \quad (4.23)$$

making it a crucial element of the CHRONOS design. Furthermore, the development of high- Q materials (e.g., sapphire) and low-loss suspension systems directly enhances sensitivity in the sub-Hz band.

These results establish a direct link between mechanical dissipation and the observable strain sensitivity, highlighting that torsion-bar thermal noise represents a fundamental thermodynamic limit in CHRONOS.

4.4 Coating Brownian noise

Coating Brownian noise arising from dielectric multilayer coatings is one of the fundamental noise sources that becomes dominant in the intermediate frequency band of the CHRONOS interferometer. This noise originates from microscopic mechanical dissipation within the multilayer dielectric films deposited on the ETM surface to achieve high reflectivity, and manifests as thermally driven surface displacement according to the fluctuation–dissipation theorem (FDT) [22, 71, 51]. In CHRONOS, after seismic and suspension noises are sufficiently suppressed, and radiation-pressure noise is reduced by the speed-meter topology, coating Brownian noise plays a crucial role as a material-limited noise source that ultimately determines the detector sensitivity.

4.4.1 Interpretation based on the fluctuation–dissipation theorem

According to the fluctuation–dissipation theorem [22], any mechanical degree of freedom that dissipates energy under an external force must exhibit corresponding thermal fluctuations in thermal equilibrium. In the case of mirror coatings, internal friction within the dielectric layers excites microscopic elastic deformations randomly, resulting in stochastic surface displacement of the mirror. Since the interferometer measures changes in optical path length, these surface fluctuations directly appear as measurement noise.

In Levin’s method [71], a virtual periodic force with the same spatial profile as the measurement beam is applied to the mirror surface, and the resulting dissipated energy is used to evaluate the thermal noise. Therefore, coating thermal noise strongly depends on the beam size on the mirror, making optical mode design a critical factor in determining the noise level.

4.4.2 Noise model

Under the semi-infinite substrate approximation and the equivalent spring model [51, 54], the one-sided amplitude spectral density of coating Brownian noise is given by

$$S_{\text{coat}}(\Omega) = \frac{\eta_g}{L_{\text{bar}}} \sqrt{\frac{4k_{\text{B}}T}{\pi\Omega}} \sqrt{\frac{1 - \sigma_s^2}{\omega_{\text{ETM}}Y_s}} \sqrt{\phi_c^{\text{eff}}}. \quad (4.24)$$

Here, the factor η_g/L_{bar} represents a geometrical conversion factor that maps the physical displacement of the ETM surface to the equivalent displacement in the interferometer readout. k_{B} is the Boltzmann constant, and T is the coating temperature. As evident from the expression, $S_{\text{coat}} \propto \sqrt{T}$, indicating that cryogenic operation is highly effective in reducing coating thermal noise [118].

The elastic response of the substrate is determined by the Young's modulus Y_s and the Poisson ratio σ_s . These parameters govern how efficiently mechanical loss within the coating is converted into surface displacement. The beam radius on the mirror, ω_{ETM} , is also a key design parameter; a larger beam size spatially averages thermal fluctuations and reduces the resulting noise level [71].

The effective loss angle ϕ_c^{eff} reflects the thickness, elastic properties, and intrinsic loss angles of each layer in the multilayer coating, and is generally expressed as

$$\phi_c^{\text{eff}} = \frac{\sum_i Y_i d_i \phi_i}{\sum_i Y_i d_i}. \quad (4.25)$$

Therefore, multilayer designs using low-loss materials (e.g., SiN or SiON) directly reduce ϕ_c^{eff} and provide the most straightforward path to improving interferometer sensitivity [52, 100].

4.4.3 Frequency dependence and role in CHRONOS

The $f^{-1/2}$ frequency dependence of coating Brownian noise reflects the general behavior of thermally driven random forces acting on elastic media with mechanical dissipation [91]. Unlike quantum radiation-pressure noise, this noise is not suppressed by the speed-meter configuration, and therefore becomes relatively dominant in the intermediate frequency band.

In an optimized CHRONOS design, coating Brownian noise is expected to limit the sensitivity in the frequency range of approximately 1–10 Hz. At lower frequencies, torsion-bar thermal noise dominates, while at higher frequencies, shot noise becomes the primary limitation. Thus, coating Brownian noise forms a boundary between the quantum-noise-dominated regime and the thermal-noise-dominated regime.

Once coating thermal noise becomes dominant, increasing laser power no longer improves sensitivity. Further sensitivity improvements therefore require reduction of material loss, optimization of beam size, and implementation of cryogenic operation.

4.4.4 Implications for coating development in CHRONOS

Coating Brownian noise cannot be reduced solely by optical design and is directly linked to material properties. For this reason, the CHRONOS project identifies the development of novel amorphous coating materials with low mechanical loss at cryogenic temperatures as a key research objective.

In particular, SiN- and SiON-based multilayer coatings are promising candidates, as they may exhibit lower mechanical loss compared to conventional silica/tantala coatings [52, 100], and are expected to significantly contribute to future sensitivity improvements.

In summary, coating Brownian noise is a major material-related noise source in the intermediate frequency band of CHRONOS and represents one of the fundamental limitations determining the scientific performance of sub-Hz gravitational-wave observations.

4.5 Seismic Noise

Seismic noise is one of the most fundamental and unavoidable technical noise sources in ground-based interferometers, particularly in the low-frequency regime. In the sub-Hz band, ground motion typically exhibits amplitudes much larger than other technical noise sources, and without sufficient isolation, it would directly limit the detector sensitivity [90, 50].

In CHRONOS, the observable is not the translational displacement itself, but the rotational (yaw) degree of freedom of the torsion bar. Therefore, seismic disturbances couple to the readout channel through a conversion from translational motion to rotational motion. The efficiency of this coupling is determined by the mechanical response of the suspension system, and plays a crucial role in the low-frequency sensitivity design [16].

4.5.1 Coupling from Ground Motion to Rotational Noise

Ground motion is primarily generated as translational displacement. However, due to asymmetries in the suspension system and finite stiffness at the support points, it couples into the rotational degree of freedom of the torsion bar. This coupling can be described by the yaw transfer function $H_{\text{yaw}}(\Omega)$.

In this work, we adopt a representative underground ground-displacement spectrum $S_x^{\text{ground}}(\Omega)$ based on measured environmental data, and include attenuation from both the pre-isolation system and the suspension chain, following approaches established in advanced interferometers [1, 12]. The resulting seismic noise contribution is expressed as

$$S_{\text{seis}}(\Omega) = \frac{|H_{\text{yaw}}(\Omega)|}{G_{\mu g} G_{\text{pre}}} S_x^{\text{ground}}(\Omega). \quad (4.26)$$

Here, $G_{\mu g}$ is the conversion factor between mechanical torque and equivalent gravitational acceleration, including geometric factors such as the effective lever arm of the bar. G_{pre} represents the frequency-dependent attenuation provided by the pre-isolation system. Multi-stage passive isolation typically yields a suppression scaling of Ω^{-4} to Ω^{-6} above the microseismic peak [1].

4.5.2 Role of Pre-Isolation and Suspension System

In CHRONOS, the concept of multi-stage seismic isolation, established in detectors such as LIGO, is extended toward lower frequencies by combining passive and active isolation systems [1]. The pre-isolation stage serves as the first line of defense against

large-amplitude low-frequency ground motion, while subsequent multi-stage pendulum suspensions further suppress higher-frequency components.

For the yaw degree of freedom, the coupling from translational motion is empirically known to be suppressed to a level of approximately 10^{-2} , consistent with assumption in torsion-bar antenna (TOBA) systems [16]. As a result, even large translational ground motion has a significantly reduced impact on the rotational readout.

Seismic noise increases rapidly below approximately 1 Hz. However, with appropriate pre-isolation and suspension design, it can be suppressed to a level comparable to or below the torsion-bar thermal noise in the frequency range of 0.3–1 Hz.

4.5.3 Underground Operation and Future Prospects

To further suppress low-frequency seismic disturbances, CHRONOS is designed to operate in an underground environment. Underground sites significantly reduce wind-driven and anthropogenic vibrations, and also lower the amplitude of the microseismic peak, as demonstrated in KAGRA [12].

Looking ahead, further improvements are expected through the combination of dedicated low-vibration platforms, low-frequency tilt isolation systems, and cryogenic suspension control. These developments aim to achieve an effective vibration level below 10^{-18} m/ $\sqrt{\text{Hz}}$ even around 0.1 Hz.

In this regime, Newtonian noise and thermal noise become dominant, and CHRONOS approaches a truly gravity-gradient-limited operation. Therefore, while seismic noise represents a major technical challenge in sub-Hz interferometry, it can be sufficiently controlled through advanced isolation techniques and underground deployment, and does not constitute the ultimate sensitivity limit of CHRONOS.

4.6 Rayleigh-wave Newtonian Noise

In this work, we evaluate Newtonian noise (NN) arising from density fluctuations induced by Rayleigh waves propagating along the Earth's surface. Unlike seismic

noise, which originates from mechanical motion, Newtonian noise is caused by time-varying gravitational fields generated by density perturbations in the surrounding medium. These gravitational fluctuations directly act on the test masses, and therefore cannot be mitigated by mechanical isolation [90, 50]. As a result, Newtonian noise constitutes a fundamental environmental limit for gravitational-wave detectors in the sub-Hz frequency band.

In the following, we summarize the conversion from ground displacement to torsion-bar angular noise based on the approximation derived by Harms [50].

4.6.1 Gravitational Perturbation from Rayleigh Waves

Rayleigh waves are surface waves localized near the ground, involving both vertical and horizontal motion. These motions induce time-dependent density perturbations, which in turn generate fluctuations in the gravitational potential [50].

Let $S_x^{\text{ground}}(\Omega)$ denote the amplitude spectral density of the vertical ground displacement. The corresponding displacement noise induced by Newtonian gravity on a test mass located at depth d is approximately given by

$$\sqrt{S_R(\Omega)} \simeq \frac{2\pi G \rho_0 \gamma_R}{\Omega^2} \langle |\cos \theta| \rangle \sqrt{S_x^{\text{ground}}(\Omega)} \exp\left(-\frac{\Omega d}{c_R}\right), \quad (4.27)$$

where G is the gravitational constant, ρ_0 is the mean ground density, c_R is the Rayleigh-wave phase velocity, and γ_R is a dimensionless coupling factor relating ground displacement to gravitational perturbation. The angle θ denotes the propagation direction of the wave relative to the detector axis. Assuming an isotropic distribution of incoming waves,

$$\langle |\cos \theta| \rangle = \frac{1}{\sqrt{2}}. \quad (4.28)$$

The exponential factor describes the attenuation of Rayleigh-wave-induced gravity perturbations with depth, demonstrating the advantage of underground installation [50, 12].

4.6.2 Differential Gravity Gradient

In a torsion-bar detector, the observable is the differential gravitational force acting on the two end test masses. In the long-wavelength (short-baseline) limit,

$$\frac{\Omega L_{\text{bar}}}{c_R} \ll 1, \quad (4.29)$$

the differential displacement induced by gravity gradients can be approximated as

$$\sqrt{S_{\text{GG,R}}(\Omega)} \simeq \mathcal{O}_R \left(\frac{\Omega L_{\text{bar}}}{c_R} \right) \sqrt{S_R(\Omega)}, \quad (4.30)$$

where \mathcal{O}_R is a geometric factor arising from directional averaging. For isotropic wave incidence,

$$\mathcal{O}_R = \sqrt{\langle \cos^4 \theta \rangle} = \sqrt{\frac{3}{8}}. \quad (4.31)$$

Under the free-mass approximation, the corresponding differential acceleration is

$$\sqrt{S_{\Delta a}(\Omega)} = \Omega^2 \sqrt{S_{\text{GG,R}}(\Omega)}. \quad (4.32)$$

4.6.3 Conversion to Torsional Angular Noise

For a torsion bar of length L_{bar} with test masses M at both ends, the differential acceleration produces a torque

$$\sqrt{S_\tau(\Omega)} = \frac{L_{\text{bar}}}{2} M \sqrt{S_{\Delta a}(\Omega)}. \quad (4.33)$$

This torque is converted into angular fluctuations through the mechanical susceptibility $\chi(\Omega)$:

$$\sqrt{S_\theta(\Omega)} = |\chi(\Omega)| \sqrt{S_\tau(\Omega)}. \quad (4.34)$$

Finally, the equivalent interferometric signal is given by

$$\sqrt{S_{\text{NN}}(\Omega)} = \frac{\eta_g}{L_{\text{bar}}} \sqrt{S_\theta(\Omega)}. \quad (4.35)$$

4.6.4 Role in CHRONOS and Design Implications

Unlike seismic noise, Newtonian noise arises from direct gravitational coupling, and thus cannot be suppressed by mechanical isolation [90]. Once seismic noise is sufficiently reduced, Newtonian noise becomes the dominant environmental limitation in the sub-Hz band.

In the optimized CHRONOS design, Newtonian noise dominates below approximately 0.1–0.3 Hz. In this regime, both torsion-bar thermal noise and seismic noise are already suppressed, and the detector sensitivity is ultimately limited by environmental gravity fluctuations.

Further mitigation therefore requires underground deployment and active subtraction techniques using environmental sensor arrays, as investigated for advanced detectors [50].

Therefore, Rayleigh-wave Newtonian noise sets the ultimate environmental sensitivity limit of CHRONOS, and plays a central role in defining the achievable performance in the sub-Hz observation band.

Table 4.1: Fundamental constants, environmental parameters, and assumed optical and mechanical parameters used in the noise and sensitivity calculations for the CHRONOS interferometer. In the CHRONOS phase convention, the detuning phase of the PRC is defined with respect to the 0° baseline, whereas both the SRC and the homodyne detection phase are referenced to the 90° baseline.

Parameter	Symbol	Value
<i>Fundamental constants and environmental parameters</i>		
Gravitational constant	G	$6.67430 \times 10^{-11} \text{ m}^3 \text{ kg}^{-1} \text{ s}^{-2}$
Boltzmann constant	k_B	$1.380649 \times 10^{-23} \text{ J K}^{-1}$
Mean ground density	ρ_0	2000 kg m^{-3}
Rayleigh coupling factor	γ_R	0.83
Rayleigh phase velocity	c_R	3500 m s^{-1}
Depth of observatory	d	200 m
Angular average	$\langle \cos \theta \rangle_{\text{rms}}$	$1/\sqrt{2}$
Orientation factor	\mathcal{O}_R	$\sqrt{3/8}$
Young's modulus	Y_s	425 GPa
Poisson ratio	σ_s	0.1
Resonant frequency of ETM stage	ω_{ETM}	$2\pi \times 2.0 \times 10^{-3} \text{ s}^{-1}$
Internal mode frequency	ω_{tb}	$2\pi \times 667 \text{ s}^{-1}$
Pre-isolation stage gain	G_{pre}	1000
Temperature of ETM	T	8 K
Wire mechanical loss angle	ϕ_0	1.0×10^{-7}
Coating mechanical loss angle	ϕ_c^{eff}	1.0×10^{-6}
Substrate mechanical loss angle	ϕ_s^{eff}	1.0×10^{-7}
<i>Optical parameters</i>		
Signal-recycling mirror reflectivity	R_s	0.5
Power-recycling mirror reflectivity	R_p	0.9
Input test-mass reflectivity	R_i	0.9999
Input laser power	P_{in}	1 W
Circulating power in arm cavity	P_{arm}	444 W
PRC detuning phase	ϕ_p	-85°
SRC detuning phase	ϕ_s	0°
Homodyne detection angle	ζ	46°
Ring-cavity finesse	\mathcal{F}	3.14×10^4
Beam radius on ETM	w	2.6 mm

CHRONOS Interferometer

5.1 Optical layout

Figure 5.1 shows the optical layout of the CHRONOS interferometer. The instrument is based on a cross-shaped torsion-bar configuration, with identical optical systems arranged symmetrically along the X and Y arms. This configuration is optimized to extract the differential signal associated with the rotational degree of freedom of the torsion bar, while efficiently suppressing common-mode disturbances such as seismic motion and laser intensity fluctuations. Common-mode rejection is a central design principle in modern gravitational-wave interferometers [1, 6], and is particularly crucial in the sub-Hz band, where environmental noise sources are dominant.

The interferometer employs a single-frequency laser at a wavelength of 1064 nm, with an input power of 1 W. This wavelength is widely used in current ground-based gravitational-wave detectors, owing to the maturity of laser and coating technologies [1]. The chosen power level represents a balance between achieving sufficient circulating power for signal amplification and mitigating thermal effects such as optical absorption and thermal lensing.

The input laser first passes through a Pre-Stabilized Laser (PSL) system, where both frequency and intensity are actively stabilized. In the sub-Hz regime, laser frequency noise couples directly to the interferometric signal, making low-frequency stabilization at the PSL stage essential [6]. Furthermore, the relative intensity noise (RIN) must be sufficiently suppressed to minimize residual coupling into the differential readout

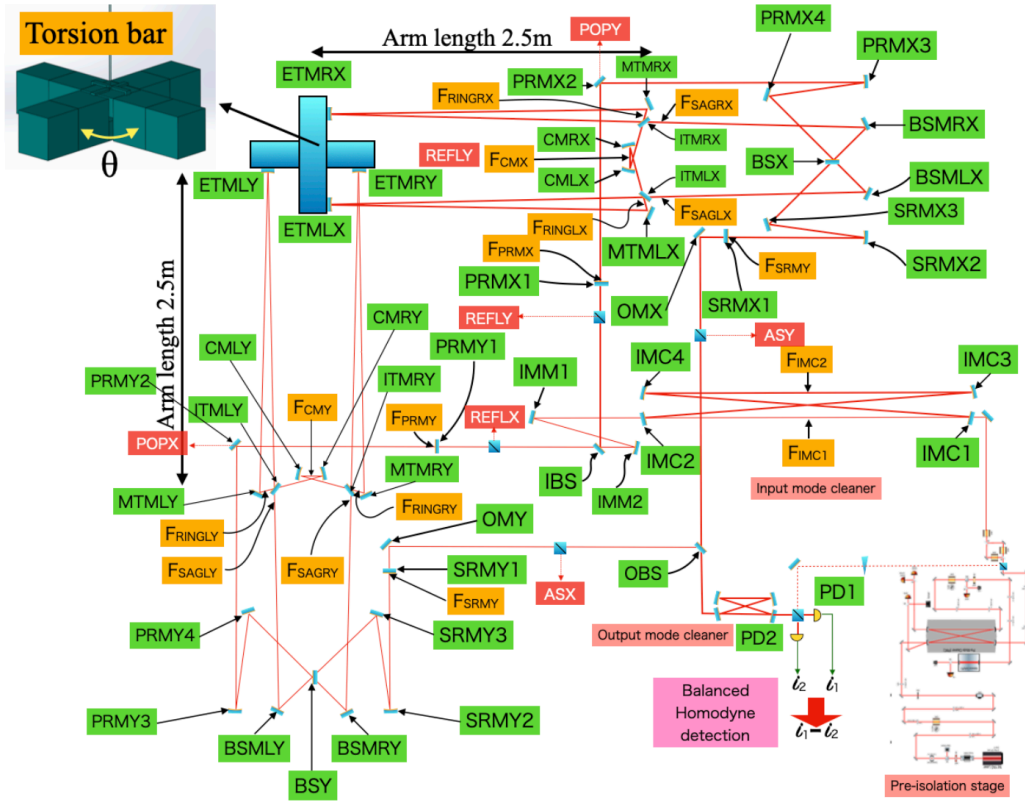


Figure 5.1: Optical layout of the CHRONOS interferometer. The laser stabilized by the PSL and IMC is split by the IBS and injected into two symmetric triangular Sagnac ring cavities. The returning beams are recombined at the OBS, and the signal is extracted through the SRM and OMC before being read out by balanced homodyne detection (BHD).

channel [104]. The detail of PSL system is summarized in Sec. 7.

The beam is then spatially filtered by an Input Mode Cleaner (IMC). The IMC operates as a high-finesse optical bow-tie cavity that transmits only the TEM₀₀ mode, effectively removing higher-order spatial modes and beam jitter. It also serves as a frequency filter, suppressing high-frequency phase noise and unwanted modulation sidebands [1, 6]. As a result, the beam delivered to the interferometer achieves high mode purity and optimal mode matching to the downstream cavities.

After the IMC, the beam is split equally into the X and Y arms by the Input Beam Splitter (IBS). Symmetric power splitting is essential for precise differential measurement, as implemented in Michelson-type interferometers [1].

In each arm, the beam is injected into a triangular Sagnac ring cavity. A defining feature of this configuration is that the interferometer measures the *velocity* of the test mass rather than its displacement. This realizes a quantum nondemolition (QND) speed-meter configuration [27, 85, 35]. In such a topology, the circulating light accumulates a phase shift proportional to the time derivative of the torsional motion. This leads to suppression of radiation-pressure noise at low frequencies, a key advantage for sub-Hz interferometry [27, 35].

After circulating in the ring cavity, the beams are recombined at the Output Beam Splitter (OBS), where the differential phase shift between the X and Y arms is converted into intensity modulation.

The signal is further processed by a Signal Recycling Mirror (SRM), which shapes the frequency response of the interferometer by forming a coupled cavity with the main interferometer [76, 78]. Signal recycling allows tuning of the bandwidth and peak sensitivity, a standard technique in advanced interferometric detectors [1].

An Output Mode Cleaner (OMC) removes residual higher-order modes and unwanted radio-frequency sidebands prior to detection, ensuring high readout purity.

The final readout is performed using balanced homodyne detection (BHD), which enables selection of the optimal quadrature of the optical field [48]. BHD provides control over the trade-off between shot noise and radiation-pressure noise, allowing quantum-noise-limited sensitivity in the measurement band [35].

As a future upgrade, a silicon-based cryogenic configuration is under consideration. In such a case, the laser wavelength would be shifted to 1550 nm to reduce optical absorption in silicon substrates and coatings [42, 30]. Cryogenic silicon interferometers are promising candidates for next-generation low-frequency gravitational-wave detectors.

For clarity, the following discussion focuses on the Y arm, while the X arm has an identical optical configuration.

5.1.1 Triangular Sagnac ring cavity

The central optical element of each arm is a triangular Sagnac ring cavity formed by the Input Test Mass (ITM), Middle Test Mass (MTM), and End Test Mass (ETM). Triangular ring cavities are widely used in interferometric systems because they provide spatial separation between input and output beams within a single plane and allow stable eigenmode control [67, 96]. These ring cavities are arranged symmetrically on either side of the torsion bar, and the light circulates unidirectionally along a closed triangular path.

In CHRONOS, while the left and right rings are geometrically symmetric, the injection point is intentionally offset from the geometric center of the ring. This asymmetry uniquely determines the circulation direction and optical path, thereby ensuring stable Sagnac operation. Such lifting of path degeneracy is a practical consideration in Sagnac speed-meter implementations [27, 85]. In addition, the asymmetric injection clarifies the separation of reflected and transmitted beams, which is advantageous for routing control beams and signal beams independently.

The ring cavity acts as a resonator that accumulates the small optical path length variations induced by the torsional motion of the bar as phase modulation. Under resonant conditions, the phase shift acquired over one round trip is effectively enhanced by the cavity buildup factor, a standard property of optical resonators [96]. The triangular configuration enables a clear spatial separation of the input, circulating, and returning beams within a single plane, which significantly simplifies alignment control and mode matching. Furthermore, the three-mirror geometry defined by ITM, MTM, and ETM provides flexibility in accommodating geometrical constraints such as installation footprint and beam height, making it well suited for an instruments.

A key feature of the Sagnac topology is that the interferometer responds to the *velocity* of the test mass rather than its displacement. This realizes a quantum nondemolition (QND) speed-meter configuration [27, 85, 35]. In such a topology, phase contributions from effectively counter-propagating optical paths cancel for low-frequency common displacement components, while the time-varying (velocity) component remains in the output signal. This velocity response suppresses radiation-pressure noise

at low frequencies, which otherwise limits displacement-based interferometers [35]. This property provides a fundamental advantage for CHRONOS in the sub-Hz frequency band.

In this section, we focus on the conceptual role of the topology, while a quantitative formulation of the speed-meter response and the associated quantum noise will be discussed in later sections.

5.1.2 Coupling between the torsion bar and the ring cavities

Triangular Sagnac ring cavities are installed on both sides of the torsion bar. When the bar undergoes a small angular rotation, the effective optical path lengths in the left and right cavities change with opposite signs. This behavior follows directly from geometric phase considerations in interferometric rotation sensing.

As a result, when the returning beams from the two cavities are interfered, the torsional motion is extracted as a differential phase signal. Differential readout is the standard strategy in precision interferometry to suppress common-mode noise sources [1, 6].

Perturbations that act similarly on both sides, such as laser intensity fluctuations and structural vibrations, appear predominantly as common-mode signals and are therefore strongly canceled in the differential channel. Likewise, provided that the optical power and phase reference supplied to each arm from the IBS are balanced, a large fraction of laser-induced noise is intrinsically suppressed [1]. Consequently, the differential output is dominated by the intrinsic angular response of the torsion bar.

In this way, the mechanical system (torsion bar) shown in Fig. 5.2 and the optical system consisting of triangular Sagnac ring cavities are clearly distinct subsystems. The fundamental detection principle of CHRONOS is realized through the coupling between these two systems. In particular, the Sagnac topology naturally provides a velocity-sensitive response proportional to the time derivative of the torsional motion [27]. This feature leads to suppression of radiation-pressure noise at low frequencies, offering a key advantage for achieving high sensitivity in the sub-Hz band.

5.1.3 Dual-recycling configuration with PR-dominated operation

The CHRONOS interferometer employs a dual-recycling configuration, consisting of both power recycling (PR) and signal recycling (SR), as originally proposed for advanced interferometric detectors [76, 78]. While both subsystems contribute to the interferometer performance, their roles are fundamentally different and asymmetric in importance.

The PR system is implemented on the input side using a set of mirrors (PRM1–PRM4) and the beam splitter (BS), forming a coupled resonant system shared by the two Sagnac arms. Power recycling increases the effective circulating power without increasing the input laser power, thereby improving the shot-noise-limited sensitivity [76]. Since shot noise scales inversely with the square root of the circulating power, $S_h^{\text{shot}} \propto P_{\text{circ}}^{-1/2}$, the PR configuration directly determines the overall sensitivity scale [35].

This role is particularly critical in CHRONOS, where the input laser power is modest (1 W) and the target frequency band lies in the sub-Hz regime. In this regime, achieving sufficient circulating power without introducing excessive thermal or technical noise requires careful optimization of the PR cavity parameters, including reflectivity, cavity length, and mode matching [1]. Therefore, the PR system acts as the primary lever for sensitivity optimization in the interferometer.

On the output side, a Signal Recycling Mirror (SRM) is employed to form a signal-recycling cavity (SRC). Signal recycling modifies the interferometer transfer function by forming a coupled cavity with the main interferometer, allowing tuning of bandwidth and peak sensitivity [78, 20]. By adjusting the microscopic detuning phase of the SRM, the frequency dependence of the response can be shaped, enhancing sensitivity in selected frequency ranges.

However, in contrast to kilometer-scale interferometers, where signal recycling plays a central role in broadband sensitivity optimization, the impact of SR tuning in CHRONOS is secondary. In the sub-Hz band, the sensitivity is influenced not only by quantum noise but also by technical and environmental noise sources, which limits the extent to which SR alone can improve performance. As a result, SR in CHRONOS serves

primarily as a complementary tool for fine-tuning the frequency response, while the PR system determines the baseline sensitivity.

The output optical field is filtered by an Output Mode Cleaner (OMC), which suppresses higher-order spatial modes and control sidebands by tens of decibels [1]. The OMC acts as a spatial and spectral filter, ensuring that only the fundamental mode carrying the signal sidebands reaches the photodetector. This reduces technical noise sources such as mode beating and scattered-light-induced fluctuations, and improves the fidelity of the detected signal.

The filtered output is read out using balanced homodyne detection (BHD), in which the interferometer output field is mixed with a local oscillator (LO), and the differential photocurrent is measured [48, 35]. BHD enables measurement of an arbitrary optical quadrature, allowing optimization of the quantum noise balance between shot noise and radiation-pressure noise. Compared to conventional DC readout schemes, balanced homodyne detection offers improved suppression of technical noise couplings at low frequencies.

In summary, the dual-recycling configuration in CHRONOS is characterized by a PR-dominated design. The circulating power enhancement and mode matching provided by the PR system set the overall sensitivity scale, while the SR configuration provides secondary control over the frequency-dependent response. A quantitative evaluation of these subsystems will be presented in the sensitivity analysis section.

5.2 Torsion bar

The central mechanical element of CHRONOS is a cross-shaped torsion-bar test mass. As shown in Fig. 5.2, this figure represents only the conceptual structure of the test mass itself and does not include the optical (ring) cavity. The torsion bar is suspended such that its rotational degree of freedom dominates at low frequencies. It responds to tidal torques induced by gravitational waves, as well as to externally applied calibrated torques, producing a minute angular displacement. Torsion-bar interferometers have been proposed as promising probes of ultra-low-frequency gravitational waves [16]. In CHRONOS, the measurement targets rotational motion rather

than translational displacement, allowing operation as a low-frequency mechanical resonator in the sub-Hz band while benefiting from differential optical readout.

The base material of the torsion bar is sapphire (single-crystal Al_2O_3). Sapphire exhibits a high mechanical quality factor at cryogenic temperatures, low internal friction, and high thermal conductivity [89]. These properties make sapphire a favorable material for cryogenic gravitational-wave detectors such as KAGRA [11]. The high thermal conductivity facilitates heat extraction from optical absorption, while the low mechanical loss reduces suspension and substrate thermal noise [91].

The torsion bar is not necessarily fabricated from a single monolithic block. Instead, it may be constructed by bonding multiple sapphire substrates to achieve the required geometry and moment of inertia. Hydroxy-catalysis bonding is employed to join sapphire substrates with high precision and low mechanical loss, forming a quasi-monolithic structure [49, 88]. This bonding technique has been widely adopted in precision interferometry because it preserves high mechanical quality while enabling flexible fabrication of complex geometries.

The reflective surfaces used for optical readout are coated with multilayer stacks of SiN and SiON. Low mechanical loss dielectric coatings are critical for reducing coating thermal noise [30, 100]. High-density deposition techniques such as LPCVD are expected to achieve low optical absorption and reduced mechanical dissipation. Although this paper focuses on optical topology, it should be emphasized that the test-mass material, coating design, and bonding techniques ultimately determine thermal noise, scattering loss, and absorption limits, and are inseparable from overall instrument performance.

The torsion bar is suspended using sapphire fibers. Cryogenic sapphire suspensions provide both efficient thermal conduction and low internal loss, enabling high-Q rotational modes [11]. The eigenfrequency of the torsional mode, determined by the suspension geometry, moment of inertia, and torsional spring constant, is designed to lie in the sub-Hz band. This enables enhanced sensitivity to ultra-low-frequency gravitational-wave signals.

An alternative implementation using silicon as the substrate material is also possi-

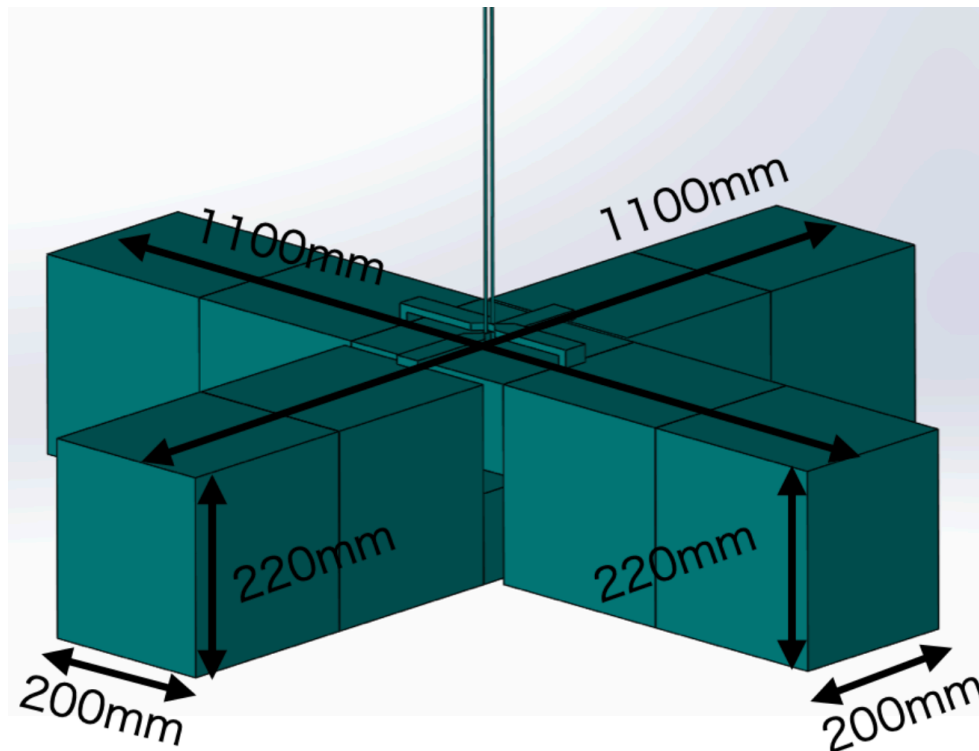


Figure 5.2: Conceptual design of the torsion-bar test mass in CHRONOS.

ble. Silicon exhibits excellent mechanical properties and high thermal conductivity at cryogenic temperatures [93]. However, at 1064 nm silicon has relatively high optical absorption. Therefore, silicon-based interferometers typically operate at 1550 nm to reduce absorption and associated thermal lensing effects [42]. In this study, we primarily consider a sapphire-based system with a 1064 nm laser as the baseline configuration, while recognizing that a silicon-based configuration at 1550 nm remains an important option for future development.

Cavity Control

It is important to clearly define the design philosophy of the optical topology, cavity lengths, recycling configuration, and RF sideband frequencies adopted in this study [76, 78]. The ultimate goal of this system is to construct a laboratory-scale interferometer that faithfully reproduces the physical conditions required for the full-scale CHRONOS detector [58]. Rather than a simple scaled-down model, the design aims to realize a demonstration platform with optical dynamics and control architecture equivalent to those of a large-scale instrument [11].

6.1 Operation method

In this study, a triangular ring Sagnac topology is adopted [27]. This configuration measures the *angular momentum* of the test mass rather than its angular displacement [27]. As a result, radiation-pressure noise is naturally suppressed in the low-frequency regime [27]. This property is essential for extending sensitivity into the sub-Hz band and represents a significant advantage over conventional Michelson configurations.

The interferometer provides a practical experimental platform to verify the following key elements:

- Optical stability (cavity stability)
- Mode matching
- Cavity length control systems [36, 18]

- Recycling phase control [76]
- Quantum-noise readout strategies [110, 43]

In this section, we first present the frequency design framework and then describe the strategy for separating control degrees of freedom.

6.1.1 Sideband Frequencies and Frequency Architecture

The starting point of the design is the round-trip length of the ring cavity. For a triangular Sagnac ring with total length

$$L_{\text{ring}} = 5.08 \text{ m}, \quad (6.1)$$

the free spectral range (FSR) is given by

$$\text{FSR}_{\text{ring}} = \frac{c}{L_{\text{ring}}} \simeq 59.0 \text{ MHz}. \quad (6.2)$$

This ring FSR serves as the fundamental reference for the entire frequency architecture.

Signal Recycling Cavity (SRC)

The SRC is designed such that its free spectral range corresponds to half that of the ring cavity [78]:

$$L_{\text{src}} \simeq 5.08 \text{ m}, \quad \text{FSR}_{\text{src}} \simeq 29.5 \text{ MHz}. \quad (6.3)$$

That is,

$$\text{FSR}_{\text{src}} = \frac{1}{2} \text{FSR}_{\text{ring}}. \quad (6.4)$$

With this design, the SRC satisfies a half-resonance condition with respect to itself while maintaining compatibility with the PRC. This reproduces the resonance and anti-resonance phase relationships established in LIGO within a compact-scale system [76].

Power Recycling Cavity (PRC)

The PRC length is set to

$$L_{\text{prc}} \simeq 7.62 \text{ m}, \quad \text{FSR}_{\text{prc}} \simeq 19.7 \text{ MHz}. \quad (6.5)$$

This value establishes an integer-ratio relationship with the ring cavity and SRC, allowing controlled resonance conditions for selected RF sidebands [76]. Importantly, the optical phase relationships established in kilometer-scale interferometers can be preserved even when scaled down to a system [11]. This design reconstructs the optical configuration through a similarity transformation in frequency space, ensuring equivalent optical dynamics.

6.1.2 RF Sidebands and Degree-of-Freedom Separation

Based on this frequency architecture, two RF sidebands are chosen for the primary control scheme:

$$f_1 = 29.50 \text{ MHz}, \quad f_2 = 58.98 \text{ MHz}. \quad (6.6)$$

The higher-frequency sideband f_2 matches the ring FSR, resulting in:

- Resonance in the PRC
- Anti-resonance in the SRC

This property enables separation of the PRC and SRC degrees of freedom using a single modulation frequency [78].

On the other hand, f_1 matches the SRC FSR and provides high sensitivity to SRC control. By combining these two sidebands, the following degrees of freedom can be controlled in an orthogonal manner [36, 18]:

- PRC length
- SRC length
- Ring resonance condition

This scheme faithfully reproduces the degree-of-freedom separation technique used in large-scale interferometers within a compact experimental system [11].

6.1.3 Input Mode Cleaner (IMC) Compatibility

The input mode cleaner (IMC) plays a crucial role in laser frequency stabilization [36, 18, 69]. It must filter the carrier field while transmitting RF sidebands used for control with minimal loss [69].

The IMC round-trip length is set to

$$L_{\text{IMC}} = 10.2 \text{ m}, \quad \text{FSR}_{\text{IMC}} \simeq 14.8 \text{ MHz}. \quad (6.7)$$

In addition, a dedicated sideband for IMC control is introduced:

$$f_{\text{IMC}} = 44.2 \text{ MHz}. \quad (6.8)$$

With this configuration:

- The carrier is purified by the IMC [69]
- f_1 and f_2 are preserved for interferometer control
- The IMC sideband stabilizes the laser frequency [36, 18]

A key feature is that all frequencies are arranged in integer-ratio relationships with respect to the ring FSR, forming a well-structured frequency architecture. This suppresses unwanted cross-coupling and mode mixing, ensuring clean separation of control signals [78, 76].

6.1.4 Design Philosophy Summary

The cavity control design of the interferometer is based on the following principles [58]:

1. Construction of a frequency architecture referenced to the ring FSR
2. Precise design of resonance and anti-resonance conditions for PRC and SRC [76, 78]
3. Orthogonal separation of degrees of freedom using RF sidebands [36, 18]
4. Frequency compatibility with the IMC [69]

5. Preservation of physical similarity with the full-scale CHRONOS detector [11, 58]

This configuration enables verification of optical stability, phase control, recycling operation, and quantum-noise readout under conditions equivalent to those of a full-scale detector, despite the compact size.

Therefore, this system is not merely a scaled model but a physically equivalent demonstration platform. The performance of the cavity control system is a fundamental technology that determines the achievable sub-Hz sensitivity and constitutes a central component of this study.

6.1.5 Control ports and control scheme

The CHRONOS interferometer adopts a dual-recycled Sagnac configuration [27, 76]. Using multiple detection ports and RF sidebands, the common and differential degrees of freedom of the coupled cavity system are stably controlled. This section systematically describes the overall lock acquisition sequence, including the initial alignment (INI) stage, as well as the definitions and optical roles of each control port [38, 11].

The primary control degrees of freedom are:

- IMC length (laser frequency reference)
- PRC length (common mode)
- SRC length (signal extraction phase)
- Ring cavity resonance condition
- Beam splitter differential phase

Although these degrees of freedom are physically coupled, they can be effectively orthogonalized and extracted as independent error signals through appropriate choices of RF sideband resonance conditions and detection ports [36, 18, 78].

Initial alignment and INI control

The interferometer lock sequence begins with the INI (Initial Alignment) stage. The purpose of this stage is to establish spatial mode matching and phase reference, and to prepare a stable reference beam required for subsequent cavity locking [69].

During the INI stage, the positions and angles of the IMC, PRM, BS, and input steering mirrors are adjusted to stabilize the spatial mode and wavefront phase of the beam injected into the Sagnac interferometer. This process is not merely mechanical alignment, but a critical step that directly impacts mode-matching accuracy and suppression of angular fluctuations during high-sensitivity operation.

The IMC is a four-mirror bow-tie cavity that functions as both a spatial mode filter and a frequency reference [69, 11]. Each mirror is suspended by a single-pendulum system, providing seismic isolation and precise angular control. The IMC length is controlled using the Pound–Drever–Hall (PDH) technique [36, 18] with a modulation frequency

$$f_{\text{IMC}} = 44.2 \text{ MHz}. \quad (6.9)$$

The reflected signal is demodulated at the same frequency to generate an error signal, which is fed back to coil-magnet actuators attached to the end mirror to control the cavity length. This configuration follows the KAGRA-type IMC design [11], employing magnetic actuation instead of piezoelectric elements, thereby achieving large dynamic range and stable low-frequency control.

The transmitted light from the IMC serves as a monitor of spatial mode quality and intensity stability [69]. Its low-frequency component is also used as an offset correction signal in the laser frequency control loop [69]. In this way, the laser frequency is tightly locked to the IMC length, establishing a stable frequency reference for the entire interferometer.

Furthermore, the RF phase reference of the IMC is phase-locked to the modulation sources

$$f_1 = 29.5 \text{ MHz}, \quad f_2 = 59.0 \text{ MHz}. \quad (6.10)$$

This ensures that the demodulation phases at the reflection port (REFL) and pick-off

port (POP) share a common reference, enabling clear separation of control degrees of freedom [78].

Once the INI stage is completed, the input beam is fully stabilized in terms of spatial mode, frequency, and phase, allowing smooth transition to the green pre-lock stage and subsequent PRC/SRC control.

Control ports and optical readout scheme

In this interferometer, the REFL, POP, and AS ports are used to sequentially control the common and differential degrees of freedom of the PRC, SRC, and Sagnac ring [76, 78, 11]. Each port carries different optical information, and by utilizing RF sideband resonance conditions and Gouy phase differences, the coupled degrees of freedom are effectively separated [78].

Reflection port (REFL) The REFL port detects light reflected from the PRC input mirror. It directly monitors the effective reflectivity of the interferometer and provides the primary error signal for the PRC length (PRCL) [76].

The reflected signal is demodulated at

$$f_1 = 29.5 \text{ MHz}, \quad (6.11)$$

and the PRCL error signal is obtained using the Pound–Drever–Hall (PDH) technique [36, 18]. Although f_1 matches the SRC FSR, it provides high sensitivity to the PRC, making it optimal for PRCL control [78].

In addition, the REFL port serves as an auxiliary monitor of the Sagnac common mode (CSAG), i.e., the average optical path length of the clockwise (CW) and counter-clockwise (CCW) beams. This signal is also coupled to the laser frequency stabilization loop, contributing to maintaining the overall interferometer resonance [36].

Pick-off port (POP) The POP port extracts a portion of the intracavity field in the PRC and is designed to sense both common and differential mode components [17].

Two photodiodes are placed at different Gouy phase locations to achieve spatial mode separation [78]:

- **POP-A (near field):** Located near the PRM, it is sensitive to CSAG and PRCL. It is mainly used as an auxiliary signal for common-mode control and laser frequency stabilization.
- **POP-B (far field):** Positioned with a Gouy phase difference of 45° – 90° relative to POP-A, it has high sensitivity to the differential Sagnac mode (DSAG).

Both signals are demodulated at

$$f_2 = 59.0 \text{ MHz.} \quad (6.12)$$

By introducing a Gouy phase difference, mixing between CSAG, PRCL, and DSAG is suppressed, enabling clear separation of each degree of freedom [78]. This reproduces the mode-separation technique used in large-scale interferometers within a compact system [11].

Antisymmetric port (AS) The AS port corresponds to the output (dark) port of the Sagnac interferometer [27]. When the interferometer is in resonance, the carrier is ideally canceled at this port (dark fringe), leaving primarily sidebands and signal components.

The signal demodulated at

$$f_2 = 59.0 \text{ MHz} \quad (6.13)$$

provides the primary error signal for signal recycling cavity length (SRCL) control [38].

The horizontal (ASX) and vertical (ASY) channels detected at the AS port are combined at the output beam splitter (OBS) and decomposed into common and differential components. The differential component reflects the relative angular motion of the mirrors and constitutes the science signal.

This differential AS signal is sent to the output mode cleaner (OMC), and the DSAG signal is finally extracted via balanced homodyne detection [43, 110]. The measured observable corresponds to velocity rather than displacement, functioning as a speed-meter observable, which is a key feature of the CHRONOS configuration [27].

Comparison with Michelson configuration The DSAG degree of freedom corresponds to the DARM degree of freedom in a Michelson interferometer, but its physical meaning differs.

In the CHRONOS configuration, DSAG represents an angular-momentum-type observable arising from the propagation velocity difference between CW and CCW beams, rather than a simple displacement [27].

Similarly, CSAG corresponds to the Michelson CARM degree of freedom, representing the common optical path length strongly coupled to laser frequency and PRC resonance [76]. Thus, while the correspondence of degrees of freedom is preserved, the physical observables are extended to angular-momentum-type quantities, which is a defining feature of the dual-recycled Sagnac configuration [27].

Table 6.1 summarizes the main detection ports and their corresponding control degrees of freedom. During the IMC-INI stage, IMCL is stabilized using a 44.2 MHz PDH signal [36], after which PRCL, CSAG, DSAG, and SRCL are sequentially locked using the REFL, POP, and AS ports [11]. The final science signal is obtained as a DC readout at the AS-BHD port, where the DSAG velocity component is measured as a speed-meter observable [43, 27].

In this way, by combining multiple ports and phase-coherent RF sidebands, a consistent control scheme is realized that stably controls a coupled multi-degree-of-freedom cavity system while enabling a quantum-noise-limited speed-meter readout [110].

Lock acquisition strategy

Lock acquisition proceeds in stages:

1. IMC lock (establish frequency reference)
2. PRC lock (establish common mode)
3. SRC lock (establish signal extraction phase)
4. Full ring resonance

Table 6.1: Major detection ports and their corresponding control degrees of freedom in the CHRONOS dual-recycled Sagnac interferometer. The top row, IMC-INI, represents the initial-alignment and frequency-reference stage in the IMC, where the IMCL is stabilized using a 44.2 MHz Pound–Drever–Hall (PDH) signal. The subsequent ports—REFL, POP, and AS—are used to sense and control the common and differential DOFs of the main dual-recycled Sagnac interferometer (PRCL, CSAG, DSAG, and SRCL). All RF ports employ phase-coherent modulation sidebands at $f_1 = 29.5$ MHz and $f_2 = 59.0$ MHz, which correspond to the resonance conditions of the PRC and the SRC, respectively. The final port, AS-BHD, is a DC readout channel that extracts the velocity component of the DSAG as the speed-meter signal, which constitutes the scientific output of the interferometer. The physical locations of the individual detection and control ports are illustrated in Fig. 5.1.

Port	RF freq.	Main DOF	Role	Remark
IMC-INI	44.2 MHz	IMCL	IMC length and alignment control	Four-mirror suspended bow-tie cavity
REFL	29.5 MHz	PRCL, CSAG	PRC and common path-length control	Also used for frequency stabilization
POP-A	59.0 MHz	PRCL (aux), CSAG	Common Sagnac mode monitor	Near-field pick-off
POP-B	59.0 MHz	DSAG	Differential Sagnac control	Far-field pick-off
AS	59.0 MHz	SRCL	Signal-recycling cavity control	Output port (dark fringe)
AS-BHD	DC	Science (DSAG velocity)	Speed-meter readout	Phase-quadrature homodyne detection

At each stage, loop gain and bandwidth are adjusted to minimize cross-coupling between degrees of freedom [11]. In particular, since PRC and SRC are strongly coupled, the phase choice of f_1 and f_2 is critical for control stability [78].

Thus, the control system of the CHRONOS interferometer is based on the same frequency-domain separation principles as large-scale interferometers [76], while being adapted for stable operation at laboratory scale. The spatial arrangement of the control readout ports is shown in Fig. 5.1.

Input Optics

The Input Optics system constitutes the pre-stabilization stage that delivers spatially pure, frequency-stabilized, and intensity-stabilized laser light to the main interferometer. In CHRONOS, a torsion-bar speed-meter interferometer operating in the sub-Hz regime, the requirements on low-frequency laser noise are particularly stringent. Therefore, the Input Optics is not merely a beam-conditioning stage, but a multi-layer stabilization architecture designed to independently control three essential degrees of freedom: spatial mode, frequency, and intensity.

A schematic layout of the Input Optics system is shown in Fig. 7.1. Light emitted from the seed laser is conditioned through electro-optic and acousto-optic modulation, filtered by the Input Mode Cleaner (IMC), stabilized in frequency by the Reference Cavity (RC), and subsequently delivered to the main interferometer.

The system is composed of the following primary components:

- Seed laser (Nd:YAG, 1064 nm)
- Steering mirrors and mode-matching optics
- Electro-Optic Modulator (EOM)
- Acousto-Optic Modulator (AOM)
- Input Mode Cleaner (IMC)
- Reference Cavity (RC)

The central element of the system is the Input Mode Cleaner (IMC), configured as a four-mirror bow-tie ring cavity. This traveling-wave configuration suppresses optical

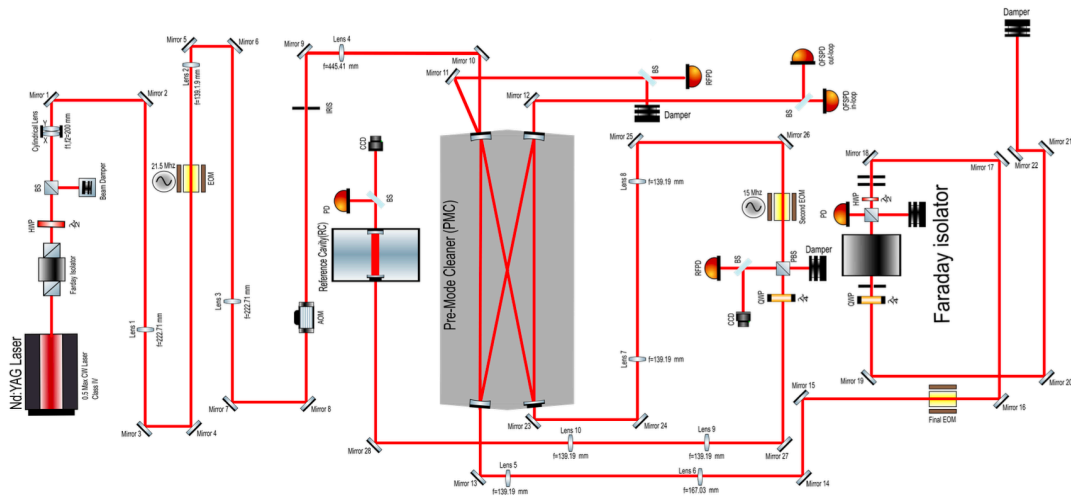


Figure 7.1: Optical layout of the CHRONOS Input Optics system. The seed laser output passes through the EOM, AOM, Input Mode Cleaner (IMC), and Reference Cavity (RC) before entering the main interferometer.

back-reflection toward the laser source and mitigates parasitic interference caused by scattered light. Such suppression is especially critical in the sub-Hz frequency band, where scattered light can couple ground motion into phase noise.

The IMC spatially filters the incoming beam by selecting the TEM_{00} eigenmode of the cavity, thereby suppressing higher-order transverse modes and improving spatial mode purity. In a speed-meter interferometer, spatial mode imperfections can couple into the velocity signal, potentially degrading sensitivity. Maintaining high spatial mode quality at the input stage is therefore essential for preserving detector performance.

Both reflected and transmitted beams from the IMC are utilized for downstream control systems. The reflected beam provides the error signal required to maintain the IMC resonance condition. The transmitted beam is split into multiple paths:

- A fraction is used for intensity stabilization (Intensity Stabilization servo),
- A fraction is directed to the Reference Cavity (RC) for frequency stabilization,
- The remaining portion serves as the input to the main interferometer.

The Reference Cavity (RC) functions as a high-stability optical frequency reference.

Laser frequency stabilization is achieved using the Pound-Drever-Hall (PDH) technique, which enables significant suppression of low-frequency frequency noise. This stage is particularly important for CHRONOS, where laser frequency noise can couple to the torsional degree of freedom through residual asymmetries and cavity-length fluctuations.

Both the IMC and RC are equipped with active thermal stabilization systems to minimize cavity-length fluctuations induced by environmental temperature variations. Such stabilization further suppresses low-frequency drift and enhances long-term operational stability.

In summary, the CHRONOS Input Optics system is designed as an integrated stabilization architecture. By simultaneously controlling spatial mode quality, frequency noise, and intensity noise, it provides a high-purity and ultra-stable laser source required for sub-Hz gravitational-wave detection with a torsion-bar speed-meter interferometer.

7.1 Pre-Mode Cleaner (PMC)

The Pre-Mode Cleaner (PMC) serves as the first optical filtering stage in the CHRONOS Input Optics chain. While often regarded as a simple pre-stabilization cavity, its role is scientifically essential for enabling ultra-low-frequency operation of the torsion-bar speed-meter interferometer.

Figure 7.2 shows the mechanical and optical structure of the PMC. It is implemented as a bow-tie traveling-wave ring cavity with a total length of $L = 0.5$ m. The traveling-wave configuration suppresses back-reflection into the laser source, thereby preventing optical feedback-induced frequency noise, which is particularly detrimental in sub-Hz interferometry.

7.1.1 Scientific Role of the PMC

The PMC fulfills several critical functions:

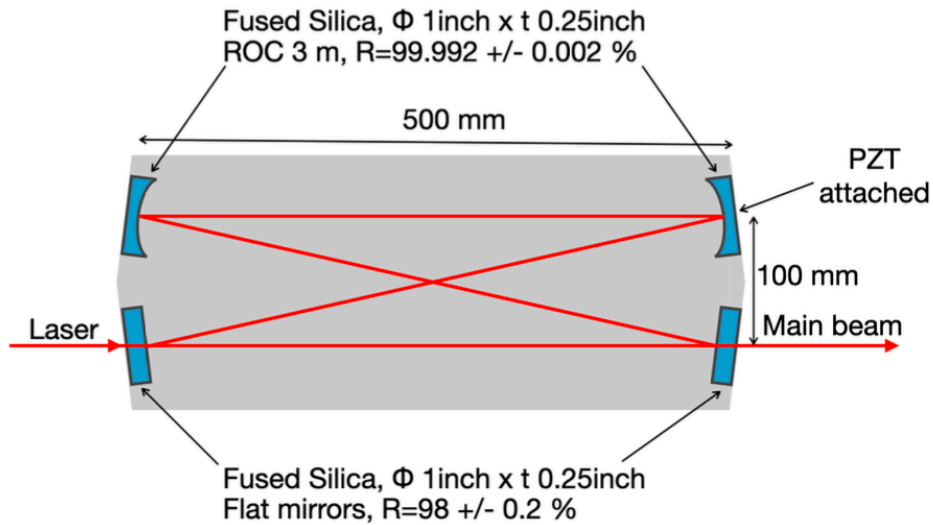


Figure 7.2: Schematic configuration of the pre-mode-cleaner (PMC) cavity. The cavity consists of two concave high-reflectivity mirrors (ROC = 3 m, $R = 99.992\% \pm 0.002\%$) separated by 500 mm, and two flat mirrors ($R = 98\% \pm 0.2\%$), forming a folded linear cavity. The mirror substrates are fused silica ($\phi 1$ inch \times 0.25 inch). One of the end mirrors is mounted on a piezoelectric transducer (PZT) for cavity length control. The main transmitted beam is extracted from the output coupler.

(i) Spatial Mode Filtering The cavity transmits only the TEM_{00} eigenmode and suppresses higher-order transverse spatial modes. Residual spatial mode distortion couples to interferometer alignment degrees of freedom and can convert beam jitter into phase noise. In a speed-meter configuration, such coupling may contaminate the velocity signal, making spatial purity at the earliest stage indispensable.

(ii) High-Frequency Intensity Noise Filtering Above the cavity pole frequency, the PMC acts as a low-pass filter for laser intensity noise. The cavity transfer function for amplitude fluctuations is

$$H(f) = \frac{1}{1 + if/f_c}, \quad (7.1)$$

where f_c is the cavity pole frequency. This passive filtering reduces high-frequency relative intensity noise (RIN) before the beam enters the active intensity stabilization servo, thereby relaxing its control bandwidth requirements.

(iii) Preliminary Frequency Conditioning Although the Reference Cavity (RC) provides the primary frequency reference, the PMC suppresses frequency fluctuations outside its linewidth. The cavity resonance converts frequency noise into transmitted power fluctuations, which are actively suppressed by the PDH locking loop. This stage reduces the dynamic range required for the RC actuator and improves lock acquisition robustness.

(iv) Isolation from Back-Scattered Light Back-scattered light from downstream optics, including the IMC and main interferometer, can re-enter the laser and produce excess phase noise. The traveling-wave geometry of the PMC significantly reduces this feedback. This is particularly important in the sub-Hz regime, where scattered light beating with ground motion can generate excess low-frequency noise.

(v) Control Noise Decoupling The PMC acts as an optical buffer between the laser source and the IMC. Without this intermediate stage, frequency and amplitude noise would directly drive the IMC control loop, increasing control noise injection into the main interferometer. By reducing upstream noise, the PMC improves overall control-loop stability.

7.1.2 Pound–Drever–Hall Frequency Discrimination

Phase modulation sidebands are generated using an Electro-Optic Modulator (EOM). The modulated beam is injected into the high-finesse Reference Cavity (RC), and the reflected field is detected to obtain a frequency error signal.

The reflected beam is separated by a Polarizing Beam Splitter (PBS) and detected with a radio-frequency photodetector (RFPD). Using the Pound–Drever–Hall (PDH) method, the detuning between the laser frequency and the cavity resonance is extracted as

$$V_{\text{err}} \propto \Im(E_{\text{carrier}} E_{\text{sideband}}^*). \quad (7.2)$$

Near resonance, the PDH error signal is linear with frequency deviation, allowing

high-precision discrimination. The slope of the discriminator is proportional to the cavity finesse \mathcal{F} , which enhances frequency sensitivity.

7.1.3 Optical and Mechanical Parameters

The cavity consists of two curved mirrors (ROC = 3 m, $R = 99.992\%$) and two flat mirrors ($R = 98\%$), all made of fused silica. One mirror is mounted on a piezoelectric actuator (PZT) for cavity-length control using the Pound-Drever-Hall method.

The free spectral range is

$$\text{FSR} = \frac{c}{L} \approx 600 \text{ MHz}, \quad (7.3)$$

ensuring large longitudinal mode spacing and stable locking.

7.1.4 Thermal Stability Considerations

The housing is fabricated from 6061 aluminum alloy. Although its high thermal conductivity promotes uniform temperature distribution, its relatively large thermal expansion coefficient ($\alpha = 2.32 \times 10^{-5} \text{ K}^{-1}$) introduces cavity-length sensitivity to temperature fluctuations.

The induced cavity-length variation is

$$\delta L = \alpha L \delta T. \quad (7.4)$$

A temperature fluctuation of 1 mK yields

$$\delta L \approx 1.2 \times 10^{-8} \text{ m}. \quad (7.5)$$

Such fluctuations correspond to resonance-frequency drift, which can couple to downstream frequency stabilization stages. Therefore, active temperature control of the PMC housing is implemented to suppress low-frequency thermal noise.

7.1.5 Importance for Sub-Hz Operation

In conventional high-frequency gravitational-wave detectors, the PMC primarily serves as a spatial filter. However, for CHRONOS operating in the sub-Hz regime, the PMC plays a deeper role: it suppresses laser noise that would otherwise couple through residual asymmetries, control loops, or scattered light paths into the torsional degree of freedom.

The PMC thus constitutes an essential noise-conditioning stage that enables the realization of quantum-noise-limited speed-meter sensitivity at ultra-low frequencies.

7.2 Intensity Stabilization

Laser Relative Intensity Noise (RIN) is one of the fundamental technical noise sources in interferometric gravitational-wave detectors. For CHRONOS, a torsion-bar speed-meter interferometer operating in the sub-Hz regime, intensity fluctuations are particularly critical. Laser power fluctuations couple directly to radiation-pressure torque, which in turn drives angular displacement of the torsion bar. Therefore, intensity stabilization at low frequencies is indispensable for achieving the target sensitivity.

In the present system, an Acousto-Optic Modulator (AOM) is used as the intensity actuator, and an analog Optical-Follower Servo (OFS) provides feedback control.

7.2.1 Physical Coupling of Intensity Noise

A fluctuation in optical power δP induces a fluctuation in radiation-pressure force. For a torsion-bar interferometer, this force produces a torque about the rotational axis.

To leading order, the torque fluctuation is approximated as

$$\delta\tau = \frac{2L}{c} \delta P, \quad (7.6)$$

where L is the lever arm from the beam spot to the rotation axis, and c is the speed of light.

The angular response of the torsion bar is given by

$$\theta(\Omega) = \frac{\delta\tau(\Omega)}{I(\Omega_0^2 - \Omega^2 + i\Omega\Gamma)}, \quad (7.7)$$

where I is the moment of inertia, Ω_0 the torsional resonance frequency, and Γ the damping rate.

At frequencies well above resonance ($\Omega \gg \Omega_0$),

$$\theta(\Omega) \approx \frac{2L}{cI\Omega^2} \delta P(\Omega). \quad (7.8)$$

Thus, intensity fluctuations exhibit a $1/\Omega^2$ enhancement in angular displacement at low frequencies, making RIN suppression increasingly important toward the sub-Hz band.

Expressed in terms of relative intensity noise, $\text{RIN} = \delta P/P$, the induced angular noise becomes

$$\theta_{\text{RIN}}(\Omega) = \frac{2LP}{cI\Omega^2} \text{RIN}(\Omega). \quad (7.9)$$

This relation explicitly shows that radiation-pressure-induced angular noise scales linearly with optical power and inversely with Ω^2 . Consequently, even modest low-frequency RIN can limit the CHRONOS sensitivity.

7.2.2 Intensity Stabilization Architecture

After passing through the AOM, the laser beam enters the PMC. The transmitted beam is split and detected by two photodiodes:

- **OFSPD-in:** in-loop detector
- **OFSPD-out:** out-of-loop detector

The OFSPD-in signal provides the error signal for the Optical-Follower Servo (OFS). The OFS drives the AOM RF amplitude, thereby modulating the diffraction efficiency and stabilizing the output optical power.

The OFSPD-out detector is located outside the feedback loop and independently monitors the achieved RIN suppression. Since in-loop measurements are artificially reduced by the loop gain, out-of-loop verification is essential to quantify the true stabilization performance.

7.2.3 Optical-Follower Servo (OFS)

The OFS consists of two primary subsystems:

- Power Stabilization Servo (PSS)
- Interface chassis

The PSS processes the photodiode signal and generates the control signal for the AOM. The interface chassis routes diagnostic signals to the data acquisition system, allowing continuous monitoring of loop performance.

The closed-loop residual intensity noise is given by

$$S_{\text{closed}}(f) = \frac{S_{\text{free}}(f)}{1 + G(f)}, \quad (7.10)$$

where $G(f)$ is the open-loop gain. In the frequency band where $|G(f)| \gg 1$, the RIN is suppressed approximately by a factor $1/G(f)$.

7.2.4 Control Loop Characteristics

The measured transfer function of the intensity stabilization loop is shown in Fig. 7.3. An open-loop gain of approximately 30 dB is achieved in the low-frequency band, with sufficient phase margin to ensure stable operation.

The unity-gain frequency is chosen to balance RIN suppression and control noise injection. Excessive bandwidth would increase sensing noise coupling, while insufficient bandwidth would leave low-frequency RIN unsuppressed.

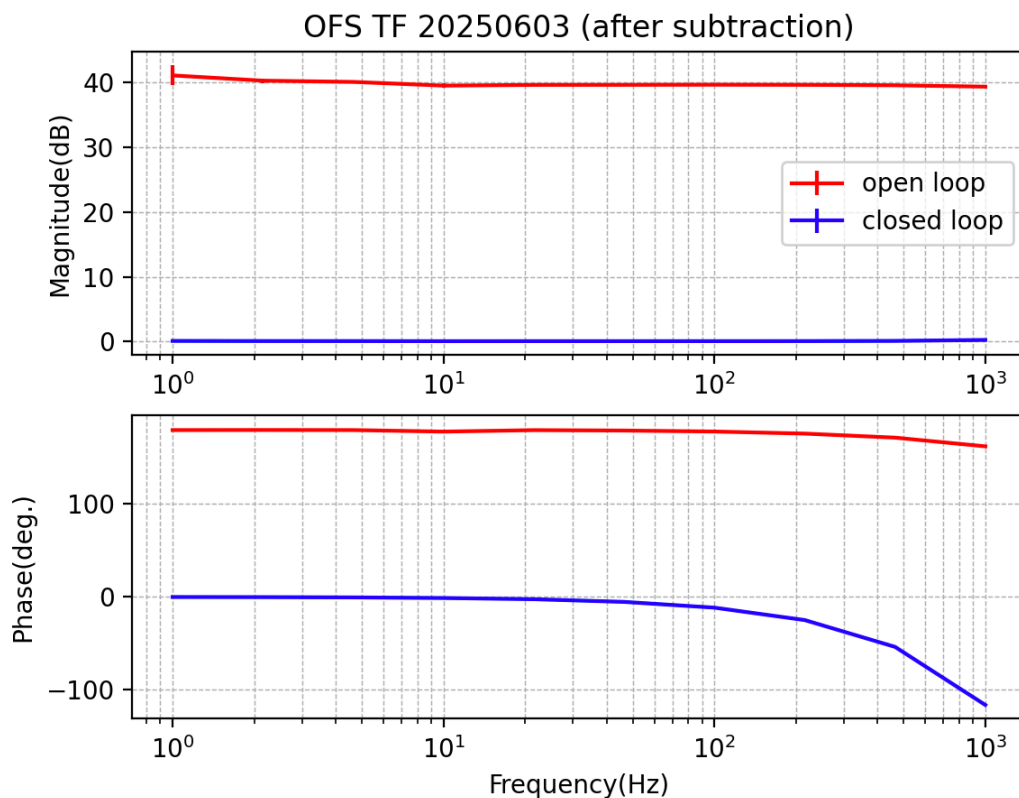


Figure 7.3: Measured transfer function of the intensity stabilization loop. Top: magnitude; Bottom: phase. Red: open-loop; Blue: closed-loop.

7.2.5 Noise Suppression Performance

The measured RIN spectra are shown in Fig. 7.4.

In the open-loop configuration, RIN at low frequencies is approximately $-60 \text{ dB/Hz}^{1/2}$. Closed-loop control achieves 20–30 dB suppression above 10 Hz. The out-of-loop measurement confirms that the achieved suppression is physical and not an artifact of loop gain.

A 20 dB reduction in RIN corresponds directly to a 20 dB reduction in radiation-pressure torque noise. This improvement significantly relaxes the low-frequency angular noise budget and contributes directly to the sub-Hz sensitivity of CHRONOS.

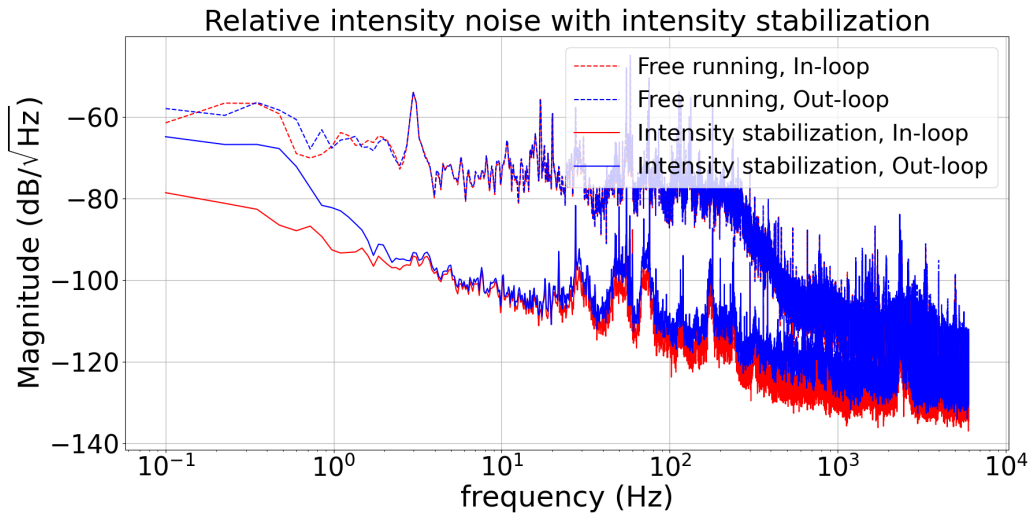


Figure 7.4: Relative intensity noise spectra. Dashed lines: open-loop. Solid lines: closed-loop. Red: OFSPD-in; Blue: OFSPD-out.

7.2.6 Role in Sub-Hz Speed-Meter Operation

In conventional position-meter interferometers, intensity noise primarily affects radiation-pressure force noise. In CHRONOS, however, the torsional degree of freedom enhances the low-frequency response, making RIN coupling particularly severe.

Therefore, the intensity stabilization system is not merely an auxiliary subsystem but a fundamental component of the detector noise architecture. Without sufficient RIN suppression, radiation-pressure torque would dominate the sub-Hz sensitivity band.

The achieved stabilization ensures that laser intensity noise remains below the torsion thermal noise and quantum radiation-pressure noise across the operational frequency range.

7.3 Frequency Stabilization

Laser frequency noise is one of the dominant technical noise sources in interferometric gravitational-wave detectors. A fluctuation in laser frequency $\delta\nu$ is converted into

phase noise through optical path-length asymmetry ΔL as

$$\delta\phi = 2\pi \frac{\delta\nu}{\nu} \Delta L, \quad (7.11)$$

where ν is the laser carrier frequency. Even a small residual asymmetry ΔL can therefore transform frequency noise into measurable phase fluctuations.

In CHRONOS, a torsion-bar speed-meter interferometer operating in the sub-Hz regime, low-frequency phase noise can couple to the rotational degree of freedom through residual optical asymmetries, imperfect common-mode rejection, and control-loop cross couplings. Because the torsional response enhances motion toward low frequencies ($\propto 1/\Omega^2$ above resonance), stringent suppression of frequency noise is required in the sub-Hz band.

Although the Pound–Drever–Hall (PDH) technique is also used to lock the Pre-Mode Cleaner (PMC), its role there is limited to maintaining cavity resonance for spatial filtering. In contrast, the PDH locking to the Reference Cavity (RC) defines the absolute frequency reference of the laser. The frequency stabilization described in this section is therefore fundamentally distinct from the PMC locking scheme.

7.3.1 Reference Cavity as Absolute Frequency Standard

A photograph of the Reference Cavity assembly is shown in Fig. 7.5.

The RC acts as a frequency reference. Locking the laser to the cavity resonance transfers the cavity-length stability to the laser frequency.

The fractional relationship between cavity length and frequency is

$$\frac{\delta\nu}{\nu} = -\frac{\delta L}{L}. \quad (7.12)$$

Therefore, mechanical vibration, acoustic coupling, and thermal expansion of the cavity spacer directly determine the achievable frequency stability.

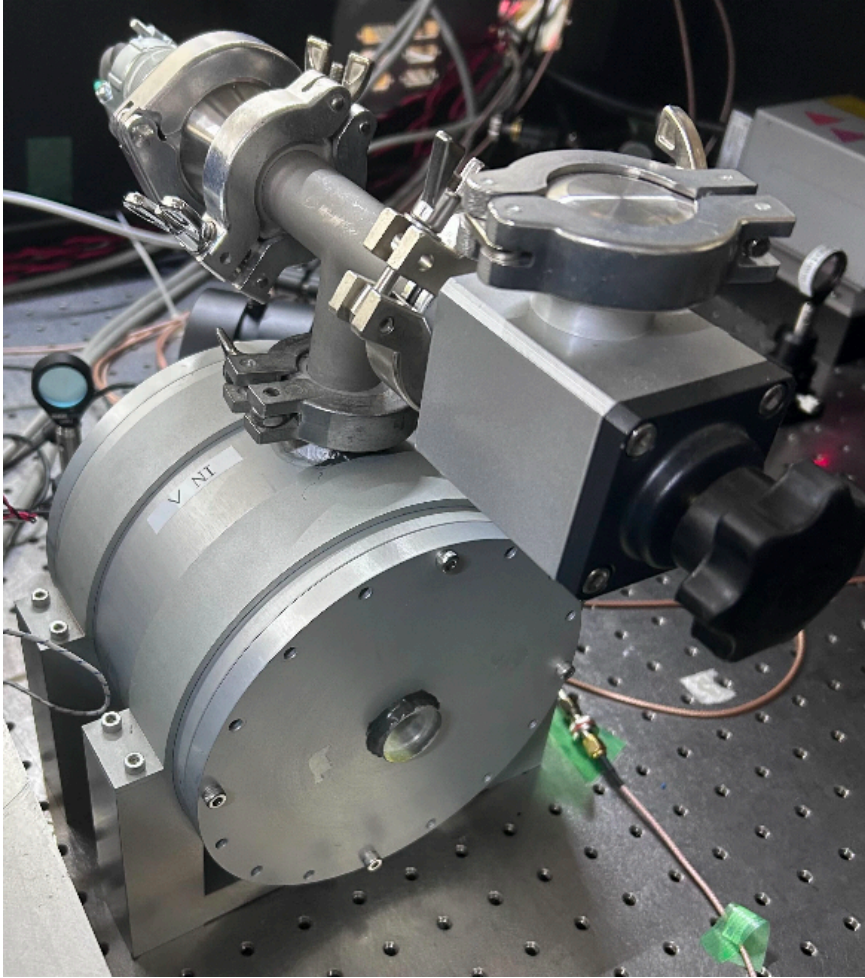


Figure 7.5: Reference Cavity (RC) assembly. A high-finesse optical resonator is enclosed within a cylindrical aluminum housing with thermal stabilization.

Temperature-induced length variations are given by

$$\delta L = \alpha L \delta T, \quad (7.13)$$

where α is the thermal expansion coefficient. Active thermal stabilization reduces long-term drift, while mechanical isolation suppresses vibrational coupling.

The intrinsic linewidth of the cavity, determined by its finesse, sets the frequency discrimination bandwidth. A higher finesse improves sensitivity but reduces capture range, requiring careful optimization between stability and operational robustness.

7.3.2 Multi-Stage Control Hierarchy

Frequency stabilization is implemented using a hierarchical actuator scheme:

- **High bandwidth:** fast phase correction via EOM
- **Intermediate bandwidth:** internal laser PZT actuator
- **Low bandwidth:** laser temperature control

This hierarchy enables broadband noise suppression while maintaining large dynamic range.

The residual closed-loop frequency noise is

$$S_{\nu,\text{closed}}(f) = \frac{S_{\nu,\text{free}}(f)}{1 + G(f)}, \quad (7.14)$$

where $G(f)$ is the open-loop gain. In the regime $|G(f)| \gg 1$, frequency noise is suppressed approximately by $1/G(f)$.

Careful loop design is required to avoid control-noise injection from sensing shot noise or actuator electronics, which may dominate at high frequencies.

7.3.3 Frequency Noise Requirement for CHRONOS

From the CHRONOS sensitivity model, the frequency noise requirement in the sub-Hz band is

$$\delta\nu_{\text{req}} \sim 10^{-2} \text{ Hz}/\sqrt{\text{Hz}}. \quad (7.15)$$

To estimate its impact, frequency noise can be converted into equivalent angular noise through residual optical asymmetry:

$$\theta_{\nu}(\Omega) = \kappa_{\phi} \frac{2\pi}{\nu} \Delta L \delta\nu(\Omega), \quad (7.16)$$

where κ_ϕ represents the phase-to-angle coupling factor. Even small asymmetries ΔL can produce measurable angular fluctuations if frequency noise is insufficiently suppressed.

By locking the laser to the high-finesse RC, the achieved frequency noise level satisfies the above requirement, ensuring that frequency noise remains below torsional thermal noise and quantum radiation-pressure noise across the operational band.

7.3.4 Importance for Sub-Hz Speed-Meter Sensitivity

In conventional position-meter interferometers, frequency noise mainly couples through arm-length mismatch. In CHRONOS, additional coupling pathways arise through rotational sensing asymmetries and control-loop cross couplings.

Because the torsional response enhances low-frequency motion, frequency stabilization must be more stringent than in high-frequency detectors.

Therefore, together with intensity stabilization, frequency stabilization constitutes a core element of the CHRONOS noise architecture. It is not an auxiliary subsystem, but a fundamental prerequisite for achieving quantum-noise-limited sensitivity in the sub-Hz regime.

7.4 Summary of the Input Optics

In this chapter, we have presented the design and implementation of the Input Optics system for CHRONOS. The Input Optics constitutes the pre-stabilization stage that delivers laser light with controlled spatial mode, intensity, and frequency to the main torsion-bar speed-meter interferometer.

First, the Pre-Mode Cleaner (PMC) selects the fundamental TEM₀₀ spatial mode while suppressing higher-order transverse modes and beam-pointing noise. The bow-tie traveling-wave configuration reduces optical back-reflection and scattered-light coupling, providing a stable spatial reference for downstream optical systems. Although

the PMC is locked using the PDH method, its primary role is spatial filtering and preliminary conditioning, rather than defining the absolute laser frequency.

Second, the Intensity Stabilization system employs an Acousto-Optic Modulator (AOM) and an Optical-Follower Servo (OFS) to suppress Relative Intensity Noise (RIN). In-loop and out-of-loop measurements confirm a RIN reduction exceeding 20 dB in the relevant frequency band. Because radiation-pressure torque scales linearly with optical power and the torsional response enhances low-frequency motion, intensity noise directly contributes to angular displacement noise. Therefore, RIN suppression is essential for maintaining sub-Hz sensitivity.

Given that frequency noise couples to phase noise through residual optical asymmetries, and ultimately to angular motion, this level of stabilization is necessary to ensure that frequency noise remains below torsional thermal noise and quantum radiation-pressure noise.

Taken together, the Input Optics system is not merely a beam-conditioning unit, but a core stabilization architecture that directly determines the achievable detector sensitivity. The integrated control of spatial purity, intensity stability, and frequency stability forms the foundation for sub-Hz gravitational-wave detection.

In a torsion-bar speed-meter interferometer, low-frequency technical noise is inherently amplified by the mechanical response of the test mass. Therefore, the stringent laser stabilization described in this chapter is a prerequisite for achieving quantum-noise-limited performance in CHRONOS.

The design and implementation presented here establish the technological basis for stable and high-sensitivity operation in the sub-Hz frequency band.

Output Optics

8.1 Purpose

The Output Optics system forms the final optical stage between the main interferometer and the readout electronics, and is responsible for delivering a spatially clean, phase-controlled, and low-noise signal field to the detection chain. Consequently, the Output Optics is not simply a detection interface, but a carefully designed filtering and readout architecture that preserves the quantum-limited signal while suppressing unwanted optical and technical noise.

One key element of the subsystem is the Output Mode Cleaner (OMC), typically implemented as a compact optical cavity matched to the fundamental eigenmode of the interferometer output field. In contrast to the Input Mode Cleaner, which prepares the beam before it enters the interferometer, the OMC filters the field after it has accumulated imperfections inside the interferometer. Optical aberrations, mirror surface defects, residual misalignments, and scattering processes can all generate higher-order spatial modes at the output port. If left unfiltered, these modes produce excess noise in the detected signal. The OMC transmits the TEM_{00} component that carries the science signal while strongly attenuating higher-order transverse modes and non-resonant optical sidebands.

Both the reflected and transmitted ports of the OMC are utilized for control and monitoring purposes. The reflected beam can be used to generate an error signal for maintaining cavity resonance and alignment, while the transmitted beam serves as the sci-

ence channel input to the balanced homodyne detector. Stable resonance of the OMC is essential, as cavity length fluctuations can directly modulate the transmitted power and introduce excess noise at low frequencies.

Downstream of the OMC, the Balanced Homodyne Detection (BHD) system measures a selected quadrature of the filtered output field. The transmitted beam is interfered with a phase-stable local oscillator on a 50/50 beamsplitter, and the differential photocurrent from two photodiodes provides a low-noise readout of the interferometer signal. This approach enables flexible selection of the readout quadrature and improved rejection of common-mode intensity noise compared to direct detection.

The OMC and BHD assemblies are designed with high mechanical rigidity, low optical loss, and careful stray-light control to meet the stringent low-frequency noise requirements of CHRONOS. Provision is also made for thermal stabilization and potential future suspension upgrades, aimed at further reducing cavity-length and alignment fluctuations in the sub-Hz regime.

Therefore, the CHRONOS Output Optics system operates as a spatial filtering and precision readout architecture. By suppressing higher-order spatial modes, stabilizing the output field, and enabling low-noise quadrature measurement through balanced homodyne detection, it ensures that the detected signal faithfully represents the interferometer response required for sub-Hz gravitational-wave measurements.

8.2 Output Mode Cleaner

8.2.1 Principle

The transverse profile of a laser beam can be expanded in terms of Gaussian spatial modes, specifically the Hermite-Gaussian modes. For CHRONOS, the desired spatial distribution is the fundamental transverse electromagnetic mode, TEM_{00} . However, real optical components are never perfect, and surface roughness errors, coating irregularities, or slight angular misalignments of mirrors can redistribute optical power from the fundamental mode into higher-order transverse modes.

To mitigate this, an input mode cleaner is installed upstream of the main interferometer as described in previous chapters. Its role is to filter the incoming beam so that predominantly the TEM_{00} mode is injected. Even with a well-prepared input beam, imperfections and misalignment within the main interferometer can still generate additional higher-order modes. For this reason, an output mode cleaner (OMC) is positioned downstream of the main interferometer, at the detection port. The OMC selectively transmits the fundamental mode, which carries the gravitational-wave signal, while rejecting higher-order modes generated within the interferometer itself.

8.2.2 Higher Order Mode Suppression

The OMC is a resonant cavity matched to the fundamental spatial mode of the interferometer output. Higher-order transverse modes experience a different round trip Gouy phase and are therefore detuned from resonance with respect to the cavity. As a result, their transmission is strongly suppressed compared to the TEM_{00} mode. In addition to spatial filtering, the cavity linewidth also provides a degree of frequency filtering, attenuating residual radio-frequency control sidebands that are not resonant with the cavity. The OMC power transmittance of the m^{th} spatial mode and the RF sideband is given, respectively, by [68]:

$$T_{OMC} = \frac{(1 - r_1^2 - \mathcal{L})(1 - r_3^2 - \mathcal{L})r_2^2 r_4^2}{|1 - r_1 r_2 r_3 r_4 e^{-im\eta}|^2} \quad (8.1)$$

$$T_{RF} = \frac{(1 - r_1^2 - \mathcal{L})(1 - r_3^2 - \mathcal{L})r_2^2 r_4^2}{|1 - r_1 r_2 r_3 r_4 e^{-im\eta + 2iL\omega_{RF}/c}|^2} \quad (8.2)$$

where T_{OMC} and T_{RF} are the OMC power transmittance of the higher order modes and RF sideband, respectively; r_i is the reflectivity of the i^{th} OMC mirror, \mathcal{L} is the optical loss per bounce, m is the mode order, and η is the round trip Gouy phase.

For CHRONOS, suppression of higher-order modes is particularly important because the low-frequency signal band is susceptible to excess noise coupling through wavefront distortions, and scattered light. The OMC reduces this coupling pathway and stabilizes the downstream homodyne readout.

8.2.3 Optical Design

The OMC is implemented as a compact optical cavity placed after the interferometer output port, with its specifications for cavity length, mirror reflectivities and radii of curvature chosen to balance mode selectivity and optical losses. The cavity length is inversely related to the free spectral range, or the spacing between adjacent modes, and must be appropriately chosen to transmit only the desired fundamental mode[44]. At the same time, the finesse, which is related to the sharpness of the resonance peak, must be high enough to discriminate against higher-order spatial modes but low enough such that intra-cavity optical losses do not significantly degrade the signal-to-noise ratio.

Mode matching between the interferometer output beam and the OMC eigenmode is a critical design consideration. Imperfect mode matching leads to direct signal loss, as part of the fundamental mode is rejected together with the higher-order content. For this reason, dedicated mode-matching optics are included upstream of the OMC to adapt the beam waist and curvature.

The incidence angle or the geometry of the bow-tie cavity also has a tradeoff, wherein it must be large enough to reduce backscattering but small enough to reduce mode ellipticity[44].

Mechanical stability of the OMC assembly is another key factor, especially in a cryogenic and low-frequency instrument such as CHRONOS. Length and alignment fluctuations of the cavity can convert into amplitude noise at the transmission port. The cavity is therefore designed to be rigidly mounted, with actuators for fine alignment control and length tuning to maintain resonance with the carrier field.

Fig. 8.1 shows the layout of the output mode cleaner (OMC), consisting of mode-matching and alignment optics followed by a bow-tie cavity with two low-reflectivity mirrors and two high-reflectivity mirrors (HRMs). A pick-off beam taken before the OMC is used for cavity control. The transmitted, spatially filtered light carrying the GW signal is then sent to the balanced homodyne detection (BHD) readout.

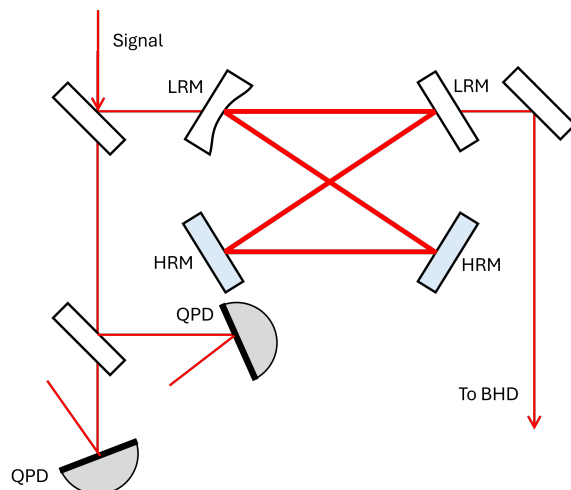


Figure 8.1: Schematic diagram of output mode cleaner(OMC) composed of mode-matching and alignment optics, followed by the bow-tie cavity with two low-reflectivity mirrors (LRM) and two high-reflectivity mirrors (HRM). A portion of the laser prior to the OMC will be directed to the OMC for control purposes. The spatially filtered transmitted light, which contains the GW-modulated signal, then proceeds to the BHD readout.

8.2.4 Future Upgrade

In the current configuration, the OMC will be implemented in a fixed aluminum cavity, primarily to validate the optical layout and control scheme. While this approach simplifies integration and commissioning, it also leaves the cavity more exposed to seismic and acoustic disturbances, which can modulate the cavity length and alignment. For a full-scale implementation, a dedicated suspension system is envisioned to provide additional isolation from environmental noise, and the OMC will be constructed on a fused silica breadboard, with components fixed via epoxy.

A suspended OMC would benefit from reduced coupling of ground motion and mechanical vibrations, particularly in the sub-Hz regime relevant for CHRONOS. By designing the suspension to have low resonant frequencies and adequate damping, it is possible to suppress length fluctuations of the cavity and maintain stable resonance conditions. In addition, using a fused silica breadboard minimizes thermal noise.

8.3 Balanced Homodyne Detection

8.3.1 Principle

Achieving further noise suppression in gravitational-wave detectors while maintaining a relatively compact detector size necessitates the use of non-classical optical fields, particularly squeezed states, where the uncertainty in one quadrature is reduced at the expense of increased noise in the conjugate quadrature[26]. Since future detector schemes may rely on a flexible readout of the quadrature space of the output light field, balanced homodyne detection is expected to replace the currently used DC readout[101]. Balanced homodyne detection enables the measurement of any chosen quadrature by interfering a weak signal beam with a strong local oscillator. When implemented in interferometric setups, this approach allows high-precision readout that fully exploits the advantages of squeezed light. Because such quantum states play a central role in modern gravitational-wave instrumentation, it has already been demonstrated in a full scale michelson interferometer setup [2] and ongoing research is being done in this field [99, 53, 107]. Accordingly, this project focuses on developing the optical hardware and readout electronics required for a balanced homodyne detector suitable for use in cross torsion bar detection experiments involving non-classical light.

Balanced homodyne detection is employed to measure the field quadrature that carries the signal with high quantum efficiency and low technical noise. In this scheme, the signal beam transmitted by the OMC is interfered with a strong, phase-stable local oscillator (LO) on a 50/50 beamsplitter. The two output ports are detected by a pair of matched photodiodes, and their photocurrents are subtracted to suppress common-mode intensity noise and obtain the differential signal, the BHD readout.

8.3.2 Readout Angle

A key feature of homodyne detection is the ability to tune the readout quadrature by adjusting the relative phase or homodyne angle between the local oscillator and the

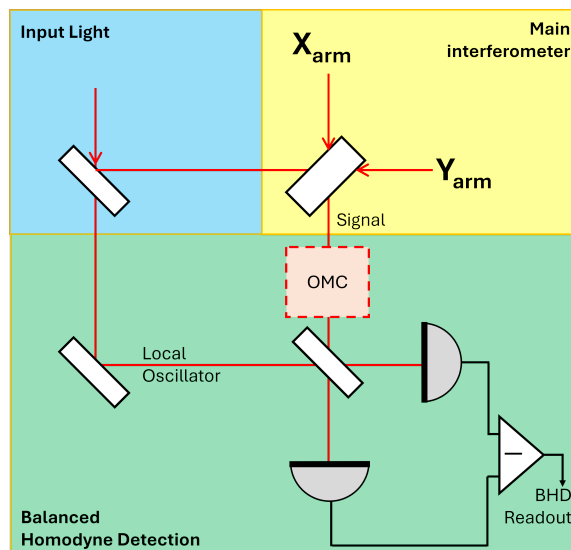


Figure 8.2: Schematic diagram of balanced homodyne detection(BHD) readout scheme with simplified layouts of the other CHRONOS subsystems to show the overall setup.

signal beam. In the context of CHRONOS, the optimal readout angle depends on the interferometer operating point and the frequency-dependent noise budget.

Careful control of the homodyne angle is therefore required to maintain optimal sensitivity across the measurement band. Stable control of this phase is essential, as fluctuations in the readout angle can lead to mixing of unwanted noise quadratures into the detected signal.

8.3.3 Optical Design

The optical layout of the BHD system is shown in Fig. 8.2. The local oscillator is derived from a clean reference beam picked-off before the main interferometer, and routed to the homodyne beamsplitter with carefully controlled path length. The local oscillator and signal beam from the OMC is then mixed at the homodyne beamsplitter, and the two output ports are measured using photodiodes. The photocurrents are then subtracted to obtain the differential signal.

Particular attention is given to balancing optical power and path length on the two photodiodes, as any imbalance reduces the effectiveness of common-mode noise cancellation.

8.3.4 Future Upgrade

The use of squeezed states of light at the output port offers a method to reduce quantum noise in the CHRONOS readout. In particular, frequency-dependent squeezing could be employed to simultaneously suppress shot noise at higher frequencies and radiation-pressure noise at lower frequencies [66]. Implementing such a scheme would require an additional filter cavity to rotate the squeezing angle as a function of frequency before injection into the homodyne detector.

Although not part of the baseline design, the output optics layout may be designed with sufficient flexibility to accommodate future integration of squeezed light sources and associated filter cavities. This forward-compatible approach ensures that upgrades aimed at quantum noise reduction can be incorporated without major redesign of the detection setup.

Cryogenic System

The sensitivity of gravitational-wave detectors is fundamentally limited by a combination of intrinsic and environmental noise sources. Continuous advancements in interferometry, optical design, suspension systems, and control techniques have led to a variety of proposed upgrades aimed at improving detector sensitivity [9, 1]. Among these noise sources, thermal noise arising from Brownian motion remains one of the dominant limitations, particularly in the low-frequency regime [91, 71, 51].

A direct and effective approach to reducing thermal noise is cryogenic operation. Lowering the temperature suppresses thermally driven fluctuations associated with mechanical dissipation, in accordance with the fluctuation–dissipation theorem [22], thereby improving the fundamental sensitivity of the detector. For this reason, next-generation and future gravitational-wave detectors, such as *LIGO Voyager* [10], *KAGRA* [12], and the *Einstein Telescope* [84], incorporate cryogenic operation as a key design element. However, systems that have been optimized for room-temperature operation must be carefully re-evaluated under cryogenic conditions. Material properties, mechanical response, optical performance, and control behavior all exhibit temperature dependence [118, 100], requiring comprehensive validation in a low-temperature environment.

In addition to reducing thermal noise in the test mass, cryogenic operation significantly affects the mechanical loss of optical coatings. Since coating dissipation is strongly temperature-dependent, operating at an appropriate cryogenic temperature can lead to substantial improvements in detector sensitivity [118, 100]. Thus, cryogenic technology plays a crucial role not only in thermal noise reduction but also in

enabling improved material performance.

On the other hand, the introduction of a cryogenic system introduces new technical challenges. Mechanical vibrations originating from cryocoolers, as well as structural resonances of the cryostat, can couple to the test mass and degrade detector sensitivity [12]. Therefore, minimizing vibration transmission is essential in cryogenic interferometers. While passive isolation techniques have been widely employed, they are often insufficient in the low-frequency band.

For future high-sensitivity detectors operating in the sub-Hz regime, it is necessary to integrate advanced vibration mitigation strategies with thermal design. In this study, we present the design concept of the cryogenic system for CHRONOS, focusing on achieving both thermal noise reduction and effective vibration suppression.

9.1 Cryocooler and Heat Link

To realize cryogenic operation for thermal noise reduction, we developed a dedicated cryogenic system for CHRONOS. As shown in Fig. 9.1, the system consists of a cryogenic chamber coupled to the main interferometer chamber, enabling cooling of the suspension system and the test mass.

Inside the chamber, a two-stage pulse-tube cryocooler (PTC) with nominal 50 K and 4 K stages is installed. Pulse-tube cryocoolers are widely used in low-vibration cryogenic applications because they contain no moving parts at the cold head, significantly reducing vibration transmission compared to conventional Gifford–McMahon (GM) cryocoolers [117, 12]. The radiation shields at 300 K and 50 K suppress radiative heat transfer from higher-temperature components, allowing efficient cooling of the inner stages.

Cooling is provided by a commercial two-stage pulse-tube cryocooler (Sumitomo Heavy Industries, SRP-082B2-F70LP), which provides cooling capacities at approximately 50 K (first stage) and 4 K (second stage). Such cryogenic architectures are also adopted in KAGRA for low-vibration mirror cooling [12].

The cold heads are thermally connected to each temperature stage via heat links, while

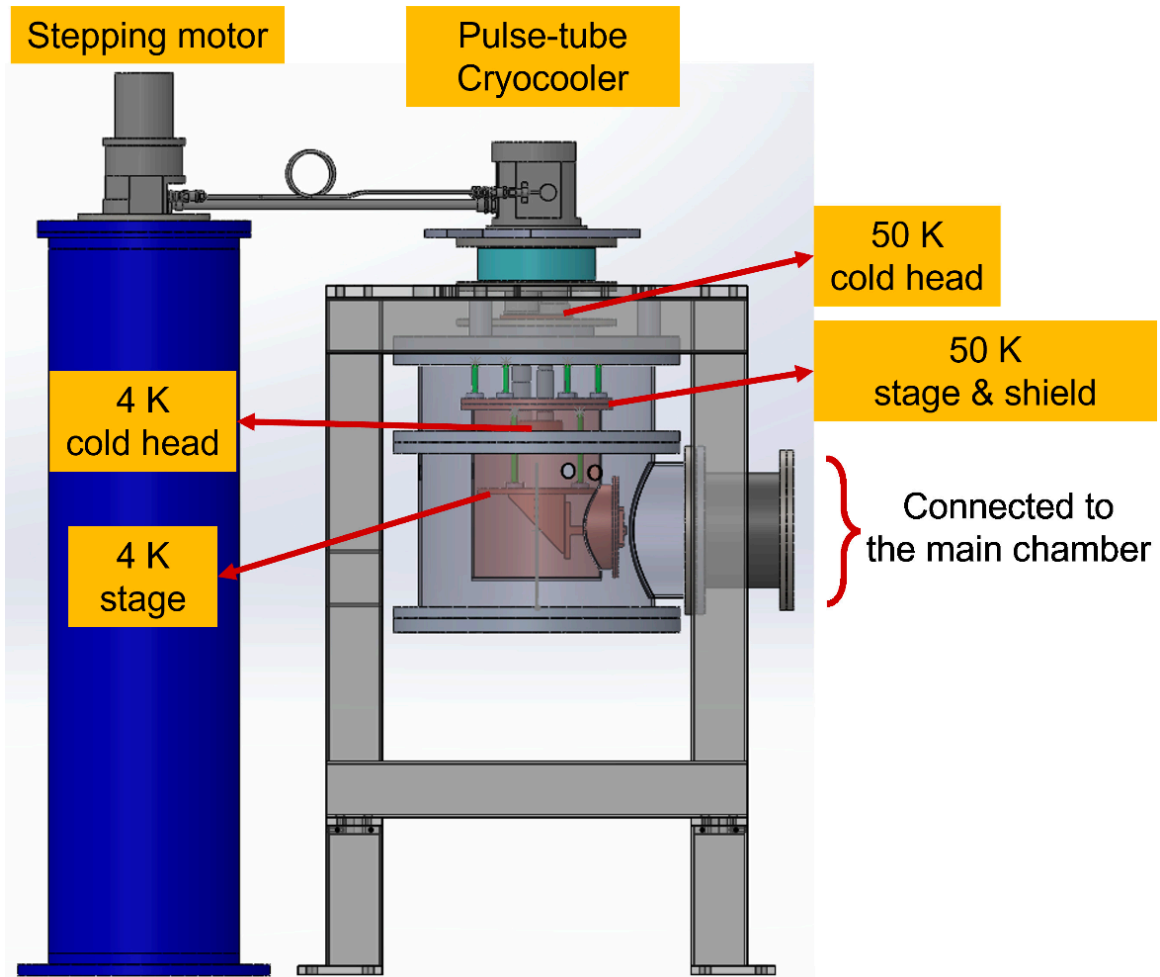


Figure 9.1: Overall configuration of the cryogenic chamber. The system consists of a two-stage pulse-tube cryocooler, 50 K and 4 K stages, and radiation shields at 300 K and 50 K. The multi-stage shielding structure suppresses radiative heat inflow from warm components.

mechanical isolation is maintained through low-conductivity supports. As shown in Fig. 9.3, the 50 K stage is suspended from the 300 K structure using low-thermal-conductivity polyimide (Vespel®) tubes. Similarly, the 4 K stage is supported from the 50 K stage using identical structures. This configuration minimizes parasitic heat conduction while maintaining mechanical stability. To suppress residual gas conduction, vent holes are introduced in the mounting screws to evacuate trapped gas inside the support tubes.

The heat links play a crucial role in achieving both efficient cooling and vibration isolation. Mechanical vibrations generated inside the cryocooler, such as pressure oscillations of the working gas, can propagate through rigid thermal connections and couple to the test mass [117]. To suppress this effect, we adopt flexible heat links composed of bundles of thin wires rather than a single rigid conductor. For the same cross-sectional area, such a stranded structure provides significantly lower stiffness, thereby reducing vibration transmission while maintaining high thermal conductivity. High-purity copper is used for the 50 K stage, while high-purity aluminum (99.9999%, 6N) is used for the 4 K stage, taking advantage of their excellent cryogenic thermal conductivity [83].

To further reduce radiative heat transfer, multi-layer insulation (MLI) is applied to both stages. MLI consists of multiple reflective layers and is highly effective in suppressing radiation, which dominates heat transfer in vacuum environments [83]. In this system, approximately 50 layers are applied to the 50 K stage and 30 layers to the 4 K stage, significantly reducing radiative heat load and improving cooling efficiency.

In summary, the cryogenic system is designed to simultaneously achieve low temperature and low vibration by combining: (i) multi-stage radiation shielding, (ii) low thermal-conductivity supports to suppress parasitic heat flow, and (iii) low-stiffness heat links for vibration isolation.

In addition to passive isolation, further reduction of residual vibration from the pulse-tube cryocooler is pursued using active vibration isolation (AVI). In an active scheme, vibrations are measured using sensors and suppressed by applying counteracting forces through actuators. Such feedback-based vibration suppression techniques are widely employed in precision interferometry [1, 12]. This approach is particularly important

for periodic low-frequency vibrations originating from the cryocooler, where passive isolation alone is insufficient.

The design and performance of the active vibration isolation system are described in detail in the following section.



Figure 9.2: Two-stage pulse-tube cryocooler used in this system. The first stage cools to ~ 50 K and the second stage to ~ 4 K. The absence of moving parts at the cold head provides low-vibration operation suitable for precision interferometry.

9.2 Cryogenic Performance

We evaluated the cryogenic performance of the system, with particular emphasis on quantifying heat loads arising from thermal conduction and radiation. To this end, controlled heat inputs were applied to the 4 K and 50 K stages, and the corresponding temperature responses were measured. This evaluation is essential for validating the thermal design and assessing the cooling margin under cryogenic operation [83].

During the measurements, the cold heads were thermally decoupled from each stage to isolate the intrinsic cooling performance of the cryocooler. This configuration allows direct evaluation of the response to externally applied heat loads. Ceramic heaters were mounted on each stage, and the injected power was precisely determined using

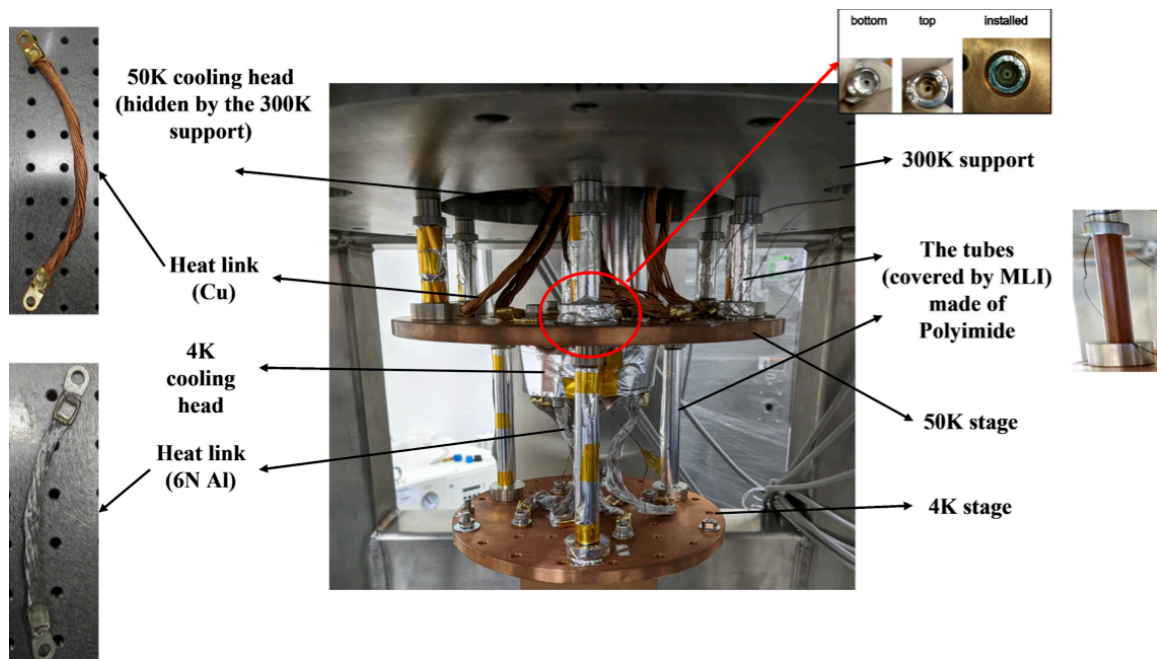


Figure 9.3: Structure of the cold heads and thermal stages. Low-conductivity Vespel supports reduce parasitic heat flow, while heat links provide efficient thermal coupling. This design balances thermal isolation and mechanical stability.

four-wire measurements of voltage and current. By varying the applied voltage, heat loads in the range of approximately 0–25 W for the 50 K stage and 0–2 W for the 4 K stage were introduced.

Figure 9.4 shows the relationship between the applied heater power and the steady-state temperature of each stage. From the slope of these curves, the effective thermal conductance and radiative heat load were evaluated. The heat balance can be expressed as

$$Q_{\text{in}} = Q_{\text{cond}} + Q_{\text{rad}} + Q_{\text{cool}}, \quad (9.1)$$

where conductive heat flow follows Fourier's law and radiative heat load follows the Stefan–Boltzmann relation [83].

The measured effective parasitic heat loads at 4.2 K and 30 K are approximately 0.5 W and 5 W, respectively. These values are consistent with theoretical estimates based on the number of MLI layers, the thermal conductivity of the support structures, and the heat-link design. They are also comparable to typical performance levels of cryogenic systems of similar scale, such as those implemented in KAGRA [12].

To characterize the cooling dynamics, we measured the cooldown process from room temperature to operating temperature. Silicon diode thermometers were used to monitor the temperature evolution of the cold heads and each stage simultaneously. The temporal temperature response is shown in Fig. 9.5. The system reaches operating temperatures of 4 K and 50 K in approximately 1000 minutes (about 17 hours), which is consistent with the expected thermal mass and cooling power of the cryocooler.

Temperature measurements were performed using calibrated silicon diode sensors (DT-680B-CU, Lake Shore Cryogenics), whose temperature dependence is well characterized in the cryogenic range [70]. Four sensors were installed: one on each of the 4 K and 50 K cold heads, and one on each of the corresponding stages. This configuration enables quantitative evaluation of the temperature gradient between the cold heads and stages, providing insight into thermal resistance and heat-transfer efficiency.

These results demonstrate that the cryogenic system achieves the designed cooling performance and provides sufficient thermal conditions for realizing a low thermal-noise environment in CHRONOS.

9.2.1 Active Vibration Isolation System

One of the major challenges in cryogenic systems is periodic mechanical vibration originating from the cryocooler and compressor. Although PTC exhibit lower vibration compared to conventional cryocoolers, residual pressure oscillations and gas flow inside the system generate periodic disturbances, particularly in the low-frequency band [117, 12]. These vibrations can propagate through heat links and support structures and couple to the test mass, potentially limiting the detector sensitivity.

As discussed in the previous section, passive isolation methods such as bellows and low-stiffness heat links are effective at higher frequencies, but their performance degrades in the low-frequency regime [1]. For CHRONOS, which targets high sensitivity in the sub-Hz band, active vibration suppression is therefore essential.

To address this issue, we developed an active vibration isolation system (AVIS). A schematic overview of the system is shown in Fig. 9.6.

The AVIS directly controls the relative motion between the cryocooler and the ground

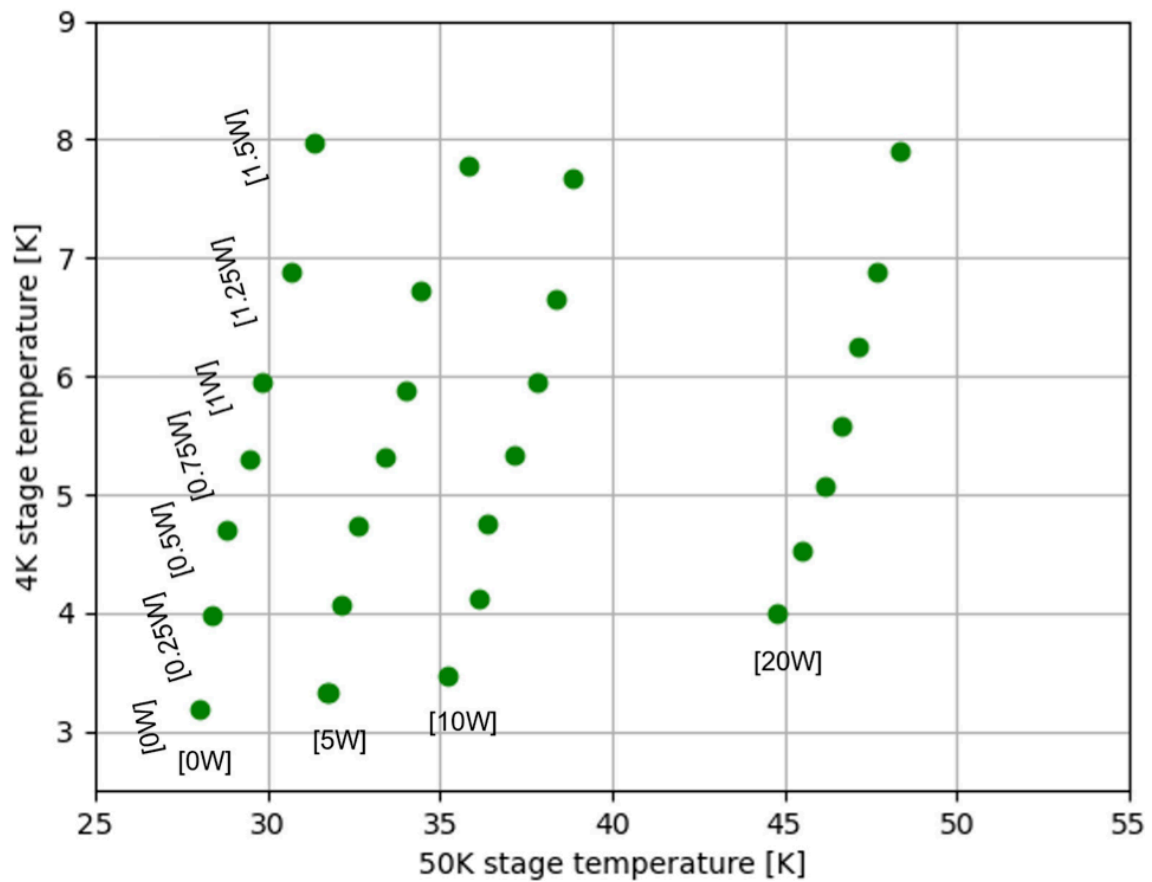


Figure 9.4: Thermal loading map of the 4 K and 50 K stages. The horizontal axis shows the applied heater power, and the vertical axis shows the steady-state temperature. The slope of each curve provides a measure of the effective thermal conductance and radiative heat load. A stable thermal response is observed over the full range of applied power.

support structure. The pulse-tube cryocooler is mounted to the 300 K chamber lid via bellows, which provide passive vibration isolation. In addition, six piezoelectric actuators (PZTs) are installed to actively control the relative displacement between the cryocooler and the support structure.

The system operates based on feedback control theory. The static equilibrium position of the cryocooler is defined as the operating point. Sensor signals measuring displacement and acceleration are continuously monitored, and the actuators generate counteracting displacements with opposite phase, thereby canceling vibration components. This approach is particularly effective for suppressing periodic disturbances

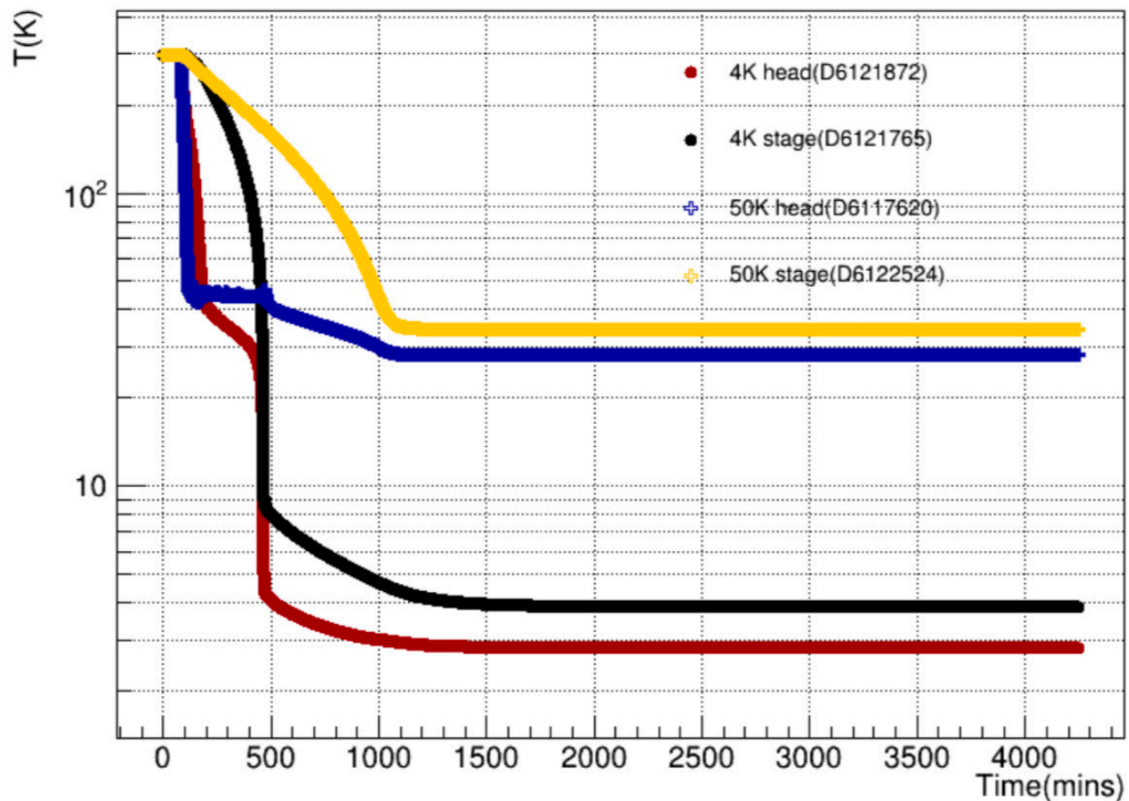


Figure 9.5: Temperature evolution during the cooldown process. The 50 K stage cools first, followed by the 4 K stage. The system reaches operating temperatures in approximately 1000 minutes (17 hours), indicating efficient thermal design of the cryostat and heat-link system.

originating from the cryocooler.

The system is designed to control six degrees of freedom (6-DOF), consisting of three translational motions (x , y , z) and three rotational motions (roll, pitch, and yaw). By appropriately arranging sensors and actuators, simultaneous control of all degrees of freedom is achieved, similar to multi-axis active isolation platforms used in advanced interferometers [1].

A photograph of the installed cryogenic system is shown in Fig. 9.7. The cryocooler is located inside the cryogenic chamber, while the compressor and drive units are installed externally. The AVIS is positioned between the cryocooler and the ground support structure, actively suppressing vibrations originating from the cryogenic system.

Figure 9.8 shows the detailed configuration of the AVIS. Multiple rigid stages are at-

tached above the cryocooler to mount the sensors. Accelerometers are installed on the outer top stage, while reflective targets for the photosensors are mounted on a windmill-shaped plate. This configuration allows simultaneous detection of horizontal and vertical vibrations.

The six piezoelectric actuators are arranged between the top plate and the outer stage, enabling force application in all degrees of freedom. This configuration realizes real-time feedback control of the full 6-DOF motion.

In this section, we have described the overall architecture and operating principle of the AVIS. The detailed specifications and performance of the sensors and actuators are presented in the following section.

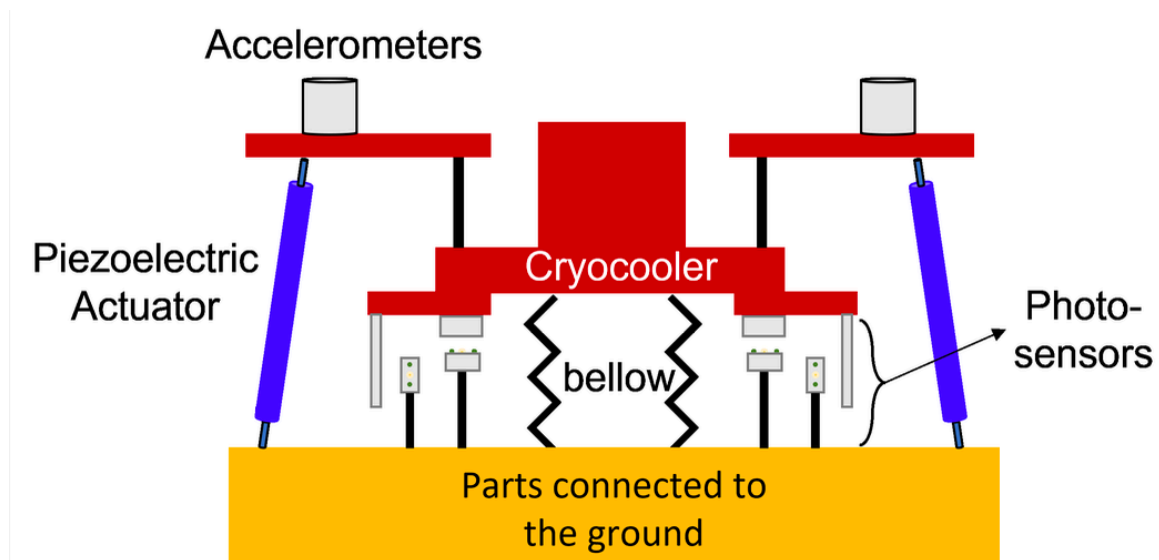


Figure 9.6: Schematic of the AVIS. The yellow structure is fixed to the ground and serves as a reference frame, while the red structure is connected to the cryocooler. They are coupled via bellows and piezoelectric actuators, allowing active control of relative motion. Multiple sensors (accelerometers and photosensors) enable six-degree-of-freedom control.

9.2.2 Photosensors

To monitor the relative displacement between the cryocooler and the ground support structure, non-contact photosensors are employed in this system. Since the measure-

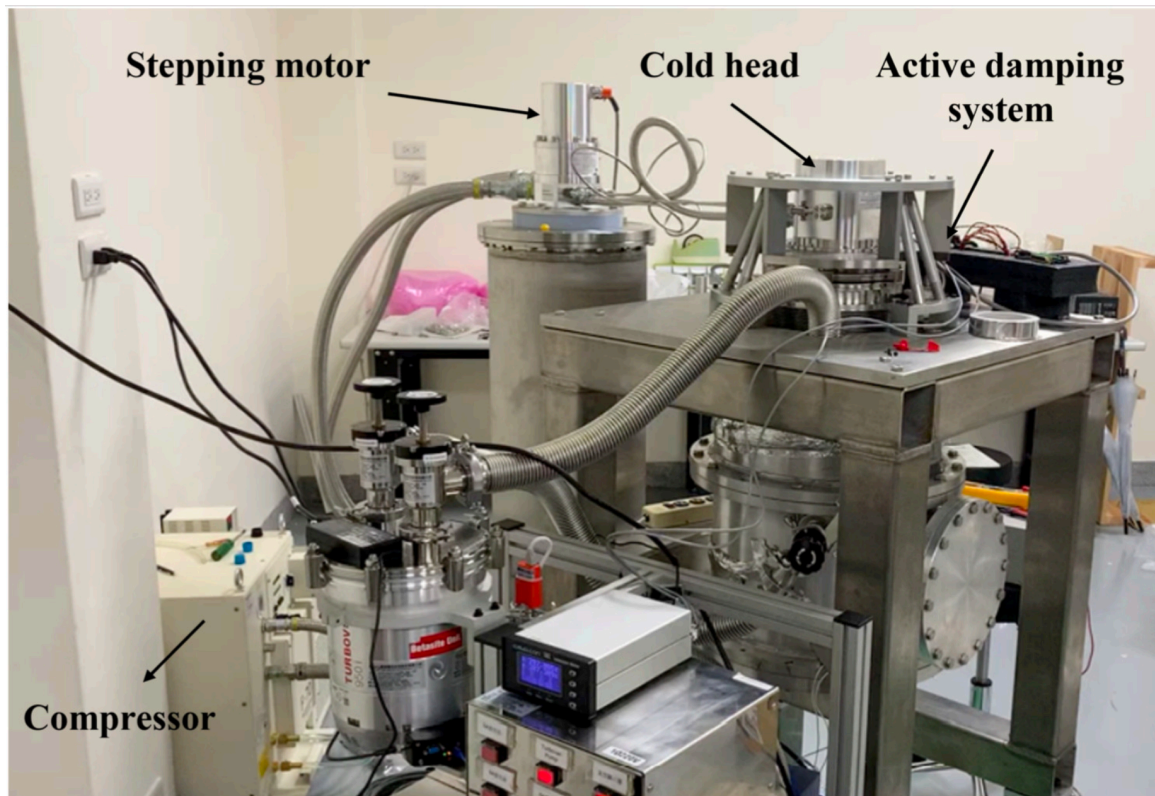


Figure 9.7: Photograph of the cryogenic system. The pulse-tube cryocooler is installed inside the chamber, and the AVIS is placed between the cryocooler and the ground support structure.

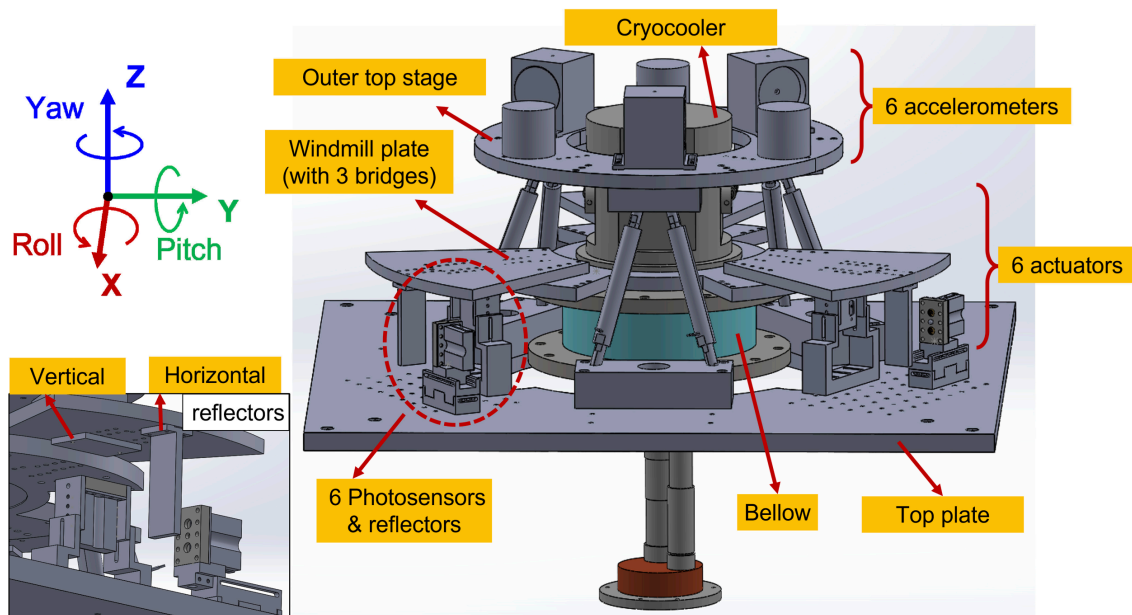


Figure 9.8: Integrated setup of the AVIS. Accelerometers (for high-frequency components) and photosensors (for low-frequency components) measure vibrations, while six piezoelectric actuators generate compensating motion. Simultaneous control of all six degrees of freedom is achieved.

ment is performed optically, the sensors introduce no mechanical loading on the system, making them particularly suitable for detecting small displacements in the low-frequency regime [1].

As shown in Fig. 9.9, the photosensor is a reflective optical device consisting of one LED and two photodiodes (PDs). Light emitted from the LED is reflected by a target mirror and detected by the PDs. The relative displacement between the sensor and the target is inferred from the change in the reflected light intensity, following standard optical position-sensing principles [55].

The photosensors provide a wide dynamic range and are effective for monitoring slow drifts and low-frequency vibrations. In this system, three horizontal and three vertical sensors are arranged to reconstruct the 6-DOF motion of the cryocooler, similar to multi-axis sensing schemes used in active isolation platforms as shown in Fig. 9.10 [1].

Detailed characterization of the sensor performance, including operation under cryogenic conditions, is under ongoing study.

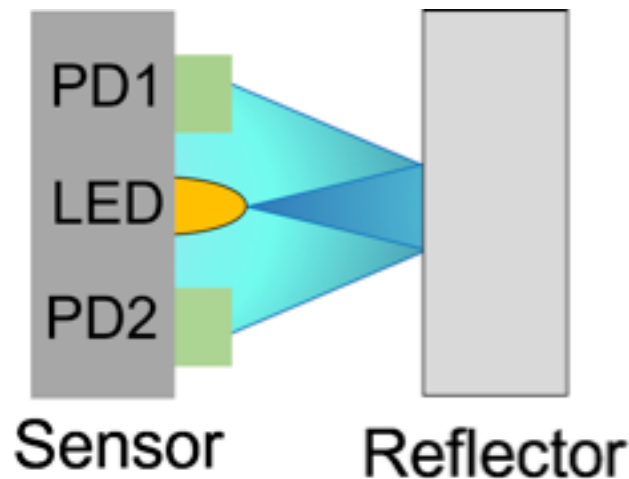


Figure 9.9: Schematic of the photosensor. Light emitted from the LED is reflected by a target and detected by photodiodes. Displacement is measured from the change in reflected light intensity.

9.2.3 Piezoelectric Actuators

Active vibration compensation is achieved using PZTs. Piezoelectric elements convert applied voltage into mechanical displacement, providing fast response and high resolution suitable for precision control [108].

The AVIS consists of six supporting legs, each equipped with one PZT. As shown in Fig. 9.11, the actuators are arranged with an inclination angle of approximately 15° , allowing control of three translational and three rotational degrees of freedom. Such geometric arrangements enable full 6-DOF control through appropriate transformation between actuator space and Cartesian coordinates.

The actuators are installed between the top plate and the support structure, and apply forces to compensate for the relative displacement between the cryocooler and the ground. Control signals are generated by a digital control system and independently applied to each actuator, enabling flexible multi-degree-of-freedom control.

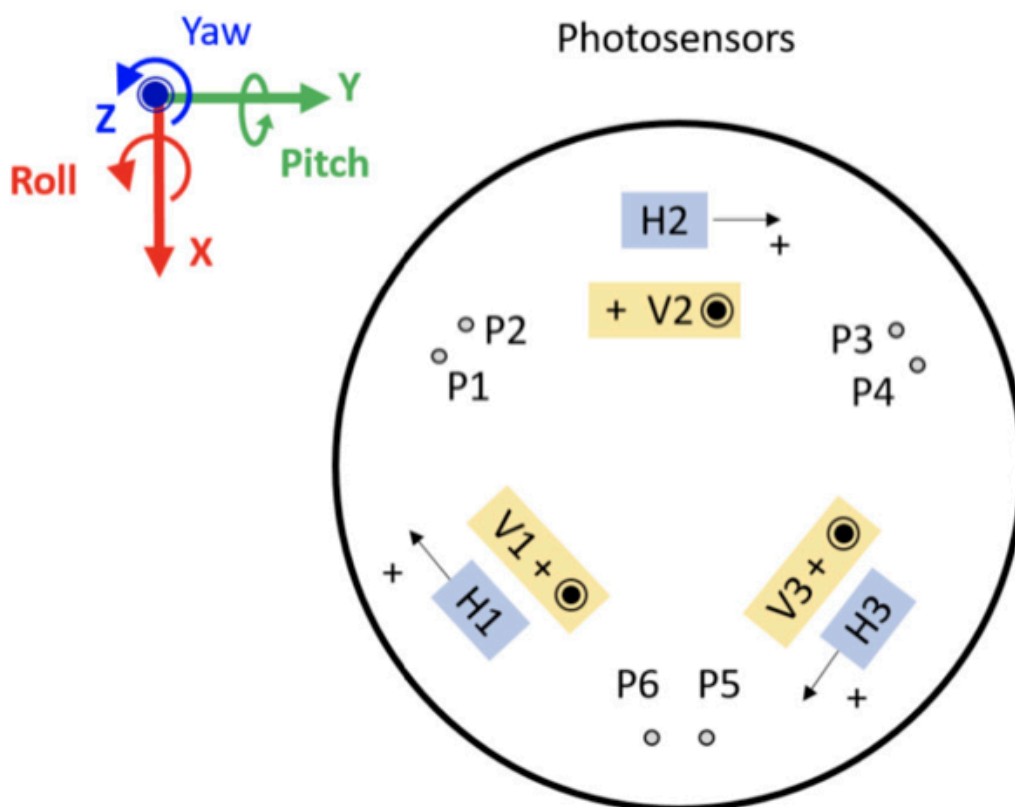


Figure 9.10: Configuration of the photosensors and coordinate system. Three horizontal and three vertical sensors are used to reconstruct 6-DOF motion.

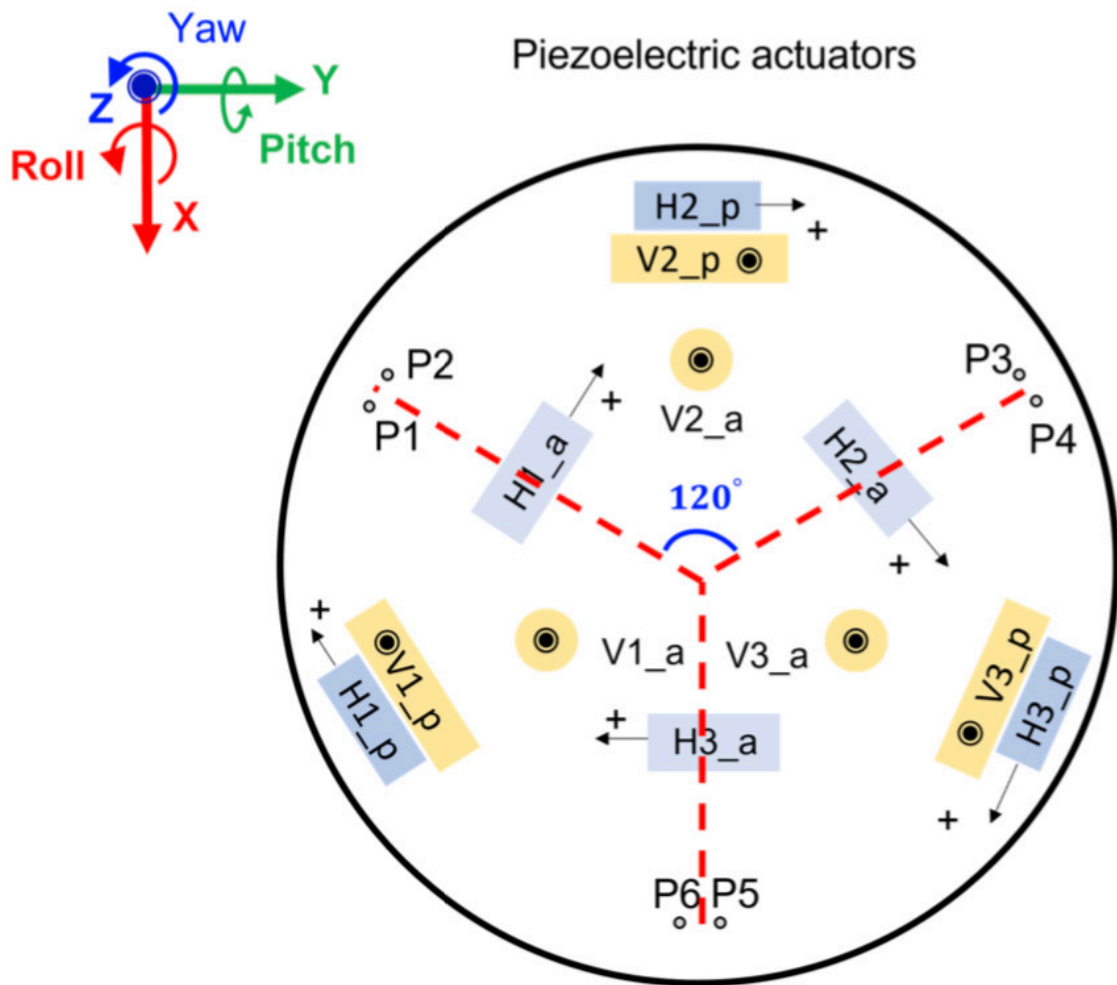


Figure 9.11: Arrangement of the piezoelectric actuators. Six PZTs are symmetrically placed, enabling control of all six degrees of freedom.

9.2.4 Control and Transfer Function

The control performance of the AVIS is characterized through measurements of the open-loop transfer function. A swept excitation signal is injected into the control system, and the system response is analyzed to obtain the frequency response.

The loop dynamics can be described by the standard feedback relation

$$T(\Omega) = \frac{G(\Omega)P(\Omega)}{1 + G(\Omega)P(\Omega)}, \quad (9.2)$$

where $P(\Omega)$ is the plant transfer function and $G(\Omega)$ is the controller transfer function [41].

Based on the measured Bode plots, digital filters are designed to compensate for phase delay and stabilize the feedback loop. A representative transfer function is shown in Fig. 9.12.

The unity gain frequency (UGF) is approximately 0.5 Hz, indicating that the feedback control is effective in the sub-Hz to 0.5 Hz range. A phase margin of about 55° ensures stable operation of the control system, consistent with standard stability criteria [41].

These results demonstrate that the AVIS provides sufficient control bandwidth to suppress low-frequency vibrations originating from the cryocooler.

9.2.5 Noise Performance

The vibration suppression performance of the AVIS was evaluated by comparing noise spectra before and after feedback control.

Initially, each degree of freedom was controlled independently, confirming that noise reduction is achieved in the frequency range below 1 Hz. Subsequently, the number of controlled degrees of freedom was gradually increased, leading to full 6-DOF simultaneous feedback control.

The system stability during multi-degree-of-freedom operation was verified through transfer function measurements, confirming stable control across all degrees of freedom.

Figure 9.13 shows the measured noise spectra before and after feedback control. Significant noise reduction is observed in the low-frequency region below 1 Hz, with improvements seen in all degrees of freedom. In particular, a pronounced reduction is observed in the y direction.

These results demonstrate that the AVIS effectively suppresses cryocooler-induced vibrations over a broad frequency range, and is particularly effective in the low-frequency band relevant for CHRONOS.

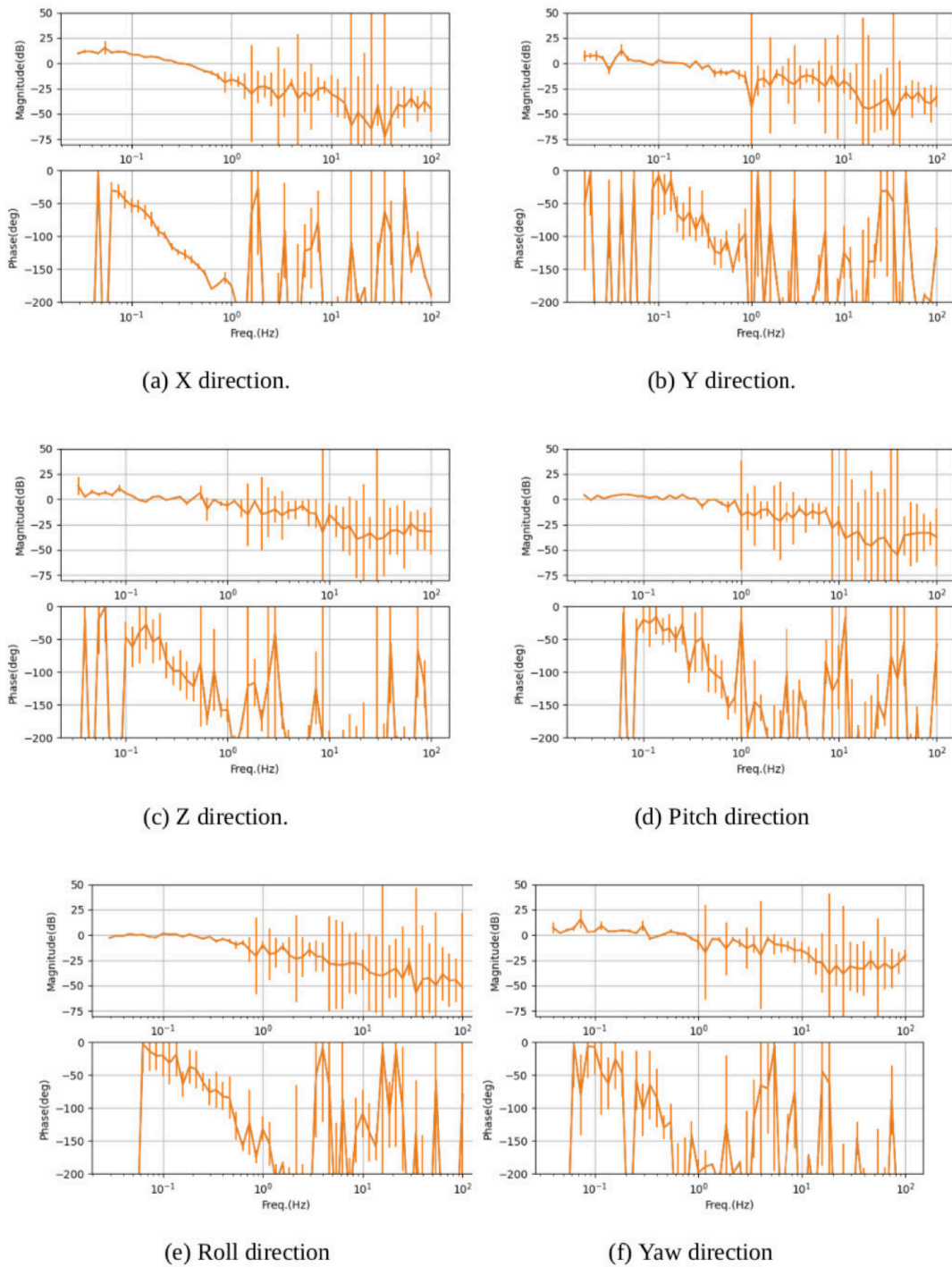


Figure 9.12: Open-loop transfer function of the control system. The unity gain frequency is approximately 1 Hz, and the phase margin indicates stable feedback operation.

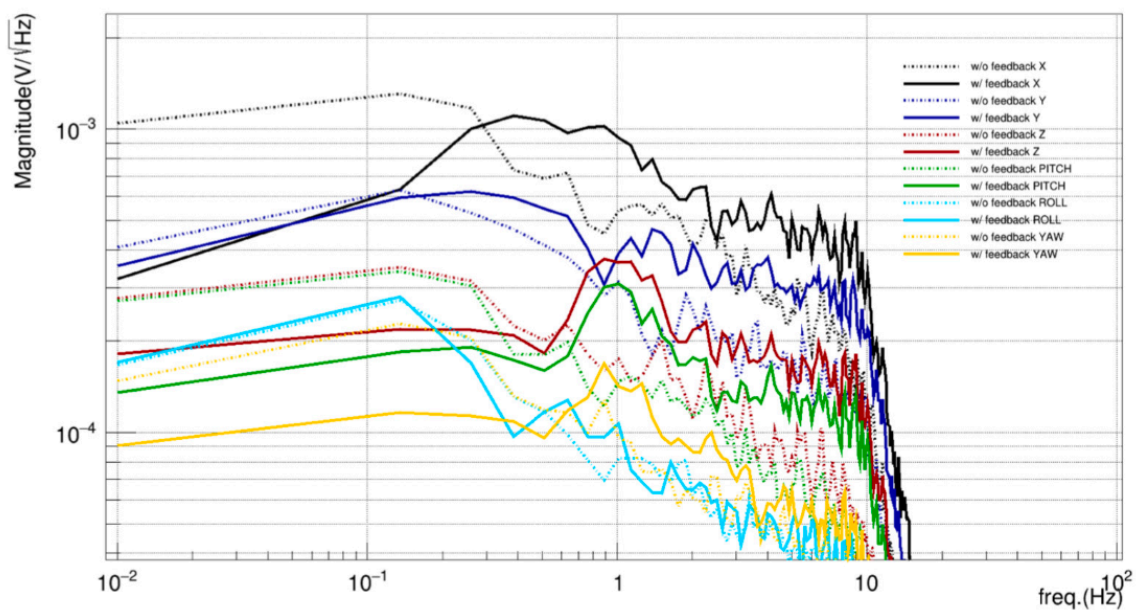


Figure 9.13: Comparison of noise spectra before and after feedback control. Significant vibration reduction is achieved below 1 Hz with full 6-DOF control.

Mirror Coating

10.1 Introduction

Mirror coating research in CHRONOS constitutes one of the central technological developments required to achieve enhanced sensitivity in future low-frequency gravitational-wave observations. In particular, below ~ 100 Hz, coating Brownian noise is one of the dominant noise sources. Its amplitude is determined primarily by the mechanical loss of the coating materials and by optical losses, including absorption and scattering. Therefore, the development of coating materials that simultaneously exhibit low mechanical dissipation and ultra-low optical absorption is directly linked to improving gravitational-wave detector sensitivity.

Future low-frequency interferometers are expected to operate in the cryogenic regime (10–120 K). Cryogenic operation effectively reduces thermal noise from both substrates and coatings; however, it also introduces additional challenges. Internal friction peaks and temperature-dependent absorption mechanisms may appear at low temperatures, potentially degrading detector performance. Consequently, coating materials must maintain low mechanical loss and low optical absorption not only at room temperature but also under cryogenic conditions. Since CHRONOS is designed explicitly for low-temperature operation, coating development is pursued with cryogenic material properties as a primary design requirement.

In current gravitational-wave detectors such as LIGO, mirror coatings are primarily fabricated using ion-beam sputtering (IBS). IBS coatings provide excellent optical qual-

ity, low scattering, and high uniformity across large optical substrates, which has been essential for kilometer-scale interferometers.

In parallel with IBS-based technologies, alternative coating approaches are being investigated. Chemical Vapor Deposition (CVD), including Plasma-Enhanced CVD (PECVD) and Low-Pressure CVD (LPCVD), offers attractive advantages due to the precise control of film thickness and stoichiometry developed in semiconductor manufacturing. Taiwan's semiconductor fabrication infrastructure provides a strong technological basis for this research, enabling highly reproducible thin-film deposition.

For CHRONOS, large-area coatings are not a primary requirement because the interferometer employs relatively small optical elements. Instead, emphasis is placed on materials that exhibit intrinsically low mechanical loss at cryogenic temperatures. Recent studies indicate that silicon nitride (SiN) and silicon oxynitride (SiON) films deposited by LPCVD can achieve exceptionally low mechanical loss, particularly at low temperatures. Therefore, CHRONOS promotes the development of LPCVD-based SiN/SiON coatings as promising candidates for cryogenic interferometric mirrors.

At present, optimization of film composition and film thickness is still under active research and development in order to further improve optical performance and mechanical properties.

CHRONOS has been advancing PECVD and LPCVD processes for amorphous silicon (a-Si), SiN, and SiON multilayers. These materials are promising candidates for high-index and low-index layers and have demonstrated the potential for low mechanical loss and reduced optical absorption at cryogenic temperatures.

In addition to exploring CVD-based fabrication, this effort also provides an independent validation platform for a-Si, SiN, and SiON films deposited by IBS in other collaborations. Ultimately, the optimized materials may be implemented either through advanced CVD techniques or through IBS deposition for final detector-grade optics. If ongoing research within the gravitational-wave community, including the extensive R&D efforts of the LIGO collaboration, demonstrates that IBS coatings provide superior performance under cryogenic conditions, CHRONOS will adopt the most suitable coating technology based on experimental evidence.

In the present phase, multilayer coatings are fabricated on 3-inch silicon wafers to optimize deposition parameters, including temperature, pressure, gas flow rates, and RF power. The targeted performance metrics are:

- Operating wavelength: 1064 nm (with optional extension to 1550 nm),
- Cryogenic mechanical loss angle: below 10^{-5} in the 10 K range at ~ 10 Hz.

These specifications are required to substantially suppress coating Brownian noise in next-generation cryogenic gravitational-wave detectors.

10.2 High-Low Dielectric Multilayer Coatings

High–Low coatings consist of alternating layers of high-index (n_H) and low-index (n_L) dielectric materials and constitute the core technology of test-mass mirrors in laser interferometric gravitational-wave detectors. Such structures can be regarded as one-dimensional photonic crystals, where periodic modulation of the refractive index produces strong Bragg reflection at a design wavelength.

10.2.1 Fresnel reflection at a single interface

For normal incidence, the amplitude reflection coefficient at an interface between media of refractive indices n_1 and n_2 is given by the Fresnel formula

$$r_{12} = \frac{n_1 - n_2}{n_1 + n_2}, \quad (10.1)$$

with the corresponding intensity reflectance

$$R_{12} = |r_{12}|^2. \quad (10.2)$$

For typical dielectric interfaces, R_{12} is only a few percent. However, in a multilayer structure, the reflected waves from each interface interfere coherently, leading to a dramatic enhancement of the overall reflectivity.

10.2.2 Quarter-wave ($\lambda/4$) design

To achieve constructive interference of reflected waves, each layer is designed to satisfy the quarter-wave condition

$$n_i d_i = \frac{\lambda}{4}, \quad (10.3)$$

where d_i is the physical thickness and λ is the design wavelength in vacuum. The corresponding phase thickness is

$$\delta_i = \frac{2\pi}{\lambda} n_i d_i = \frac{\pi}{2}. \quad (10.4)$$

Under this condition, the round-trip phase shift in each layer is π , ensuring that reflections from all interfaces add in phase at λ . This constitutes the Bragg reflection condition.

10.2.3 Transfer matrix formalism

A rigorous description of multilayer reflectivity is obtained using the transfer matrix method (TMM). This method provides a systematic way to calculate reflection and transmission of electromagnetic waves propagating through a stack of thin films.

We consider a monochromatic electromagnetic wave propagating along the z direction. Inside a homogeneous layer the electric field can be written as the superposition of forward- and backward-propagating waves,

$$E(z) = E^+ e^{ikz} + E^- e^{-ikz}. \quad (10.5)$$

Optical absorption in the coating material is incorporated through the complex refractive index

$$\tilde{n}_i = n_i + ik_i, \quad (10.6)$$

which corresponds to the complex dielectric constant

$$\tilde{\varepsilon}_i = \tilde{n}_i^2. \quad (10.7)$$

Here k_i is the extinction coefficient describing optical absorption.

According to Maxwell's equations, the tangential components of the electric and magnetic fields must be continuous at each interface between two layers. It is therefore convenient to represent the field by the vector

$$\mathbf{\Psi}(z) = \begin{pmatrix} E(z) \\ H(z) \end{pmatrix}, \quad (10.8)$$

where the magnetic field can be written as

$$H(z) = \frac{1}{Z_i} (E^+ e^{ikz} - E^- e^{-ikz}), \quad (10.9)$$

and Z_i is the optical impedance of layer i .

Propagation through a layer of thickness d_i can then be expressed by the transfer matrix

$$\begin{pmatrix} E(z + d_i) \\ H(z + d_i) \end{pmatrix} = M_i \begin{pmatrix} E(z) \\ H(z) \end{pmatrix}, \quad (10.10)$$

with the characteristic matrix

$$M_i = \begin{pmatrix} \cos \delta_i & iZ_i \sin \delta_i \\ \frac{i}{Z_i} \sin \delta_i & \cos \delta_i \end{pmatrix}, \quad (10.11)$$

where the phase thickness is

$$\delta_i = \frac{2\pi}{\lambda} \tilde{n}_i d_i. \quad (10.12)$$

For a stack consisting of N layers, the total system matrix is obtained as the ordered product

$$M = M_N M_{N-1} \cdots M_1 = \begin{pmatrix} A & B \\ C & D \end{pmatrix}. \quad (10.13)$$

To determine the reflection coefficient, we apply boundary conditions at the entrance and exit of the multilayer. If the incident wave has amplitude E_0 , the field in the incident medium ($z < 0$) can be written as

$$E(z) = E_0 e^{ik_0 z} + r E_0 e^{-ik_0 z}. \quad (10.14)$$

On the substrate side ($z > L$), only a transmitted wave exists,

$$E(z) = t E_0 e^{ik_s z}. \quad (10.15)$$

Using these boundary conditions together with the system matrix relation, the amplitude reflection coefficient can be expressed in terms of the matrix elements

$$r = \frac{(A + B n_s) n_0 - (C + D n_s)}{(A + B n_s) n_0 + (C + D n_s)}. \quad (10.16)$$

Finally, the reflectance is given by

$$R = |r|^2. \quad (10.17)$$

10.2.4 Ideal quarter-wave stack

For an ideal symmetric quarter-wave stack consisting of N pairs of alternating high- and low-index layers, the reflectance can be approximated analytically as

$$R \simeq \left(\frac{(n_H/n_L)^{2N} - 1}{(n_H/n_L)^{2N} + 1} \right)^2. \quad (10.18)$$

The reflectance increases exponentially with the number of layer pairs. With several tens of layers, reflectivities exceeding

$$R > 99.999\% \quad (10.19)$$

are routinely achieved, enabling high-finesse arm cavities in gravitational-wave interferometers.

10.3 LPCVD fabrication

LPCVD is a thin-film deposition method which is used for the production of films with uniform thickness, high purity and the ability to cover complex surface designs. LPCVD creates thin films through chemical reactions between gaseous precursors which occur at high temperatures and low pressure settings that operate around few hundred mTorr. The Low-pressure operation minimizes gas molecules collision, resulting in an even distribution of reactants that will mostly interact with the surface of the wafer. This process uses a horizontal quartz tube furnace as shown in figure 10.1 for its operations, which allows operators to load multiple wafers through a boat system that enters the reaction zone at controlled temperature. The process requires precise management of temperature and pressure and gas flow as these factors impact both deposition rates and film composition and microstructural characteristics. LPCVD films have hydrogen concentrations that are usually lower than those of PECVD, and, consequently, they possess better density, optical and mechanical stability. Therefore, LPCVD is the best option for producing low-loss optical coatings.

10.3.1 Growth Kinetics and Surface-Reaction Control

The deposition process begins with nucleation before entering the stages of grain formation and coalescence and continuous film growth which produces dense uniform layers which is illustrated in figure 10.2. The LPCVD growth process proceeds through the following fundamental steps:

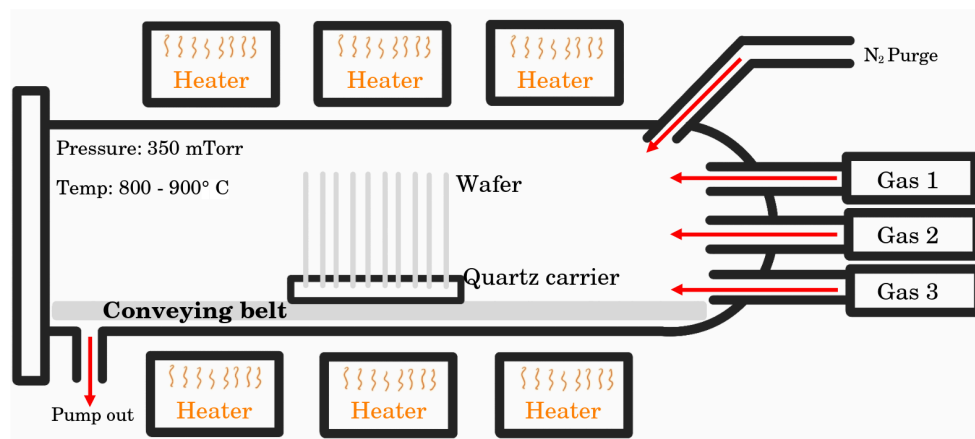


Figure 10.1: Schematic diagram of LPCVD furnace chamber.

1. Gas-phase transport of precursor molecules to the substrate surface
2. Adsorption of reactant species onto surface sites
3. Thermally activated surface reactions and bond formation
4. Desorption of volatile reaction by-products

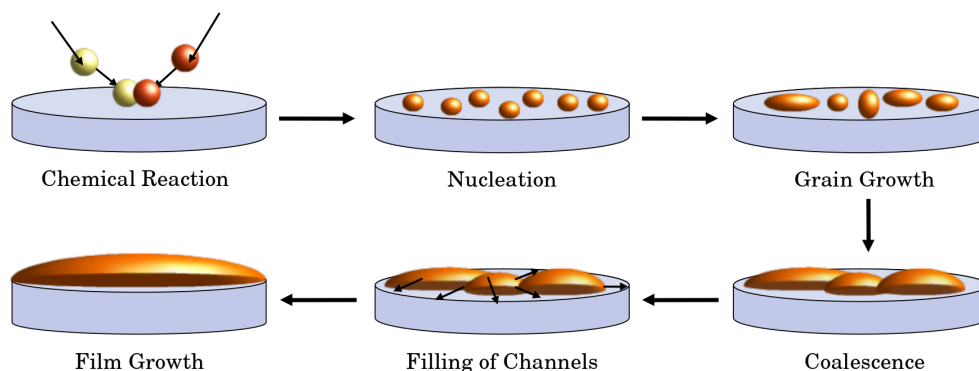


Figure 10.2: Process of film growth on wafer inside the LPCVD furnace.

10.4 Material: *a*-Si, SiN, SiON

The LPCVD method of film deposition exhibits its most important feature when it is applied to multilayer systems because their combined interface defects create problems which reduce both optical performance and mechanical strength [63].

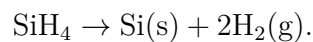
Each material fulfills a distinct functional role:

1. The first material *aSi* delivers high refractive index contrast which enables optical confinement and interference-based structural design.
2. The second material *SiN* functions as a dielectric layer which maintains mechanical strength while it supports tensile forces and prevents material diffusion.
3. The third material *SiON* provides a gradual shift in optical and mechanical characteristics which extends between its two adjacent layers to prevent sudden interface breaks.

The combined use of these materials allows multilayer stacks to be engineered beyond simple optical optimization, incorporating mechanical and thermodynamic stability as primary design parameters.

10.4.1 Material-Specific LPCVD Processes

Amorphous Silicon (a-Si): Amorphous silicon films deposited by LPCVD are commonly formed through the thermal decomposition of silane gas according to



Deposition occurs at temperatures below the crystallization threshold of silicon. In this temperature regime, long-range atomic ordering cannot develop, and the material forms a continuous random network primarily composed of silicon atoms in tetrahedral coordination. Because of the structural disorder inherent to the amorphous phase, coordination defects known as dangling bonds are inevitably present.

These defects introduce localized electronic states within the forbidden bandgap. Such mid-gap states enable optical transitions that absorb sub-bandgap photons, leading to a measurable extinction coefficient $\kappa(\lambda)$ at photon energies below the fundamental absorption edge. The density and distribution of these defect states depend strongly on the growth conditions, particularly the deposition temperature and the amount of hydrogen released during film growth.

LPCVD processes typically produce films with significantly lower hydrogen incorporation compared to plasma-assisted deposition techniques. This results in higher

structural density, improved thermal stability, and reduced defect formation. However, the residual structural disorder intrinsic to amorphous silicon remains a fundamental characteristic, which contributes to both optical absorption and mechanical energy dissipation [102, 65].

Despite these limitations, amorphous silicon is an attractive candidate for high-index layers in dielectric mirror coatings because of its large refractive index ($n \sim 3.4$ at near-infrared wavelengths). When paired with low-index materials such as silicon nitride (SiN) or silicon oxynitride (SiON), *a*-Si enables the realization of high-reflectivity multilayer stacks with a reduced number of layers compared to conventional oxide-based coatings.

Recent studies have also indicated that carefully optimized *a*-Si films can exhibit relatively low mechanical loss at cryogenic temperatures, making them promising for low-frequency gravitational-wave detectors. Nevertheless, optical absorption in *a*-Si remains an important challenge, and ongoing research focuses on reducing sub-bandgap absorption through optimization of deposition parameters, hydrogen control, and post-growth annealing processes.

Silicon Nitride (SiN_x): Stoichiometric silicon nitride films can be synthesized in LPCVD reactors using dichlorosilane (DCS) and ammonia precursors according to



The elevated deposition temperature promotes the formation of strong Si–N covalent bonds, producing a highly cross-linked amorphous network structure with near-stoichiometric composition. As a result, LPCVD silicon nitride films exhibit high mass density, low hydrogen incorporation, and extremely low impurity concentration.

Silicon nitride possesses a wide electronic bandgap exceeding 5 eV, which suppresses electronic absorption in the visible and near-infrared wavelength ranges. Consequently, LPCVD SiN_x films typically exhibit very low optical absorption and scattering losses while maintaining stable refractive index characteristics [45, 113].

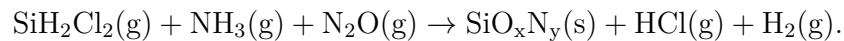
Deviations from the stoichiometric composition modify the bonding configuration

and lead to silicon-rich or nitrogen-rich films. Such compositional variations influence several key properties, including the refractive index, internal stress, and optical absorption. In optical coatings, this tunability enables optimization of the refractive index contrast when SiN_x is paired with high-index materials such as amorphous silicon.

A distinctive characteristic of LPCVD SiN_x films is their intrinsic tensile stress, which originates from atomic packing constraints during film growth. Although excessive stress can compromise the mechanical integrity of suspended structures, controlled tensile stress can significantly enhance elastic energy storage and reduce effective mechanical dissipation through the mechanism of dissipation dilution [82, 72]. These properties make LPCVD SiN_x an attractive candidate for low-index layers in multi-layer mirror coatings designed for cryogenic gravitational-wave detectors.

Silicon Oxynitride (SiO_xN_y): Silicon oxynitride (SiO_xN_y) is an intermediate dielectric material formed by incorporating both oxygen and nitrogen into the silicon network during film deposition. In LPCVD processes, SiO_xN_y films can be synthesized by introducing oxidizing species such as nitrous oxide together with conventional silicon nitride precursors.

A representative reaction scheme can be written as



The atomic structure of SiO_xN_y consists of a continuous amorphous network containing mixed tetrahedral units with Si–O and Si–N bonds. Oxygen substitution modifies the local bonding environment while preserving the overall network connectivity, rather than forming separate oxide and nitride phases.

Because of this mixed bonding configuration, the optical properties of SiO_xN_y can be tuned continuously between those of silicon dioxide and silicon nitride. To first approximation, the refractive index can be expressed as a compositional interpolation

$$n_{\text{SiON}}(\lambda) \approx x n_{\text{SiN}}(\lambda) + (1 - x) n_{\text{SiO}_2}(\lambda),$$

where x represents the effective nitrogen fraction in the film.

This compositional tunability allows SiO_xN_y to serve as an index-engineered dielectric layer in optical coatings. By gradually adjusting the oxygen-to-nitrogen ratio, refractive index transitions can be realized without abrupt interfaces, thereby reducing optical scattering and interfacial stress.

Compared with stoichiometric silicon nitride, SiO_xN_y films generally exhibit lower intrinsic stress while maintaining good chemical stability and dielectric performance. These characteristics make SiO_xN_y particularly suitable for graded multilayer coatings and transition layers that improve the mechanical robustness of precision optical stacks [13].

Data analysis

11.1 Data Processing Framework

The primary objective of data analysis in laser-interferometric gravitational-wave detectors is to identify gravitational-wave signals embedded in detector output and to extract their physical properties [5, 74]. The main observational targets include short-duration transient signals such as compact binary coalescences (CBC), and long-duration signals obtained through statistical integration, such as the stochastic gravitational-wave background (SGWB) [14, 28, 87].

The data analysis framework of CHRONOS follows established methodologies developed for ground-based interferometers such as LIGO [1], while incorporating modifications reflecting its unique characteristics, including sub-Hz sensitivity and torsional degree-of-freedom readout.

In the sub-Hz regime, detector output is strongly influenced by Newtonian noise, thermal noise, and environmental disturbances [50, 91, 34]. Therefore, long-duration stability, accurate noise characterization, and systematic uncertainty control are central elements of the CHRONOS data-processing strategy.

The overall data-processing pipeline is structured as follows:

- 1. Data acquisition (raw data)**

The detector output is recorded as a time-series of digitized voltage signals obtained via analog-to-digital conversion (ADC) of the photodetector output. These raw data contain the full detector response, including both signal and noise con-

tributions [1].

Given the torsional readout of CHRONOS, the primary observable corresponds to angular displacement or angular velocity of the test mass. Particular care is required to maintain long-term stability and low-frequency fidelity.

2. Calibration

The recorded voltage signals are converted into physical quantities such as gravitational-wave strain $h(t)$ or angular displacement. Calibration in CHRONOS relies on the torsional response function and absolute calibration using the photon calibrator and gravitational calibrator (GCal), enabling accurate reconstruction of the low-frequency response [62, 114].

Calibration uncertainty propagates directly into both CBC parameter estimation and Ω_{GW} inference, and is therefore treated as a systematic uncertainty in subsequent analyses [114].

3. Pre-processing and conditioning

The calibrated data are conditioned for analysis by computing spectral quantities such as $h(f)$, removing contaminated channels, and applying data-quality flags. This stage also includes formatting the data into standardized structures suitable for downstream analysis pipelines [109].

For CHRONOS, emphasis is placed on long-segment spectral estimation, mitigation of low-frequency environmental disturbances, and characterization of correlated noise relevant to SGWB estimation [50].

4. Processed data

The pre-processed data are stored in a unified format that can be shared across different analysis pipelines. These processed data serve as the common input for:

- Matched-filter searches for compact binary inspiral signals [109],
- Cross-correlation and auto-correlation analyses for Ω_{GW} estimation [14, 87],
- Long-duration stability studies and systematic noise characterization.

The separation between raw, calibrated, and processed data ensures reproducibil-

ity, traceability of systematic effects, and consistent treatment of statistical uncertainties across all scientific analyses.

11.2 Compact Binary Coalescence (CBC) Analysis

11.2.1 Detector response and data model

Compact binary systems emit gravitational waves whose frequency increases as the orbital separation shrinks due to gravitational radiation reaction. During the early inspiral phase, the signal evolves slowly and remains in the low-frequency band for an extended duration, making it particularly relevant for detectors operating below 1 Hz.

When a gravitational wave impinges on a detector, the observed strain is given by a linear combination of the two polarization components, h_+ and h_\times [74]. The detector sensitivity depends on the source direction and polarization state through the antenna pattern functions F_+ and F_\times . The measured strain signal can therefore be written as

$$h_{\text{obs}}(t) = F_+ h_+(t) + F_\times h_\times(t). \quad (11.1)$$

In practice, the detector output contains instrumental and environmental noise. The measured data stream $s(t)$ is thus expressed as

$$s(t) = h_{\text{obs}}(t) + n(t), \quad (11.2)$$

where $n(t)$ denotes the total noise contribution.

For CHRONOS, the physical observable is not directly the dimensionless strain but the torsional motion of the test mass, namely the angular displacement or angular velocity of the torsion bar. The quantity $h_{\text{obs}}(t)$ therefore represents the output after conversion from gravitational-wave strain through the full detector response function [1]. This response function incorporates both the mechanical susceptibility of the torsion system and the optical transfer function of the interferometric readout.

The CBC analysis presented in the following sections is therefore formulated in the

frequency domain using a noise-weighted inner product, where both the full detector response and the spectral properties of the noise are explicitly incorporated.

11.2.2 Signal-to-noise ratio and matched filtering

The statistical significance of a gravitational-wave signal is quantified by the signal-to-noise ratio (SNR). In gravitational-wave data analysis, the SNR is rigorously defined through a noise-weighted inner product in the frequency domain [39].

For two time-series $a(t)$ and $b(t)$, the inner product is defined as

$$(a|b) = 4 \operatorname{Re} \int_{f_{\min}}^{f_{\max}} \frac{\tilde{a}^*(f)\tilde{b}(f)}{S_n(f)} df, \quad (11.3)$$

where $\tilde{a}(f)$ and $\tilde{b}(f)$ denote the Fourier transforms of the time-domain signals and $S_n(f)$ is the one-sided power spectral density (PSD) of the detector noise.

Given detector data $s(t)$ and a template waveform $h(t)$, the matched-filter SNR is defined as

$$\operatorname{SNR} = \frac{(s|h)}{\sqrt{(h|h)}}. \quad (11.4)$$

In the ideal case where the data consist of signal plus stationary Gaussian noise, $s(t) = h(t) + n(t)$, the expected optimal SNR becomes

$$\operatorname{SNR}_{\text{opt}} = \sqrt{(h|h)}. \quad (11.5)$$

Using the Fourier-domain representation of the inspiral waveform derived in the previous section, the optimal SNR can be written explicitly as

$$\operatorname{SNR} = \left[4 \int_{f_{\min}}^{f_{\max}} \frac{|\tilde{h}(f)|^2}{S_n(f)} df \right]^{1/2}. \quad (11.6)$$

Substituting the stationary-phase inspiral amplitude, $|\tilde{h}(f)| \propto \mathcal{M}_c^{5/6} f^{-7/6}$, one obtains

$$\operatorname{SNR}^2 \propto \int_{f_{\min}}^{f_{\max}} \frac{f^{-7/3}}{S_n(f)} df. \quad (11.7)$$

This expression shows explicitly that the SNR accumulation depends both on the spectral shape of the inspiral signal and on the detector noise PSD. The strong $f^{-7/3}$ weighting indicates that low-frequency sensitivity plays a particularly important role in enhancing the detection significance.

In realistic detector data, however, the noise is not perfectly stationary nor purely Gaussian. Transient noise artifacts and spectral non-stationarity can bias the SNR. Therefore, in addition to the matched-filter SNR, detection confidence is evaluated using background estimation techniques and statistical measures such as the false alarm rate [109, 112].

For CHRONOS, several aspects are especially relevant in the SNR evaluation. First, the long-duration inspiral signals in the sub-Hz band imply extended coherent integration. Second, the frequency-dependent mechanical response of the torsion system modifies the effective strain sensitivity. Third, low-frequency noise sources such as Newtonian noise directly impact the integrand in Eq. (11.7). Finally, the absolute calibration accuracy, for example through gravitational calibration techniques [62, 114], affects the reliability of the inferred signal amplitude.

A consistent treatment of these factors is therefore required to determine the true detection sensitivity and astrophysical reach of CHRONOS.

11.2.3 SNR accumulation in the sub-Hz regime

According to Eq. (11.7), the integrand contains the factor $f^{-7/3}$, which strongly enhances the contribution from lower frequencies provided that the detector noise does not rise too steeply in this regime. This property reflects the slow orbital evolution of compact binaries during the early inspiral phase.

The physical origin of this low-frequency dominance can be understood from the time-to-coalescence relation,

$$t(f) = \frac{5}{256} \frac{1}{(\pi f)^{8/3}} \mathcal{M}_c^{-5/3}, \quad (11.8)$$

which shows that the binary spends a disproportionately long time emitting gravitational waves at low frequencies. Since matched filtering coherently integrates the signal over the duration of observation, the extended residence time in the sub-Hz band translates directly into enhanced SNR accumulation.

For stellar-mass compact binaries, the signal may remain in the sub-Hz regime for months to years before entering the ~ 10 – 100 Hz band accessible to ground-based interferometers such as Advanced LIGO. A detector sensitive below 1 Hz can therefore

track the inspiral evolution over a much longer baseline in time, accumulating phase information well before merger.

In addition to increasing the total SNR, low-frequency observation improves the conditioning of the parameter-estimation problem. Because the inspiral phase evolution is governed primarily by the chirp mass, extended phase tracking at low frequencies reduces degeneracies between intrinsic parameters and improves distance estimation through the overall amplitude scaling.

For CHRONOS, which is designed to operate in the sub-Hz band, this capability represents a fundamental scientific advantage. By observing the early inspiral phase inaccessible to conventional ground-based detectors, CHRONOS extends the observable portion of the binary evolution and enhances the cumulative SNR prior to merger. This extended sensitivity window naturally complements higher-frequency interferometers, forming a multi-band observational strategy for compact binary coalescences.

11.2.4 Scientific implications for CHRONOS

The ability to observe compact binary inspirals in the sub-Hz regime has several important scientific consequences. As shown in the previous sections, the SNR accumulation is strongly weighted toward low frequencies, and compact binaries spend a substantial fraction of their evolution in this band. A detector such as CHRONOS, operating below 1 Hz, therefore accesses an extended portion of the inspiral phase that is inaccessible to conventional ground-based interferometers.

One immediate implication is the improvement of parameter estimation. Because the inspiral phase evolution is governed predominantly by the chirp mass, long-duration phase tracking at low frequencies significantly enhances the precision with which \mathcal{M}_c can be determined. The extended baseline in time also reduces correlations among intrinsic parameters and improves the measurement of the luminosity distance through the overall amplitude scaling. This early accumulation of phase information strengthens the conditioning of the likelihood function used in matched-filter analysis.

Another important consequence is the possibility of early-warning detection. Since compact binaries remain in the sub-Hz band months to years before merger, CHRONOS

could identify candidate events well before they enter the $\sim 10\text{--}100$ Hz band of ground-based detectors. Such early identification enables coordinated multi-band gravitational-wave observations, where low-frequency detectors track the early inspiral while high-frequency interferometers observe the late inspiral and merger. This multi-band strategy enhances both detection confidence and astrophysical inference.

Furthermore, early detection in the sub-Hz regime opens the prospect of multi-messenger coordination. Advance alerts issued prior to merger would allow electromagnetic and neutrino observatories to prepare targeted follow-up observations, increasing the likelihood of capturing prompt or precursor emission associated with compact binary coalescences.

From a broader perspective, CHRONOS contributes to a hierarchical observational framework in which gravitational-wave signals are followed continuously across frequency bands. By extending the observable inspiral phase to earlier epochs of binary evolution, CHRONOS enhances the cumulative SNR, improves parameter estimation accuracy, and strengthens the synergy between low-frequency and high-frequency gravitational-wave detectors. This complementary role defines the scientific significance of CBC observations with CHRONOS.

11.3 Stochastic Gravitational-Wave Background (SGWB) Analysis

11.3.1 Statistical Description of the SGWB

A stochastic gravitational-wave background (SGWB) is produced by the superposition of a large number of unresolved gravitational-wave sources distributed throughout the Universe. Because individual signals cannot be separated in time or frequency, the background must be characterized statistically.

The SGWB is commonly described under the assumption that it is statistically isotropic, stationary, and Gaussian [14, 87]. Under these conditions, the background is fully specified by its second-order correlation function.

In cosmology and gravitational-wave astronomy, the energy density of the background is expressed in terms of the dimensionless quantity

$$\Omega_{\text{GW}}(f) = \frac{1}{\rho_c} \frac{d\rho_{\text{GW}}}{d \ln f}, \quad (11.9)$$

where ρ_{GW} is the gravitational-wave energy density and $\rho_c = 3H_0^2/(8\pi G)$ is the critical energy density of the Universe.

The strain power spectral density of the SGWB is related to $\Omega_{\text{GW}}(f)$ by

$$S_h(f) = \frac{3H_0^2}{2\pi^2} \frac{\Omega_{\text{GW}}(f)}{f^3}. \quad (11.10)$$

This relation shows that the strain spectrum increases toward low frequencies as f^{-3} for a flat energy density spectrum. Consequently, detectors operating at low frequencies can achieve significant sensitivity to cosmological gravitational-wave backgrounds.

For an isotropic and stationary background, the Fourier components of the strain satisfy

$$\langle \tilde{h}_A^*(f) \tilde{h}_B(f') \rangle = \frac{1}{2} \delta(f - f') \gamma_{AB}(f) S_h(f), \quad (11.11)$$

where $\gamma_{AB}(f)$ is the overlap reduction function (ORF) that encodes the relative geometry and response of the two channels or detectors.

Equation (11.11) provides the fundamental statistical signature of the SGWB: while the signal is correlated between detectors or readout channels according to $\gamma_{AB}(f)$, instrumental noises are generally uncorrelated. This property forms the basis of correlation-based detection methods for the SGWB.

11.3.2 Correlation-Based Detection Principle

The output of a gravitational-wave detector is a time series that contains both gravitational-wave signals and instrumental noise. For a given detector channel A , the measured

data can be written as

$$x_A(t) = h_A(t) + n_A(t), \quad (11.12)$$

where $h_A(t)$ denotes the strain induced by the stochastic gravitational-wave background and $n_A(t)$ represents the detector noise.

For a stochastic background, the gravitational-wave signal is itself a random process. Consequently, the power spectrum of the measured data becomes

$$P_A(f) = S_h(f)R_A(f) + P_A^{\text{noise}}(f), \quad (11.13)$$

where $R_A(f)$ is the detector response function and $P_A^{\text{noise}}(f)$ is the intrinsic detector noise spectrum.

Because both the SGWB signal and the instrumental noise contribute additively to the observed power spectrum, a single detector cannot in general distinguish between the two. Any measured excess power may be interpreted either as a gravitational-wave background or as a misestimation of the noise level.

This degeneracy can be broken by exploiting the fact that a gravitational-wave background produces correlated responses between detectors or independent readout channels, while instrumental noises are typically uncorrelated.

Consider two data streams $x_A(t)$ and $x_B(t)$:

$$x_A(t) = h_A(t) + n_A(t), \quad x_B(t) = h_B(t) + n_B(t). \quad (11.14)$$

If the instrumental noises are statistically independent,

$$\langle n_A(t)n_B(t') \rangle = 0, \quad (11.15)$$

then the expectation value of their correlation becomes

$$\langle x_A(t)x_B(t') \rangle = \langle h_A(t)h_B(t') \rangle. \quad (11.16)$$

In other words, the correlated component of the detector outputs isolates the gravitational-wave signal while suppressing the noise.

This property forms the basis of SGWB detection: instead of searching for excess power in a single detector, one measures the correlation between independent data streams.

The correlation amplitude accumulates coherently with observation time, while the contribution from uncorrelated noise averages toward zero. As a result, the signal-to-noise ratio improves with the square root of the integration time,

$$\text{SNR} \propto \sqrt{T}. \quad (11.17)$$

This statistical accumulation makes correlation techniques particularly powerful for detecting extremely weak stochastic backgrounds. The same principle applies both to cross-correlation between spatially separated detectors and to internal correlation between independent readout channels within a single detector.

11.3.3 General Correlation Estimator

To extract the correlated gravitational-wave signal from two data streams, we construct a correlation estimator in the frequency domain.

Let $x_A(t)$ and $x_B(t)$ denote the outputs of two detector channels. Their Fourier transforms are defined as

$$\tilde{x}(f) = \int_{-\infty}^{\infty} dt x(t) e^{-2\pi i f t}. \quad (11.18)$$

We define the correlation statistic

$$Y_{AB} = \int_{-\infty}^{\infty} df \tilde{x}_A^*(f) \tilde{x}_B(f) Q_{AB}(f), \quad (11.19)$$

where $Q_{AB}(f)$ is a filter function that determines how different frequency components contribute to the estimator.

The purpose of the filter is to weight frequency bins according to their expected signal strength and noise level. In practice, this filter is chosen to maximize the signal-to-noise ratio of the estimator.

The statistic Y_{AB} measures the integrated correlation between the two channels across the observation band. Because the stochastic background produces correlated responses between detectors, while instrumental noises are assumed to be uncorrelated, the expectation value of Y_{AB} isolates the gravitational-wave contribution.

The correlation estimator defined in Eq. (11.19) provides a unified framework for SGWB searches. The same expression applies both to

- cross-correlation between independent detectors, and
- internal correlation between independent channels within a detector.

The difference between these strategies lies only in the physical interpretation of the response function and in the statistical properties of the detector noise.

In the following sections we evaluate the expectation value and variance of the estimator and derive the optimal filter that maximizes the detection sensitivity.

11.3.4 Expectation Value and Relation to Ω_{GW}

We now evaluate the expectation value of the correlation estimator defined in Eq. (11.19).

Substituting the detector outputs

$$x_A(t) = h_A(t) + n_A(t), \quad x_B(t) = h_B(t) + n_B(t), \quad (11.20)$$

into Eq. (11.19) gives

$$Y_{AB} = \int df (\tilde{h}_A^* + \tilde{n}_A^*)(\tilde{h}_B + \tilde{n}_B)Q_{AB}(f). \quad (11.21)$$

Taking the ensemble average and assuming that the detector noises are uncorrelated with each other and with the signal,

$$\langle n_A n_B \rangle = 0, \quad \langle h n \rangle = 0, \quad (11.22)$$

the expectation value becomes

$$\langle Y_{AB} \rangle = \int df \langle \tilde{h}_A^*(f) \tilde{h}_B(f) \rangle Q_{AB}(f). \quad (11.23)$$

For an isotropic, stationary, and Gaussian SGWB, the strain correlations between two channels satisfy

$$\langle \tilde{h}_A^*(f) \tilde{h}_B(f') \rangle = \frac{1}{2} \delta(f - f') \gamma_{AB}(f) S_h(f), \quad (11.24)$$

where $\gamma_{AB}(f)$ is the overlap reduction function (ORF) that describes the relative geometry and response of the two channels.

Substituting this relation into the expression above yields

$$\langle Y_{AB} \rangle = \frac{T}{2} \int df \gamma_{AB}(f) S_h(f) Q_{AB}(f). \quad (11.25)$$

Using the relation between the strain spectrum and the gravitational-wave energy density,

$$S_h(f) = \frac{3H_0^2}{2\pi^2} \frac{\Omega_{\text{GW}}(f)}{f^3}, \quad (11.26)$$

we obtain

$$\langle Y_{AB} \rangle = \frac{T}{2} \left(\frac{3H_0^2}{2\pi^2} \right) \int df \gamma_{AB}(f) \frac{\Omega_{\text{GW}}(f)}{f^3} Q_{AB}(f). \quad (11.27)$$

Equation (11.27) demonstrates that the expectation value of the correlation statistic is directly proportional to the gravitational-wave energy density spectrum.

The measured correlation amplitude is therefore linear in $\Omega_{\text{GW}}(f)$.

This property allows correlation measurements to be used as a direct estimator of the stochastic gravitational-wave background. Any statistically significant non-zero correlation between independent channels can thus be interpreted as a constraint on $\Omega_{\text{GW}}(f)$.

11.3.5 Variance and Optimal Filtering

To evaluate the statistical significance of the correlation estimator, we compute its variance under the assumption that the detector noises in the two channels are uncorrelated and dominate over the signal.

The variance of the estimator defined in Eq. (11.19) is

$$\sigma_{Y_{AB}}^2 = \langle Y_{AB}^2 \rangle - \langle Y_{AB} \rangle^2. \quad (11.28)$$

For a weak stochastic background, the contribution of the gravitational-wave signal to the variance can be neglected. The variance is therefore determined primarily by the detector noises.

Assuming stationary and uncorrelated noises,

$$\langle \tilde{n}_A^*(f) \tilde{n}_B(f') \rangle = 0, \quad (11.29)$$

and

$$\langle \tilde{n}_A^*(f) \tilde{n}_A(f') \rangle = \frac{1}{2} \delta(f - f') P_A(f), \quad (11.30)$$

where $P_A(f)$ and $P_B(f)$ are the one-sided noise power spectral densities of the two channels.

Substituting these relations into the expression for the estimator variance yields

$$\sigma_{Y_{AB}}^2 = \frac{T}{4} \int df P_A(f) P_B(f) |Q_{AB}(f)|^2. \quad (11.31)$$

The signal-to-noise ratio (SNR) of the measurement is then defined as

$$\text{SNR}_{AB} = \frac{\langle Y_{AB} \rangle}{\sigma_{Y_{AB}}}. \quad (11.32)$$

The filter function $Q_{AB}(f)$ can be chosen to maximize this SNR. Maximizing Eq. (11.31) for fixed $\langle Y_{AB} \rangle$ leads to the optimal filter

$$Q_{AB}(f) \propto \frac{\gamma_{AB}(f)\Omega_{\text{GW}}(f)}{f^3 P_A(f)P_B(f)}. \quad (11.33)$$

Substituting this optimal filter into the expression for the SNR yields

$$\text{SNR}_{AB}^2 = 2T \left(\frac{3H_0^2}{2\pi^2} \right)^2 \int_0^\infty df \frac{\gamma_{AB}^2(f)\Omega_{\text{GW}}^2(f)}{f^6 P_A(f)P_B(f)}. \quad (11.34)$$

Equation (11.34) reveals several universal properties of stochastic-background searches:

- The signal-to-noise ratio scales linearly with the background amplitude

$$\text{SNR} \propto \Omega_{\text{GW}}.$$

- The sensitivity improves with the square root of observation time

$$\text{SNR} \propto \sqrt{T}.$$

- The sensitivity is strongly weighted toward low frequencies through the f^{-6} factor.
- The detector geometry and response enter through the overlap reduction function $\gamma_{AB}(f)$.

These relations define the fundamental sensitivity of correlation-based SGWB searches. The specific detection strategy—whether cross-correlation between independent detectors or internal correlation within a detector—enters only through the definitions of the noise spectra and the overlap reduction function.

11.3.6 Cross-Correlation Between Independent Detectors

The standard strategy for detecting a stochastic gravitational-wave background is the cross-correlation of independent detectors [14, 87]. In this approach, the two data streams correspond to spatially separated instruments that measure the same gravitational-wave field.

Let $x_i(t)$ and $x_j(t)$ denote the outputs of detectors i and j . The measured signals can be written as

$$x_i(t) = R_i * h(t) + n_i(t), \quad x_j(t) = R_j * h(t) + n_j(t), \quad (11.35)$$

where R_i and R_j represent the detector response functions and n_i, n_j are the instrumental noises.

Because the detectors are geographically separated and operate independently, their instrumental noises are expected to be statistically uncorrelated,

$$\langle n_i(t)n_j(t') \rangle \approx 0. \quad (11.36)$$

As a result, the expectation value of the correlation estimator isolates the gravitational-wave contribution.

The correlated gravitational-wave response between the two detectors is described by the overlap reduction function (ORF) $\gamma_{ij}(f)$. This function depends on the relative separation, orientation, and antenna patterns of the detectors and quantifies the sensitivity of the detector pair to an isotropic SGWB.

The resulting signal-to-noise ratio is given by Eq. (11.34), with the detector noise spectra $P_i(f)$ and $P_j(f)$ and the ORF $\gamma_{ij}(f)$.

A key advantage of cross-correlation searches is their robustness against instrumental systematics. Because detector noises are physically independent, uncorrelated noise averages down with integration time, while the correlated gravitational-wave signal accumulates coherently.

Calibration uncertainties enter the analysis through the detector response functions. Let the calibrated strain data be written as

$$\tilde{x}_i(f) = (1 + \delta C_i(f))\tilde{h}_i(f) + \tilde{n}_i(f), \quad (11.37)$$

where $\delta C_i(f)$ represents a fractional calibration error. Such uncertainties modify the effective normalization of the correlation estimator but do not introduce spurious cor-

relations between detectors. Consequently, calibration errors typically act as multiplicative systematic uncertainties on the inferred value of Ω_{GW} rather than producing false detections.

For this reason, cross-correlation between independent detectors is considered the most robust and conservative method for SGWB searches and forms the basis of analyses performed by the global network of ground-based interferometers.

11.3.7 Internal Correlation Within a Detector

An alternative realization of the correlation technique is the use of independent readout channels within a single detector. In this case the two data streams correspond to different optical or mechanical modes that respond to the same gravitational-wave signal.

Let $x_a(t)$ and $x_b(t)$ denote two independent readout channels. Their outputs can be expressed as

$$x_a(t) = R_a * h(t) + n_a(t), \quad x_b(t) = R_b * h(t) + n_b(t), \quad (11.38)$$

where R_a and R_b represent the channel response functions.

The correlation estimator introduced in Eq. (11.19) remains valid, with the overlap reduction function replaced by an effective internal response function

$$\gamma_{ab}^{(\text{int})}(f), \quad (11.39)$$

which describes the relative coupling of the gravitational-wave signal to the two readout channels.

In contrast to cross-correlation between separate detectors, the instrumental noises of internal channels may not be strictly independent. Environmental disturbances or technical noise sources can couple simultaneously to multiple channels, leading to

correlated noise:

$$\langle n_a(t)n_b(t') \rangle \neq 0. \quad (11.40)$$

Such correlated noise can bias the correlation estimator and mimic a stochastic gravitational-wave signal. The control and characterization of correlated noise therefore becomes a central experimental challenge.

Calibration plays a particularly important role in this context. Because the gravitational-wave response of each channel is determined by its transfer function, any calibration error modifies the effective response functions $R_a(f)$ and $R_b(f)$. If these errors differ between channels, the inferred correlation amplitude may be systematically biased.

Accurate calibration of the detector response is therefore essential to distinguish genuine gravitational-wave correlations from instrumental artifacts. In particular, calibration systems such as photon calibrators provide an independent reference that allows the transfer functions of individual channels to be measured with high precision.

When noise correlations are sufficiently suppressed and the response functions are accurately calibrated, internal correlation measurements can achieve sensitivities comparable to those of detector networks. This approach is especially attractive for experiments operating in frequency bands where only a limited number of detectors are available.

For CHRONOS, which is designed to operate in the sub-Hz regime, internal correlation between independent readout channels provides a promising pathway for SGWB detection. At the same time, the suppression and quantitative modeling of correlated environmental noise sources such as Newtonian noise is essential to ensure the reliability of the measurement.

11.3.8 Systematic Effects and Correlated Noise

While correlation techniques suppress uncorrelated detector noise, a number of systematic effects can introduce biases in the correlation estimator. Understanding and controlling these effects is essential for reliable SGWB measurements.

Correlated environmental noise Environmental disturbances can couple simultaneously to multiple detectors or multiple readout channels within a detector. Examples include seismic motion, electromagnetic interference, and atmospheric density fluctuations that generate Newtonian noise [50].

If such disturbances affect two channels simultaneously, the resulting noise correlation

$$\langle n_A(t)n_B(t') \rangle \neq 0 \quad (11.41)$$

can produce a non-zero correlation estimator even in the absence of a gravitational-wave signal. This effect is particularly relevant for internal-correlation measurements and for geographically nearby detectors.

Quantitative modeling and subtraction of correlated environmental noise are therefore critical components of SGWB analysis.

Calibration uncertainty Another important systematic effect arises from uncertainties in the detector response functions. Let the calibrated strain data be written as

$$\tilde{x}(f) = (1 + \delta C(f))\tilde{h}(f) + \tilde{n}(f), \quad (11.42)$$

where $\delta C(f)$ represents a fractional calibration error.

In cross-correlation measurements between independent detectors, calibration uncertainties primarily act as multiplicative normalization errors on the inferred value of Ω_{GW} . Because they do not generate correlated noise between detectors, they do not produce false detections.

For internal correlation measurements, however, calibration errors may modify the relative response of different readout channels. Accurate calibration of the transfer functions is therefore essential to ensure that the measured correlation reflects the gravitational-wave signal rather than instrumental artifacts.

Calibration systems such as photon calibrators provide an independent reference for determining the detector response functions with high precision. Such calibration

techniques are particularly important for low-frequency detectors where long integration times are required.

Implications for SGWB searches The impact of systematic effects depends on the specific correlation strategy employed.

- Cross-correlation between independent detectors is robust against instrumental noise correlations but relies on a detector network.
- Internal correlation within a detector enables SGWB searches even in the absence of multiple detectors but requires stringent control of correlated noise and precise calibration.

In practice, both approaches are complementary. Cross-correlation provides a robust detection method, while internal correlation can extend sensitivity in frequency ranges where detector networks are sparse.

For experiments operating in the sub-Hz band, such as CHRONOS, long integration times and strong low-frequency environmental couplings make the quantitative treatment of systematic effects particularly important. Careful calibration, environmental monitoring, and correlated-noise modeling are therefore essential components of the SGWB analysis framework.

11.3.9 Application to CHRONOS

The CHRONOS detector is designed to operate in the sub-Hz frequency band, a regime that is largely unexplored by existing gravitational-wave observatories. In this frequency range, correlation-based searches for the stochastic gravitational-wave background offer unique scientific opportunities.

As shown in Eq. (11.34), the sensitivity of correlation measurements is strongly weighted toward low frequencies through the f^{-6} factor in the integrand. Detectors operating at lower frequencies therefore gain significant leverage in probing cosmological gravitational-wave backgrounds. In particular, the sub-Hz band is expected to contain important contributions from early-Universe processes such as inflation, phase

transitions, and cosmic-string networks.

CHRONOS employs a torsion-bar interferometer configuration that measures rotational motion of suspended test masses. This design provides high sensitivity at very low frequencies where conventional kilometer-scale interferometers are limited by seismic noise and suspension thermal noise.

Because only a limited number of detectors are currently planned in the sub-Hz band, the use of internal correlation between independent readout channels becomes an important strategy for SGWB searches. In CHRONOS, multiple sensing channels with distinct transfer functions can be constructed within a single instrument. The correlation formalism developed in the previous sections can therefore be applied directly, with the internal response function $\gamma_{ab}^{(\text{int})}(f)$ describing the relative coupling of the gravitational-wave signal to each channel.

A critical challenge for such measurements is the control of correlated environmental noise. At sub-Hz frequencies, disturbances such as Newtonian noise from seismic and atmospheric density fluctuations can couple to multiple channels simultaneously. Accurate modeling and monitoring of these environmental contributions are therefore essential for reliable SGWB searches.

Equally important is the precise calibration of the detector response. Because the inferred gravitational-wave energy density depends linearly on the measured correlation amplitude, any calibration error in the detector transfer functions directly translates into a systematic uncertainty on Ω_{GW} . Independent calibration systems, such as photon calibrators, provide a means to determine the response functions of individual channels with high precision and to validate the stability of the instrument over long integration times.

By combining precise calibration, environmental noise monitoring, and correlation-based analysis techniques, CHRONOS aims to establish a new observational window for stochastic gravitational-wave backgrounds in the sub-Hz band. The methodology described in this section provides the theoretical framework for interpreting these measurements and for quantifying the sensitivity of the experiment to cosmological gravitational-wave signals.

Calibration and Reconstruction

12.1 Gravitational Wave Strain

The primary observable in gravitational-wave detectors is the strain $h(t)$ reconstructed from the interferometer output. Accurate calibration is essential, as systematic errors in the strain directly propagate into biases in astrophysical parameters such as source distance, mass, and the stochastic gravitational-wave energy density Ω_{GW} [4, 116, 103].

Laser interferometers are typically operated under feedback control, which maintains the interferometer at its operating point (e.g., the mid-fringe condition). In such a closed-loop system, the error signal measured by the photodetector is actively suppressed by the control system and kept close to zero. Therefore, the error signal does not directly represent the physical displacement of the interferometer [3].

The process of extracting the externally induced displacement from this closed-loop system is referred to as reconstruction [116, 103]. While several implementations exist, the essential requirement is the precise characterization of the actuation function $A(\Omega)$ and the sensing function $C(\Omega)$ [4, 3].

In conventional interferometers, the signal is expressed in terms of arm-length variations. In contrast, CHRONOS is sensitive to the rotational degree of freedom of a torsion-bar test mass, and the signal is therefore naturally described in terms of angular displacement.

Figure 12.1 shows the feedback loop that includes the reconstruction. The gravitational

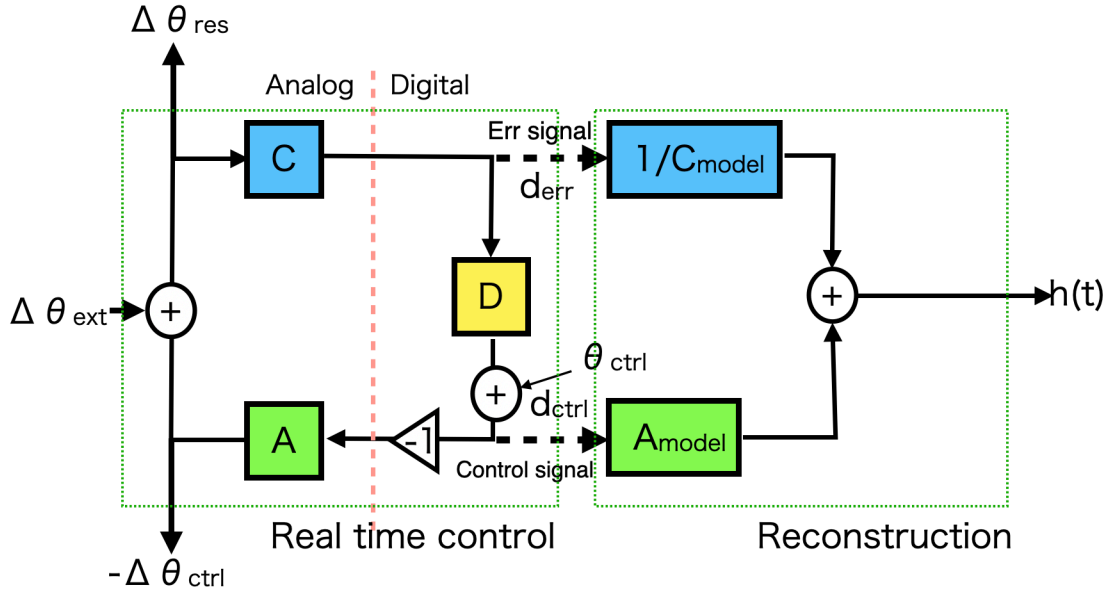


Figure 12.1: Schematic diagram of the feedback loop including the reconstruction process.

wave strain is described as:

$$h(t) = \frac{L_L(t) - L_R(t)}{L_{arm}} = \theta_L - \theta_R, \quad (12.1)$$

where L_{arm} is the effective length of arm and $\Delta\theta_{ext} = \theta_R(t) - \theta_L(t)$ is differential arm length caused by the external source [4].

The external displacement, $\Delta\theta_{ext}$, is calculated from both the digital error signal d_{ctrl} . Basically, $\Delta\theta_{ext}$ is calculated from the d_{err} alone. However, $\Delta\theta_{ext}$ is contracted with d_{err} and d_{ctrl} . So, we can calculate as:

$$\Delta\theta_{res} = \Delta\theta_{ext} - \Delta\theta_{ctrl} \quad (12.2)$$

$$d_{err} = C(t)\Delta\theta_{res} \quad (12.3)$$

$$\Delta\theta_{ctrl} = A(t)d_{ctrl}, \quad (12.4)$$

By combining with above equations, we can obtain

$$\Delta\theta_{ext} = \frac{d_{err}}{C} + Ad_{ctrl}. \quad (12.5)$$

In the frequency domain, Eq.(12.5) is simple multiplications. However, in the time

domain, d_{err} and d_{ctrl} are convolved with digital filters:

$$\Delta\theta_{ext}(t) = \left[\frac{1}{C} * d_{err} \right] + [A * d_{ctrl}], \quad (12.6)$$

where convolution is defined by $[F * G](t) = \int G(t')F(t - t')dt'$ [116].

In CHRONOS, the calibration procedure therefore consists of: (i) precise measurement of the actuation function $A(\Omega)$, (ii) characterization of the sensing function $C(\Omega)$, and (iii) verification of the loop gain $G(\Omega)$ through transfer-function measurements. Accurate determination of these quantities ensures reliable strain reconstruction over the full observation band.

12.2 Model

The open-loop gain of the differential angular degree of freedom is

$$\tilde{G}_\theta(\Omega) = \tilde{C}_\theta(\Omega, t)\tilde{D}_\theta(\Omega)\tilde{A}_\theta(\Omega, t), \quad (12.7)$$

where

- \tilde{C}_θ : sensing function,
- \tilde{D}_θ : digital control filter,
- \tilde{A}_θ : actuation function.

This formulation follows the standard linear control model used in ground-based interferometers [4, 3].

The response function is therefore

$$\tilde{R}_\theta(\Omega, t) = \frac{1 + \tilde{G}_\theta(\Omega, t)}{\tilde{C}_\theta(\Omega, t)} = \frac{1}{\tilde{C}_\theta(\Omega, t)} + \tilde{D}_\theta(\Omega)\tilde{A}_\theta(\Omega, t), \quad (12.8)$$

which directly generalizes the conventional DARM reconstruction to the angular degree of freedom of CHRONOS.

12.3 Photon Calibrator

Photon Calibrator (PCal) is a promising calibration method that has been deployed in the conventional gravitational-wave detectors [62, 37, 56]. It applies photon force to the test mass by injecting the power-controlled laser beams for generating an artificial harmonic displacement. As a result, it enables us to calibrate the displacement of the test mass against the known force.

When a beam of power P is injected to the test mass in the incident angle θ , the force applied in the translational direction is $2P \cos \theta / c$ using the speed of light c . The latest design of PCal system, which has been deployed by KAGRA, controls power of two beams independently and injects them on the nodal circle of the test mass to suppress excitation of its internal resonant mode [56, 62].

For CHRONOS, we extend the PCal system to four beams. These beams are injected to the back surface of the test mass to avoid interfering the main beam path. This enables us to control degrees of freedom of translation, yaw, and pitch independently. Having these degrees of freedom in control has several advantages; control of inclination of the beams in the triangle cavity, torque-based measurement of the position offset of the main interferometer beam, and application to a photon-pressure actuator for locking the interferometer.

We utilize the four-beams system for both PCal and photon-pressure actuator. Most of the laser power is assigned to the actuation for locking the cavity, and the rest is to the line injection as a PCal. In this section, we describe the projected performance when operating it as a PCal.

Actuation model

The injection positions are approximately symmetrically arranged around the center of mass of the bar as shown in Fig. 12.2. We label the four injection points by index $i = 1, 2, 3, 4$. We define the x-y plane by the surface of the bar and z axis by the translational direction, spanned by unit vectors $\vec{e}_x, \vec{e}_y, \vec{e}_z$. The position vector from the center of mass is written as $\vec{r}_i = (a_i, b_i, 0)$. As we see later, the injection positions should be

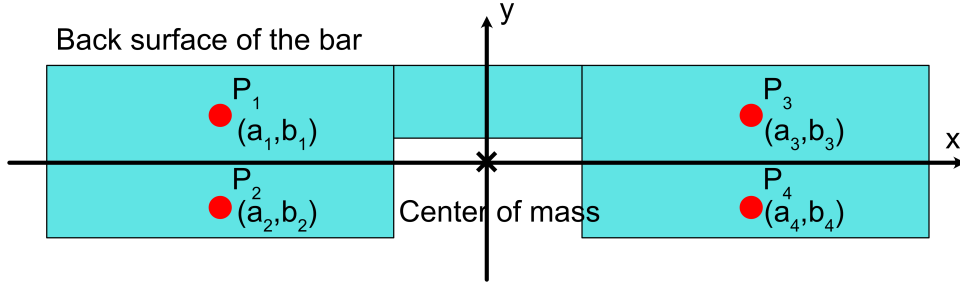


Figure 12.2: Conceptual positions and indices of the PCal beams on the CHRONOS torsion bar.

modified with consideration of avoiding excitation of the internal resonant modes.

We parameterize the force applied by each beam by beam power P_i , azimuthal incident angle θ_i , and inclination incident angle ϕ_i . Using these parameters, the force vector of the beam can be written as

$$\vec{F}_i = \left(\frac{2P_i(t) \cos \phi_i \sin \theta_i}{c}, \frac{2P_i(t) \sin \phi_i}{c}, \frac{2P_i(t) \cos \phi_i \cos \theta_i}{c} \right), \quad (12.9)$$

where c is the speed of light. Therefore, the net force in the translational direction and torques in the yaw and pitch rotation are

$$F_T(t) = \sum_i^4 \vec{F}_i \cdot \vec{e}_z, \quad (12.10)$$

$$T_Y(t) = \sum_i^4 (\vec{r}_i \times \vec{F}_i) \cdot \vec{e}_y, \quad (12.11)$$

$$T_P(t) = \sum_i^4 (\vec{r}_i \times \vec{F}_i) \cdot \vec{e}_x. \quad (12.12)$$

The equation of motion of translational displacement and rotations can be written as

$$M\ddot{z}(t) + \gamma\dot{z}(t) + kz(t) = F_T(t), \quad (12.13)$$

$$I_Y\ddot{\varphi}_Y(t) + \Gamma_Y\dot{\varphi}_Y(t) + K_Y\varphi_Y(t) = T_Y(t), \quad (12.14)$$

$$I_P\ddot{\varphi}_P(t) + \Gamma_P\dot{\varphi}_P(t) + K_P\varphi_P(t) = T_P(t), \quad (12.15)$$

where M is mass of the bar, I_Y and I_P are moment of inertia around each rotation axis, γ and Γ are damping coefficients, k and K are restoring coefficients originated to gravity and torsion spring coefficient.

The Eqs. (12.13)(12.14)(12.15) can be converted into the frequency domain by Laplace transform as

$$-M\omega^2 z(\omega) + i\omega\gamma z(\omega) + kz(\omega) = F_T(\omega), \quad (12.16)$$

$$-I_Y\omega^2 \varphi_Y(\omega) + i\omega\Gamma_Y \varphi_Y(\omega) + K_Y \varphi_Y(\omega) = T_Y(\omega), \quad (12.17)$$

$$-I_P\omega^2 \varphi_P(\omega) + i\omega\Gamma_P \varphi_P(\omega) + K_P \varphi_P(\omega) = T_P(\omega), \quad (12.18)$$

where $\omega \equiv 2\pi f$ for the frequency f . Therefore, the displacement and rotation angles in the frequency domain are

$$\begin{aligned} z(\omega) &= \frac{F_T(\omega)}{-M\omega^2 + i\omega\gamma + k} = \frac{F_T(\omega)}{-M\left(\omega^2 - i\frac{\Omega_T\omega}{Q_T} - \Omega_T^2\right)} \\ &\simeq -\frac{F_T(\omega)}{M\omega^2}, \end{aligned} \quad (12.19)$$

$$\begin{aligned} \varphi_Y(\omega) &= \frac{T_Y(\omega)}{-I_Y\omega^2 + i\omega\Gamma_Y + K_Y} = \frac{T_Y(\omega)}{-I_Y\left(\omega^2 - i\frac{\Omega_Y\omega}{Q_Y} - \Omega_Y^2\right)} \\ &\simeq -\frac{T_Y(\omega)}{I_Y\omega^2}, \end{aligned} \quad (12.20)$$

$$\begin{aligned} \varphi_P(\omega) &= \frac{T_P(\omega)}{-I_P\omega^2 + i\omega\Gamma_P + K_P} = \frac{T_P(\omega)}{-I_P\left(\omega^2 - i\frac{\Omega_P\omega}{Q_P} - \Omega_P^2\right)} \\ &\simeq -\frac{T_P(\omega)}{I_P\omega^2}, \end{aligned} \quad (12.21)$$

where

$$\Omega_T \equiv \sqrt{\frac{k}{M}}, \quad \Omega_Y \equiv \sqrt{\frac{K_Y}{I_Y}}, \quad \Omega_P \equiv \sqrt{\frac{K_P}{I_P}}, \quad (12.22)$$

$$Q_T \equiv \frac{\Omega_T M}{\gamma}, \quad Q_Y \equiv \frac{\Omega_Y I_Y}{\Gamma_Y}, \quad Q_P \equiv \frac{\Omega_P I_P}{\Gamma_P}. \quad (12.23)$$

The Ω represent the resonant frequencies, and the Q represents the quality factors of each degree of freedom (DoF). The resonant frequencies of the CHRONOS torsion bar are less than 1 Hz, and the quality factor of sapphire is typically at the order of 10^8 . Therefore, we neglected the Ω/Q and Ω^2 terms in Eqs. (12.19)(12.20)(12.21).

The yaw angle described by Eq. (12.20) mainly contributes to the strain-equivalent calibration amplitude,

$$h_{\text{PCal}}(\omega) = -\frac{2\varphi_Y(\omega)}{\eta_g |F_{\text{eff}}|} \frac{\omega^2 - i\frac{\Omega_Y \omega}{Q_Y} - \Omega_Y^2}{\omega^2} \simeq -2\varphi_Y(\omega). \quad (12.24)$$

Here the η_g is the geometrical coupling efficiency and the F_{eff} is the effective antenna pattern. Both η_g and F_{eff} are at the order of 1, thus we simplify the formula to the last term of Eq. (12.24).

12.3.1 Optical configuration

In order to realize the four-beams injection that powers and positions are independently controlled, we propose optics based on acousto-optic modulators (AOMs) coupled with optical follower servos (OFSs) and . This configuration has been demonstrated in Photon Calibrator studies in LIGO and KAGRA [62, 56, 59]. The OFS generates analog feedback signal to the AOM and also allows external input for changing the offset voltage.

Figure 12.3 shows a conceptual optical layout of the four-beams photon pressure actuator. It consists of the transmitter module, periscope, and receiver module. The transmitter module controls the beam power, while the receiver module monitors the reflected power and the beam positions. Beam orientations are adjusted at the periscope to hit the designated positions on the test mass.

Figure 12.4 shows the schematic diagram of the transmitter module. Powers and positions of the four beams should be independently controlled. We measure each beam power by a photodetector labeled as OFSPD. Each of four OFSPDs is connected to an OFS to feedback the intensity signal to AOM. Out of the feedback loop, an independent photodetector labeled as TxPD monitors each power. Each TxPD is coupled with integrated sphere to collect entire power of the beam. Beams for power monitoring are sampled from the transmitted beams by diffractive beam samplers. The mirrors at the final part of the transmitter module have picomotors to control orientations of the transmitted beams.

The beams reflected by the test mass are received by the receiver module. Figure 12.5 shows the schematic diagram of the receiver module. In the receiver module, the total

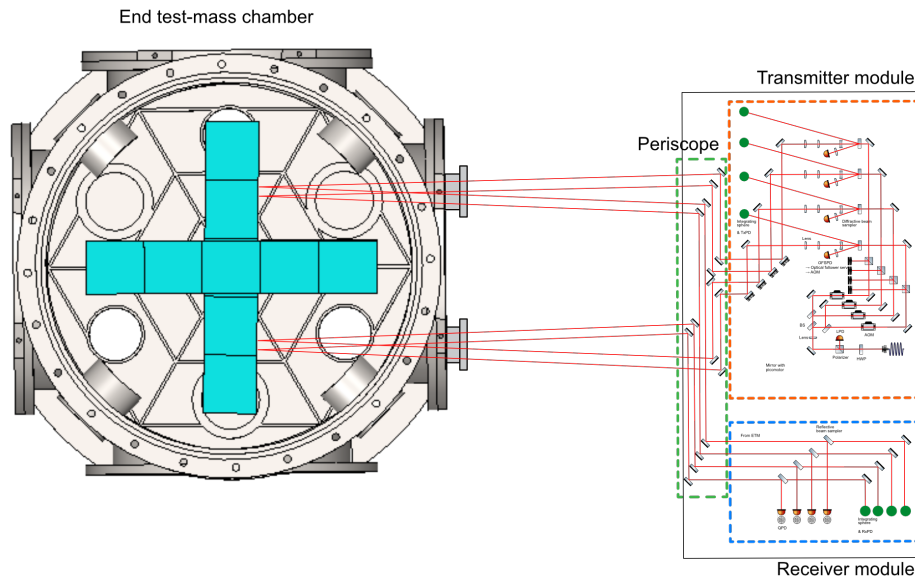


Figure 12.3: Conceptual optical layout of the CHRONOS PCal with the end test mass chamber. PCal setup for only one bar is shown.

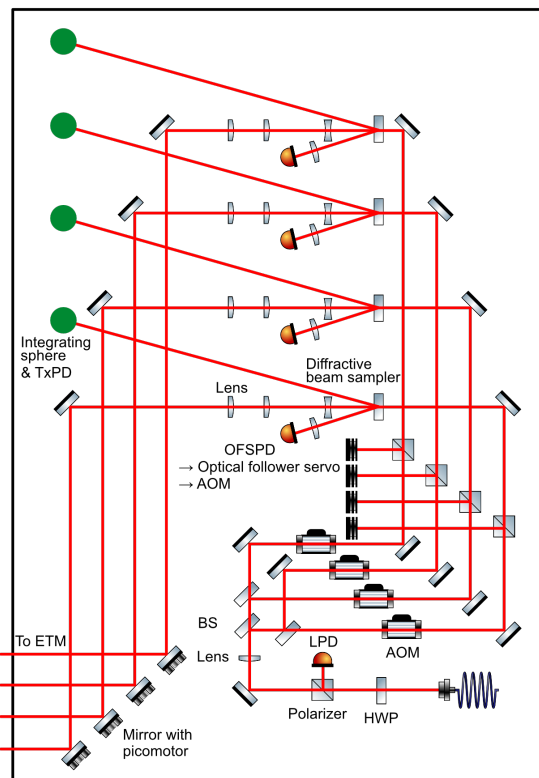


Figure 12.4: Conceptual optical layout of the transmitter module for CHRONOS PCal.

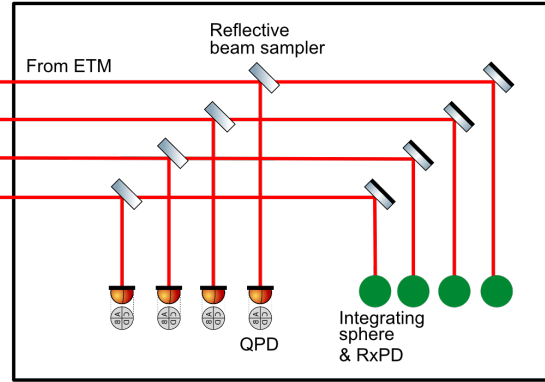


Figure 12.5: Conceptual optical layout of the receiver module for CHRONOS PCal.

power of the four beams is monitored by a photodetector labeled as RxPD, coupled with an integrating sphere. The small fraction of the beam is sampled by beam samplers and led to quadrant photodetectors for monitoring the beam positions.

12.3.2 Sensitivity comparison

Here we evaluate the actuation range of PCal with the realistic parameter values for CHRONOS as summarized in Table 12.1. We deploy a CNI FC-1550-10W, a fiber-coupled 10 W constant-wave laser with a wavelength of 1550 nm, as a laser source. It is split into four beams by beam splitters. We assume that the beams 3 and 4 are modulated in the opposite phase of the beams 1 and 2. When the torque reaches at its maximum, P_1 and P_2 are at the maximum while P_3 and P_4 are zero.

We have to limit the power of each beam to keep the PCal-induced calibration amplitude smaller than the wavelength of the main laser and also the PCal noise smaller than one-tenth of the total noise of the interferometer. We set these constraints at 1 Hz. As we calculate right below, we assign a power amplitude of $330 \mu\text{W}$ centered at $330 \mu\text{W}$ to P_2 and P_4 , while those of P_1 and P_3 should be $131 \mu\text{W}$ centered at $131 \mu\text{W}$ to meet the requirement. The difference of the power is for compensating the asymmetry of the beam positions in the vertical direction. The beam power is significantly smaller than PCals of LIGO and KAGRA, resulted from the conversion between rotation angle and strain being at the order of 1.

Incident angle on the torsion bar is constrained by the chamber size and the window

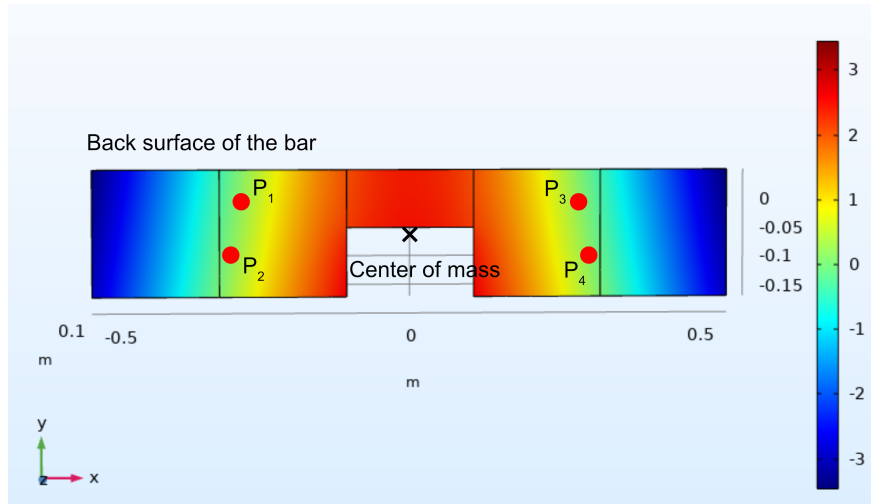


Figure 12.6: Injection positions of the CHRONOS PCal beams and the mode shape of the horizontal bending mode of the CHRONOS torsion bar at 1238 Hz simulated by COMSOL. Unit of the color legend is arbitrary.

size. We inject the beams through the window attached to the CF100 vacuum flange. Considering the effective diameter of the window is approximately 0.08 m and it is 0.8 m away from the surface of the torsion bar, the incident angle is 5.7° at most. The mass of the torsion bar is 171 kg, and the moment of inertia is $19.9 \text{ kg}\cdot\text{m}^2$ in yaw and $1.3 \text{ kg}\cdot\text{m}^2$ in pitch [57].

The injection positions should be on the nodal line of the internal resonant modes of the bar which couples to the rotation because the excitation of these modes can cause spurious rotation signal. The CHRONOS torsion bar has resonant modes at 667 Hz and 1237 Hz, where the first mode is the vertical bending mode and the second is the horizontal bending mode [104]. The second mode is relevant to the rotation signal, particularly when the main interferometer beams are at asymmetric positions due to unexpected beam offset.

Considering the maximum distance from the center of mass and the seams of the sapphire blocks where the mirrors should not be attached, we determine the injection positions as $(a_1, b_1) = (-0.306, 0.051)$, $(a_2, b_2) = (-0.321, -0.046)$, $(a_3, b_3) = (0.306, 0.051)$, $(a_4, b_4) = (0.321, -0.046)$ in the unit of meter. Figure 12.6 shows the shape of the 1238 Hz mode and the injection positions. The mode frequency and shape are simulated by COMSOL [31].

Parameter	Symbol	Value (Unit)
Peak-to-peak power of upper beam	P_1, P_3	≤ 261 (μW)
Peak-to-peak power of lower beam	P_2, P_4	≤ 660 (μW)
Azimuthal incident angle	$\theta_1, \theta_2, \theta_3, \theta_4$	≤ 5.7 ($^\circ$)
Inclination incident angle	$\phi_1, \phi_2, \phi_3, \phi_4$	≤ 5.7 ($^\circ$)
First beam position	(a_1, b_1)	(-0.306,0.053) (m,m)
Second beam position	(a_2, b_2)	(-0.317,-0.021) (m,m)
Third beam position	(a_3, b_3)	(0.306,0.053) (m,m)
Fourth beam position	(a_4, b_4)	(0.317,-0.021) (m,m)
Mass of the bar	M	171 (kg)
Moment of inertia of the bar (yaw)	I_{yaw}	19.9 ($\text{kg}\cdot\text{m}^2$)
Moment of inertia of the bar (pitch)	I_{pitch}	1.3 ($\text{kg}\cdot\text{m}^2$)

Table 12.1: Parameters related to the CHRONOS PCal.

Substituting these values into Eqs. (12.9)(12.11)(12.20)(12.24), we derive the signal amplitude induced by PCal. Figure 12.7 shows a comparison between the PCal signal and the noise budget of CHRONOS. Signal-to-noise ratio is 1733 at 1 Hz.

Noise budget

Laser intensity noise The laser power control system using the combination of AOM and OFS has been studied in the previous GW experiments for pre-stabilized input laser and PCal [23, 98, 29, 62, 56]. The power stabilization performed by KAGRA's PCal reported relative power noise (RPN) of -140dB in the frequencies higher than 100 Hz. The RPN rose by $1/f$ slope at below 100 Hz. We model it as $\text{RPN} = 1 \times 10^{-7}(1 + 100/f)$ and assume the same value as the RPN potentially achievable with our power control configuration.

Electronics noise When we operate the power control system for an actuator, in addition to the analog OFS for intensity stabilization, it involves digital control using the error signal of the interferometer. Precision of the digital control is limited by the digitization noise of the digital-to-analog converters (DACs). As analytically derived by Bennett (1948), the digitization noise of N -bit DAC can be modeled by $(2^N \sqrt{3/2})^{-1}$. When we use General Standard PCIe-16AO16-16-F0-DF which divides ± 10 V range

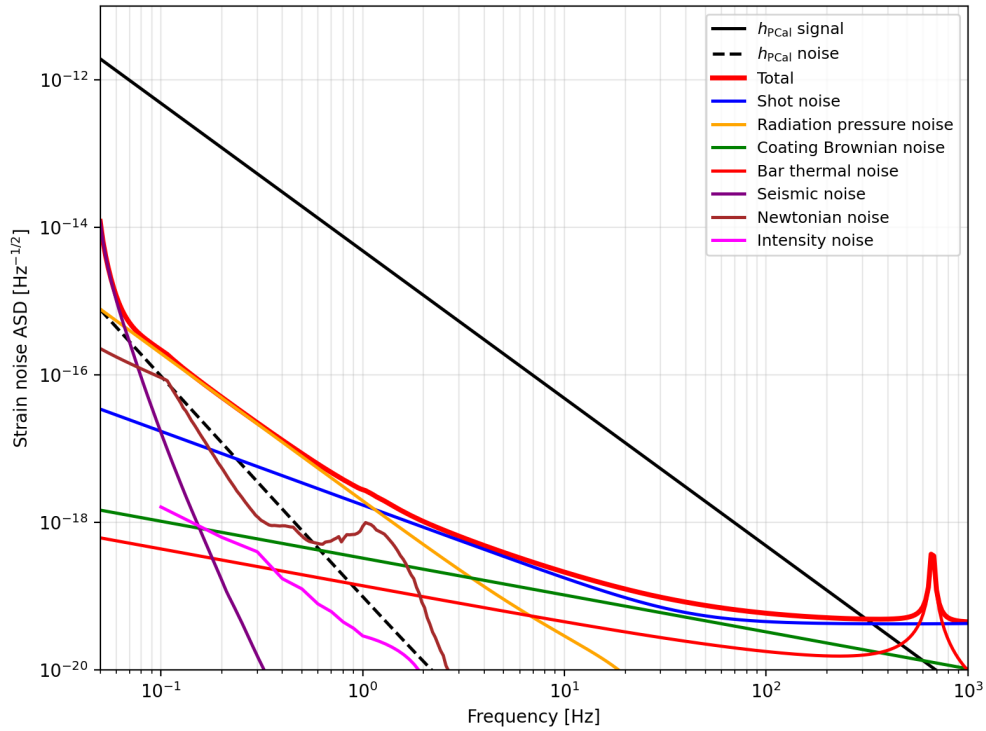


Figure 12.7: Noise budget of CHRONOS compared with the strain-equivalent calibration amplitude h_{PCal} generated by PCal.

by 16 bit, it limits the precision of output voltage to be more than $1.2 \times 10^{-5} \text{Hz}^{-1/2}$ ($-98 \text{ dBHz}^{-1/2}$).

The DAC noise propagates to the power fluctuation through an offset voltage applied to the OFS, thus to the AOM. As shown in Fig. 12.8, a slope of the power of the 1st order diffraction light with our AOM is $0.36/\text{V}$ when it is operated at 1.7 V to keep it 80% power of the maximum diffraction. Because our OFS is operated at a gain of 4, the output voltage from the DAC is around 0.43 V . It leads to a power fluctuation of $5.3 \times 10^{-6} \text{ Hz}^{-1/2}$ per unit power. For simplicity, we treat it as white noise.

Magnetic and seismic noise Photon pressure actuator does not couple with magnetic environment and the seismic noise. The magnetic field in the circumstance around the test mass and transmitter module does not affect to the laser power because a photon does not have charge. Vibration of the transmitter module does not change the photon pressure due to the constant speed of the light.

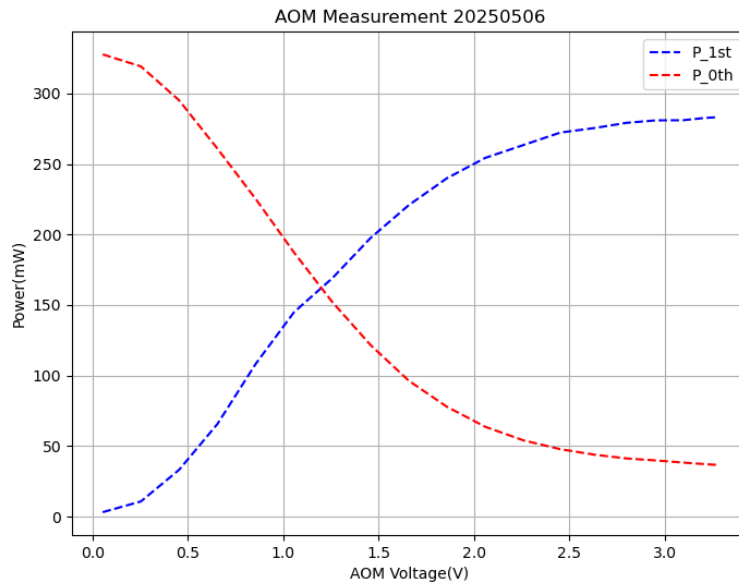


Figure 12.8: Diffraction efficiency of AOM with the bias voltage from the OFS. Blue: 1st order diffraction light, Red: 0th order diffraction light.

Total noise By combining quadratures of the laser intensity noise and electronics noise, we derive the noise curve of PCal as shown in Fig. 12.7.

Systematic error

In this study, uncertainty of beam power, incident angles, beam positions, moment of inertia, spurious yaw rotation induced by non-zero pitch angle, and bulk deformation are taken into account as systematic error sources. The detail is described by Tanabe *et al.* [105].

12.4 Torque-coupled Gravitational Calibrator (GCal)

In this study, we introduce a torque-coupled gravitational calibrator (GCal) that applies a purely Newtonian gravitational torque to a torsion-bar test mass [60, 59].

As illustrated in Fig. 12.9, a quadrupolar rotating rotor generates a time-modulated gravitational field, which couples directly to the rotational degree of freedom of the

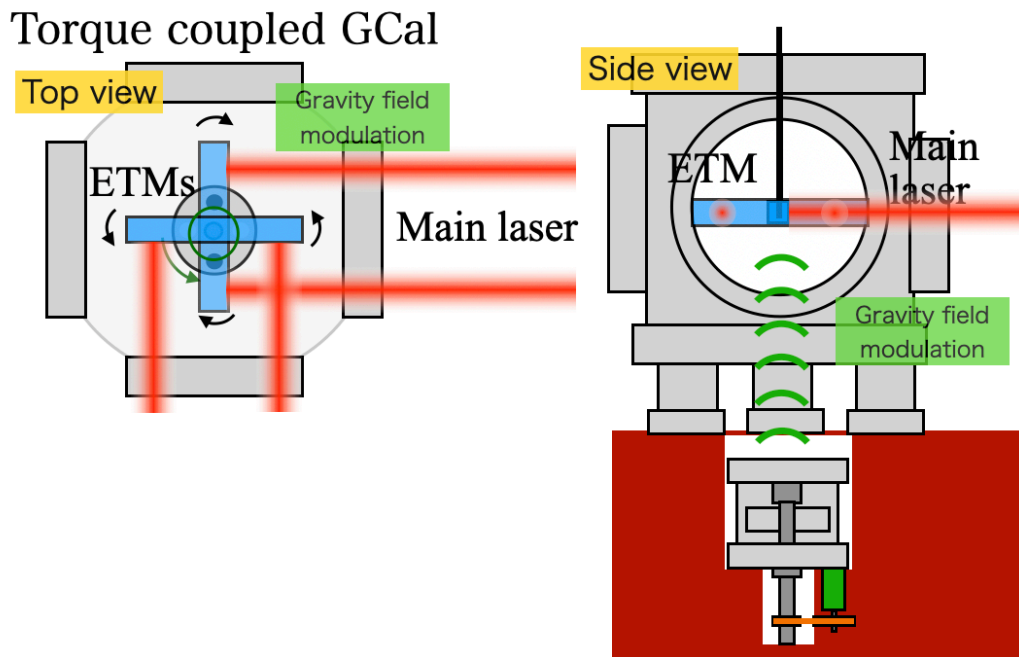


Figure 12.9: Conceptual schematic of the torque-coupled gravitational calibrator (GCal). A rotating quadrupolar mass distribution generates a time-modulated Newtonian gravitational field that couples directly to the torsional degree of freedom of the test mass. The dominant calibration signal appears at twice the rotor rotation frequency (2Ω).

test mass. The calibration signal appears at twice the rotor rotation frequency and can be described analytically from the known mass distribution and geometrical configuration.

The essential feature of this approach is that the gravitational interaction itself serves as the calibration source. In contrast to electromagnetic actuators or photon-pressure calibrators [62], the present scheme does not rely on the mechanical transfer function of the suspension system or on interferometer control-loop dynamics. Because the torque is applied directly to the rotational degree of freedom, a simple proportional relation between the applied gravitational torque and the detector response is established in the inertial regime.

This configuration provides a theoretically transparent and reproducible pathway for absolute calibration, enabling high-precision amplitude calibration in the sub-Hz frequency band.

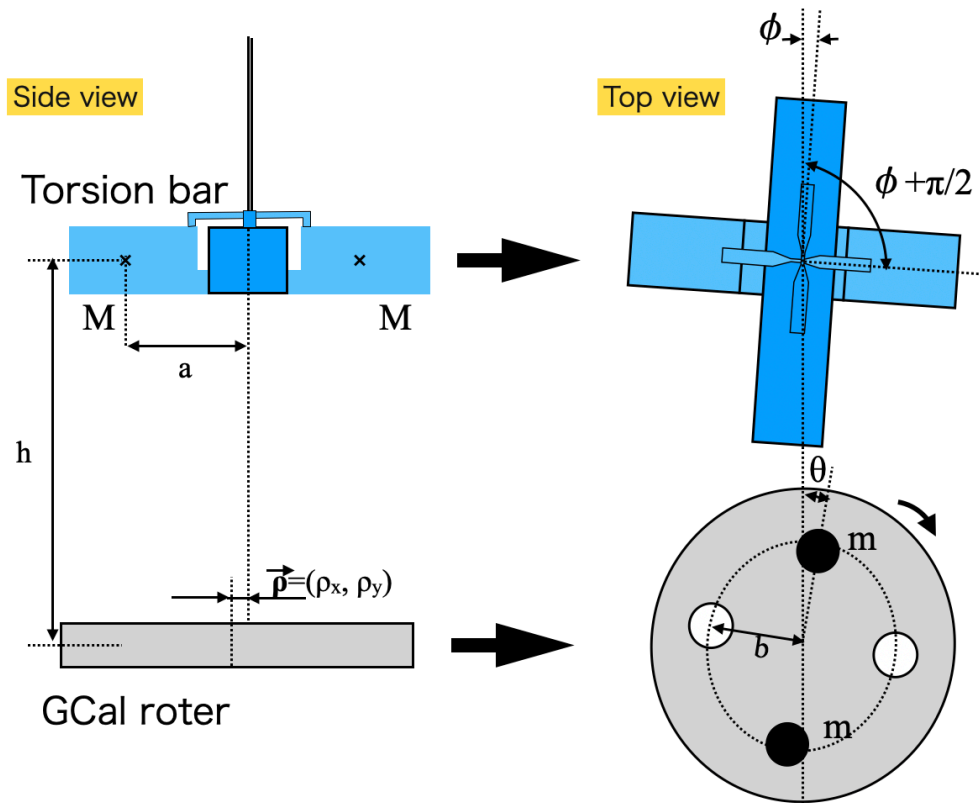


Figure 12.10: Geometrical configuration of the torque-coupled GCal. The system is characterized by four primary parameters: the effective lever arm length a , the rotor radius b , the vertical separation h , and the horizontal offset ρ_{\perp} . A representative interaction scale is defined as $R_0 = \sqrt{a^2 + b^2 + h^2 + \rho_{\perp}^2}$.

Geometrical configuration

The geometrical configuration of the torque-coupled GCal adopted in this study is illustrated in Fig. 12.9 and Fig. 12.10. In this scheme, a rotating mass distribution generates a time-modulated Newtonian gravitational field, which couples directly to the rotational degree of freedom of the torsion-bar test mass.

The rotor rotates uniformly with angular velocity Ω , and its angular position is given by

$$\theta(t) = \Omega t. \quad (12.25)$$

This periodic motion induces a time-dependent gravitational potential at the location of the test mass. As a result, a harmonic gravitational torque is generated, contain-

ing integer multiples of the rotation frequency. For a quadrupolar mass configuration, the dominant calibration signal appears at 2Ω , providing a well-defined narrow spectral line within the observation band, consistent with standard multipole-expansion arguments.

The geometry of the system is characterized by four primary parameters: the distance a from the torsion axis to the test mass, the rotor radius b defined as the distance from the rotor center to each rotating calibration mass, the vertical separation h between the rotor plane and the torsion bar, and the horizontal offset ρ_{\perp} between their symmetry axes.

The parameter a does not merely represent a geometric distance; rather, it corresponds to the *effective lever arm length* with respect to the rotational degree of freedom. It determines the moment arm through which the gravitational force acting on the test mass is converted into torque about the torsion axis. To leading order, the torque amplitude scales linearly with a , reflecting the relation

$$\tau \sim a F_{\text{grav}},$$

where F_{grav} denotes the gravitational force component perpendicular to the lever arm.

The rotor radius b determines the quadrupole moment of the rotating mass distribution and therefore sets the amplitude of the time-modulated gravitational potential. The vertical separation h defines the characteristic interaction distance, governing the overall gravitational coupling strength through the inverse-distance dependence of Newtonian gravity. The horizontal offset ρ_{\perp} quantifies deviations from perfect coaxial alignment and introduces symmetry-breaking corrections that appear as higher-order terms in the multipole expansion.

A representative distance scale between the rotating masses and the test mass can be defined as

$$R_0 = \sqrt{a^2 + b^2 + h^2 + \rho_{\perp}^2}, \quad (12.26)$$

which sets the characteristic scale of the gravitational interaction. In practice, the torque amplitude can be systematically derived by performing a multipole expansion around this reference distance, with the quadrupole term providing the dominant contribution for the symmetric configuration considered here.

These geometrical parameters determine not only the absolute calibration amplitude but also the systematic uncertainty budget. In particular, uncertainties in h and ρ_{\perp} enter at first order in the analytical derivatives of the torque expression, making precise mechanical alignment and position metrology essential for achieving sub-percent-level calibration accuracy.

Furthermore, we introduce a dimensionless geometrical parameter

$$\xi = \frac{2ab}{R_0^2}, \quad (12.27)$$

which characterizes the coupling between the effective lever arm length a of the torsion bar and the rotor radius b . The parameter ξ serves as the small expansion parameter in the multipole expansion of the gravitational torque arising from the quadrupole mass distribution. In typical experimental configurations, $\xi \ll 1$ holds, so that the gravitational torque can be described by a rapidly convergent series expansion.

The time-modulated Newtonian gravitational potential generated by the rotating mass distribution produces a periodic torque on the torsional degree of freedom. Due to the quadrupolar rotational symmetry, the torque contains predominantly even harmonics of the rotor rotation frequency. Among these components, the dominant contribution is the second harmonic at twice the rotation frequency, 2Ω , as expected from standard quadrupole symmetry arguments.

The amplitude of this 2Ω torque component is given by the multipole expansion

$$\tau_2 = \frac{GmM}{R_0} \left(\frac{3}{2}\xi^2 + \frac{35}{8}\xi^4 + \dots \right), \quad (12.28)$$

where G is the gravitational constant, m is the mass of a single rotor weight, and M denotes the effective mass at the end of the torsion bar. The quantities R_0 and ξ are the geometrical parameters defined in the previous section.

Equation (12.28) corresponds to the multipole expansion of the gravitational torque arising from the quadrupole moment. Because $\xi \ll 1$ in practical configurations, the series converges rapidly and the leading term dominates. To leading order, the torque amplitude scales as

$$\tau_2 \propto \frac{GmMa^2b^2}{R_0^5}. \quad (12.29)$$

This scaling relation shows explicitly that increasing the calibration mass m , the effective lever arm length a , or the rotor radius b enhances the torque amplitude, whereas

increasing the characteristic separation R_0 suppresses the coupling strongly through the R_0^{-5} dependence.

The angular response of the torsion bar is described by

$$I\ddot{\theta} + \Gamma\dot{\theta} + I\Omega_0^2\theta = \tau_2 \cos(2\Omega t), \quad (12.30)$$

which corresponds to the standard driven damped torsional oscillator [91]. Here I is the moment of inertia, Ω_0 is the torsional resonance angular frequency, and Γ is the damping coefficient. When the calibration band lies well above the torsional resonance ($\Omega \gg \Omega_0$), the inertial term dominates over the restoring term, and the angular displacement amplitude can be approximated as

$$\theta(\Omega) \simeq \frac{\tau_2}{I\Omega^2}. \quad (12.31)$$

To convert the torsional response into an effective interferometric strain, we combine the angular displacement of the torsion bar with the optical readout response of the interferometer. The strain-equivalent calibration amplitude induced by the GCal can then be written as

$$h_{\text{GCal}}(\Omega) \simeq -\frac{2\tau_2}{\eta_g |F_{\text{eff}}| I\Omega^2}, \quad (12.32)$$

where I is the moment of inertia of the torsion bar, η_g denotes the geometrical coupling efficiency, and F_{eff} represents the effective interferometer response function that converts angular displacement into the measured output signal. Equation (12.32) clearly shows that

$$h_{\text{GCal}} \propto \Omega^{-2}, \quad (12.33)$$

establishing a well-defined inverse-square frequency scaling. Consequently, the calibration-line amplitude increases toward lower frequencies, enabling intrinsically high-SNR calibration in the sub-Hz regime.

Sensitivity comparison

In this work, we have presented the first systematic formulation and experimental demonstration of a torque-coupled GCal for sub-Hz torsion-bar detectors. In contrast to conventional force-coupled GCals, which act primarily on translational degrees of

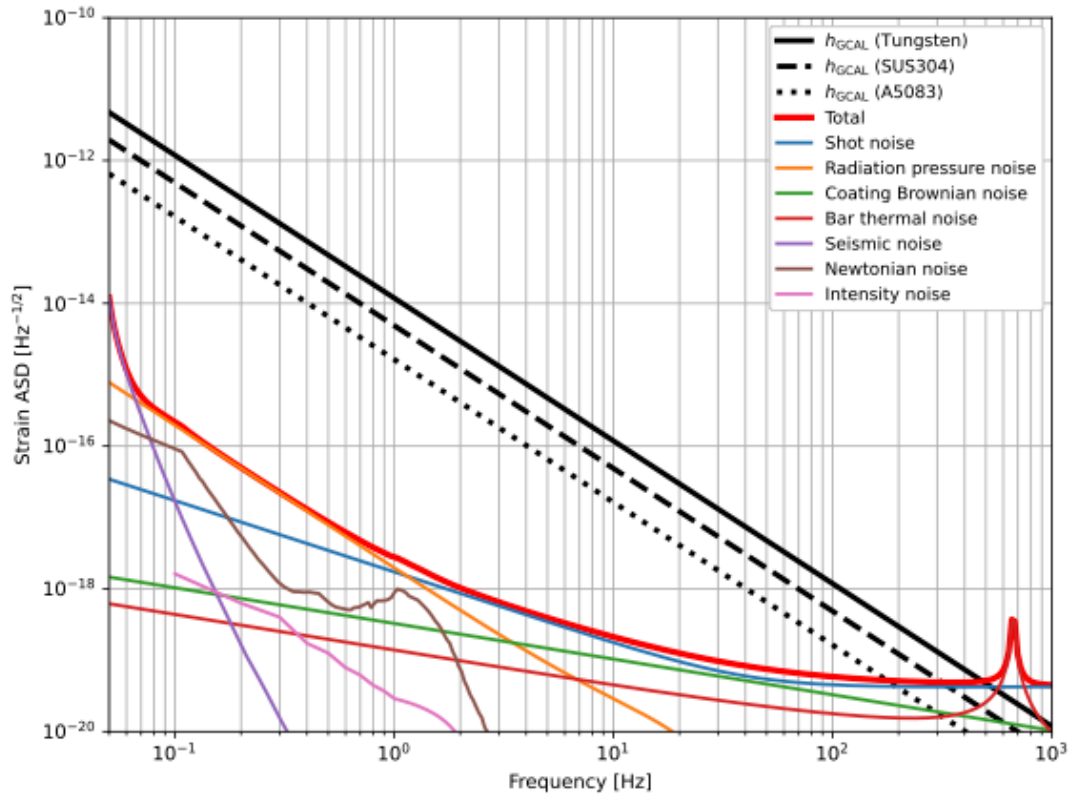


Figure 12.11: Noise budget of the CHRONOS compared with the strain-equivalent calibration amplitude h_{GCal} generated by the torque-coupled GCal. Results for different rotor materials (Tungsten, SUS304, and A5083) are shown.

freedom, the present approach couples the Newtonian gravitational field directly to the rotational degree of freedom of the test mass. This configuration significantly reduces dependence on the suspension transfer function and interferometer control loops, providing a conceptually simpler and more direct pathway for absolute calibration [62].

The gravitational interaction between the rotating quadrupole rotor and the torsion bar has been derived analytically using a multipole expansion. The resulting closed-form expression for the torque amplitude enables explicit evaluation of higher-order gravitational contributions as well as analytical computation of parameter derivatives. This framework allows systematic uncertainties to be propagated transparently, without relying on numerical potential-field integration.

Using parameters corresponding to the current CHRONOS design, the GCal signal

appears as a narrow spectral line at $2f_{\text{rot}}$ within the operational band of 0.1–10 Hz. Because the torsional resonance frequency satisfies

$$\frac{\omega_0}{2\pi} < 0.01 \text{ Hz},$$

the calibration band lies well within the inertial regime. As a result, a simple proportional relation between the applied gravitational torque and the strain-equivalent detector response is established, analogous to the free-mass calibration limit [91].

Since the gravitational torque scales linearly with the calibration mass, the achievable strain-equivalent amplitude and the corresponding SNR density are strongly determined by the rotor material density. For identical geometrical configurations, high-density materials provide a substantial increase in calibration margin, offering a clear design guideline for future implementations.

Systematic uncertainties were evaluated using a first-order perturbative error-propagation framework based on analytical parameter derivatives. The resulting fractional systematic error is approximately 0.24%, dominated primarily by geometric alignment uncertainties between the rotor and the detector. At 1 Hz, the corresponding absolute uncertainty is of order 10^{-17} , which defines the achievable absolute calibration accuracy under realistic experimental conditions.

Taken together, these results demonstrate that the torque-coupled GCal provides a practical and scalable calibration strategy for torsion-bar gravitational-wave detectors. The method combines a calibration-line amplitude well above the detector noise, analytically tractable systematic uncertainties, and reduced dependence on interferometer control models. More broadly, gravity-based calibration emerges as a powerful metrological tool for next-generation low-frequency gravitational-wave observatories.

12.5 Reconstruction

This section describes the strain-reconstruction pipelines for CHRONOS. In contrast to kilometer-scale Michelson interferometers where DARM is a differential arm length, the primary gravitational-wave readout of CHRONOS is the **difference bar angle**

(DARM $_{\theta}$),

$$\Delta\theta(t) \equiv \theta_1(t) - \theta_2(t), \quad (12.34)$$

which is reconstructed from the digital error signal and auxiliary control signals, following the standard control-model decomposition into sensing and actuation paths [4, 3, 116]. The present implementation is adapted to the torsional (angular) degree of freedom and to the speed-meter response characteristic of CHRONOS.

We develop two pipelines for reconstruction: (i) a **front-end (online)** pipeline for low-latency monitoring during operation, and (ii) a **high-latency (offline)** pipeline for the final calibrated strain product.

12.5.1 Front-end (online) pipeline

The front-end pipeline runs in real time and provides a continuously updated monitor signal $h_{\text{mon}}(t)$ with minimal latency. In this stage, the interferometer control-loop signals are partially calibrated online using a fixed set of IIR filters that approximate the nominal sensing and actuation models, as commonly implemented in low-latency calibration systems [103].

12.5.2 High-latency (offline) pipeline

The high-latency pipeline produces the final calibrated strain $h(t)$ using offline raw data and a more accurate reconstruction model. This pipeline adopts FIR filtering applied directly to the recorded error and control signals, consistent with standard offline calibration frameworks in ground-based detectors [116, 103].

The time dependence of the calibration parameters is incorporated using time-dependent correction factors (TDCFs) derived from swept-sine measurements and/or continuous calibration lines (e.g., photon calibrator, torque-coupled GCal, and reference injections).

In the frequency domain, the angular response function is written as

$$\tilde{R}_{\theta}(\Omega, t) = \frac{1}{\tilde{C}_{\theta}(\Omega, t)} + \tilde{D}_{\theta}(\Omega)\tilde{A}_{\theta}(\Omega, t), \quad (12.35)$$

and the reconstructed differential angle is

$$\Delta\tilde{\theta}(\Omega) = \tilde{R}_\theta(\Omega, t) \tilde{d}_{\text{err}}(\Omega). \quad (12.36)$$

In practice, the offline pipeline implements as a set of FIR filters for (i) inverse sensing and (ii) actuation reconstruction, together with slowly varying TDCFs (Time Dependent Collection Factor) that track drifts in optical gain, effective pole frequency, actuation efficiency, and timing.

12.6 Error estimation

Accurate estimation of the response function uncertainty is essential, because the strain reconstruction process involves both control-loop inversion and model-dependent angular-to-strain conversion [103, 116]. In CHRONOS, the primary observable is the differential bar angle $\Delta\theta$, and the strain is reconstructed through the angular response function $\tilde{R}_\theta(\Omega, t)$ and the angle-to-strain conversion factor $\mathcal{K}_{\theta \rightarrow h}$.

12.6.1 Residual response function

The detector response function $\tilde{R}_\theta(\Omega, t)$ is constructed from the sensing and actuation models introduced in the previous sections. In practice, however, the modeled response is not perfectly accurate because of uncertainties in optical parameters, control filters, and actuator calibration. Therefore, it is necessary to compare the model prediction with direct calibration measurements.

We quantify this discrepancy by defining the fractional residual response

$$\frac{\delta\tilde{R}_\theta(\Omega)}{\tilde{R}_{\theta,\text{model}}(\Omega)} = \frac{\tilde{R}_{\theta,\text{meas}}(\Omega) - \tilde{R}_{\theta,\text{model}}(\Omega)}{\tilde{R}_{\theta,\text{model}}(\Omega)}. \quad (12.37)$$

Here, $\tilde{R}_{\theta,\text{model}}(\Omega)$ is the response predicted from the calibrated sensing and actuation models, while $\tilde{R}_{\theta,\text{meas}}(\Omega)$ is obtained from calibration measurements such as swept-sine injections or continuous calibration lines using photon calibrators or torque-coupled GCal actuators [103, 62].

Because the reconstructed gravitational-wave strain is obtained by dividing the detector output by the response function, any error in the response model directly propagates to the strain estimate. To first order, the fractional response error is identical to the fractional strain error:

$$\frac{\delta \tilde{R}_\theta}{\tilde{R}_\theta} = \frac{\delta \tilde{h}}{\tilde{h}}. \quad (12.38)$$

Equation (12.38) indicates that both amplitude and phase uncertainties in the response function translate directly into calibration uncertainty in the reconstructed strain. Therefore, accurate measurement and continuous monitoring of $\tilde{R}_\theta(\Omega, t)$ across the observation band are essential to control systematic biases in astrophysical parameter estimation.

Cosmology

Primordial gravitational waves provide a unique observational window into the physics of the early Universe. Unlike electromagnetic radiation, gravitational waves propagate essentially freely once produced and therefore preserve direct information about the physical processes occurring at extremely high energy scales. The detection of primordial gravitational waves would therefore provide powerful insight into the origin of cosmic structure and the fundamental physics governing the earliest moments of the Universe.

One of the most compelling targets of modern cosmology is the gravitational-wave background generated during the inflationary epoch. Quantum fluctuations of the spacetime metric during inflation produce tensor perturbations that subsequently propagate as relic gravitational waves. The amplitude of these perturbations is commonly parameterized by the tensor-to-scalar ratio r , which quantifies the relative strength of tensor and scalar fluctuations.

The most sensitive probe of primordial tensor perturbations to date comes from observations of the cosmic microwave background (CMB). Primordial gravitational waves generate a characteristic B-mode polarization pattern in the CMB, providing a direct observable signature of tensor perturbations. Experiments such as *Planck* and BICEP/Keck have therefore placed increasingly stringent limits on the tensor amplitude at cosmological scales.

While CMB observations probe gravitational waves at extremely large cosmological scales, corresponding to frequencies near $f \sim 10^{-17}$ Hz, direct gravitational-wave detectors probe dramatically higher frequencies. Ground-based interferometers such as

LIGO and Virgo are sensitive to stochastic gravitational-wave backgrounds in the frequency band around tens to hundreds of hertz, while future space-based detectors will explore the millihertz band.

A key quantity describing the primordial tensor spectrum is the tensor spectral index n_t , which characterizes the scale dependence of the gravitational-wave amplitude. While many inflationary models predict a slightly red-tilted spectrum, a variety of early-Universe scenarios allow a positive tensor spectral index. Such a blue-tilted spectrum corresponds to a gravitational-wave energy density that increases toward higher frequencies.

Blue-tilted spectra are particularly interesting because the enhancement of gravitational-wave power at high frequencies can bring primordial signals within the sensitivity range of direct gravitational-wave detectors even when the tensor amplitude at CMB scales is small. This makes gravitational-wave observations across multiple frequency bands a powerful probe of early-Universe physics.

In this context, gravitational-wave detectors operating in the sub-Hz frequency band play a critical role. This frequency range bridges the gap between space-based and ground-based interferometers and provides a key window for probing blue-tilted primordial spectra. The CHRONOS experiment is designed to explore this frequency band with high sensitivity, enabling cosmological measurements that are complementary to both CMB observations and higher-frequency gravitational-wave detectors.

In this chapter we describe the cosmological framework used to connect primordial tensor perturbations with present-day gravitational-wave observations and investigate how multi-band measurements can constrain blue-tilted primordial gravitational-wave spectra.

13.1 Basic principle of the analysis

The stochastic gravitational-wave background (SGWB) provides a statistical probe of primordial gravitational waves generated in the early Universe. Unlike transient signals produced by individual astrophysical events, the primordial background is ex-

pected to consist of the superposition of a large number of independent sources and is therefore characterized statistically through its spectral energy density.

The gravitational-wave energy density per logarithmic frequency interval is commonly expressed in terms of the dimensionless quantity in Eq. 3.1.

Primordial gravitational waves produced during inflation are described by the tensor power spectrum

$$P_t(k) = A_t \left(\frac{k}{k_*} \right)^{n_t}, \quad (13.1)$$

where A_t is the tensor amplitude evaluated at the pivot scale k_* and n_t denotes the tensor spectral index. The pivot scale is typically chosen as

$$k_* \simeq 0.05 \text{ Mpc}^{-1},$$

which is commonly adopted in CMB analyses.

After their generation, primordial tensor perturbations propagate through the expanding Universe. Their evolution is described by the gravitational-wave transfer function $T(k)$, which accounts for the horizon re-entry of each mode and the expansion history of the Universe.

The present-day gravitational-wave energy density spectrum is related to the primordial tensor spectrum through

$$\Omega_{\text{GW}}(f) = \frac{1}{12} \left(\frac{k}{a_0 H_0} \right)^2 P_t(k) T^2(k), \quad (13.2)$$

where a_0 is the present scale factor.

The comoving wavenumber k is related to the observed gravitational-wave frequency through

$$k = 2\pi f a_0. \quad (13.3)$$

This relation provides the link between the primordial tensor spectrum defined at cosmological scales and the gravitational-wave energy density measured by interferometric detectors.

Measurements of $\Omega_{\text{GW}}(f)$ at interferometer frequencies therefore provide complementary information to CMB observations and enable constraints to be placed on the scale dependence of primordial tensor perturbations.

13.1.1 Transfer function in radiation- and matter-dominated eras

The transfer function $T(k)$ describes the evolution of primordial tensor perturbations after horizon re-entry and encodes the effect of the cosmological expansion history. In particular, the evolution differs depending on whether a given Fourier mode re-enters the horizon during the radiation-dominated (RD) or matter-dominated (MD) era.

Modes entering the horizon during the radiation-dominated epoch evolve differently from those entering during the matter-dominated epoch. This produces a scale-dependent modification of the primordial tensor spectrum that must be included when computing the present-day gravitational-wave energy density.

Using a commonly adopted analytic approximation, the present-day energy density of primordial gravitational waves can be written as

$$\Omega_{\text{GW}}(k) = \Omega_{\text{GW}}^{\text{CMB}} \left(\frac{k}{k_*} \right)^{n_t} T^2(k), \quad (13.4)$$

where the normalization at CMB scales is

$$\Omega_{\text{GW}}^{\text{CMB}} = \frac{3}{128} r A_s \Omega_r. \quad (13.5)$$

Here Ω_r denotes the present radiation density parameter and k_* is the pivot scale used in CMB analyses.

The transfer function can be approximated by combining the contributions from the

radiation- and matter-dominated epochs,

$$T^2(k) = T_{\text{MD}}^2(k) + T_{\text{RD}}^2. \quad (13.6)$$

For modes that re-enter the horizon during the matter-dominated era, the transfer function scales as

$$T_{\text{MD}}^2(k) = \frac{1}{2} \left(\frac{k_{\text{eq}}}{k} \right)^2, \quad (13.7)$$

where k_{eq} is the comoving horizon scale at matter-radiation equality.

For modes entering during the radiation-dominated era, the transfer function approaches a constant value,

$$T_{\text{RD}}^2 = \frac{16}{9}. \quad (13.8)$$

Combining these contributions yields the approximate expression

$$\Omega_{\text{GW}}(k) = \Omega_{\text{GW}}^{\text{CMB}} \left(\frac{k}{k_*} \right)^{n_t} \left[\frac{1}{2} \left(\frac{k_{\text{eq}}}{k} \right)^2 + \frac{16}{9} \right]. \quad (13.9)$$

This analytic expression provides a convenient model for the primordial gravitational-wave spectrum over a wide range of frequencies and is widely used in studies of multi-band gravitational-wave cosmology.

13.2 Cosmological model and assumptions

The cosmological analysis presented in this work is performed within the framework of the standard Λ CDM cosmology extended to include primordial tensor perturbations.

The parameter set used in the analysis is

$$\Theta = \{\Omega_b, \Omega_c, h, \tau, n_s, A_s, r, n_t\}, \quad (13.10)$$

where Ω_b and Ω_c denote the present baryon and cold dark-matter density parameters, h is the dimensionless Hubble parameter defined by

$$H_0 = 100 h \text{ km s}^{-1} \text{ Mpc}^{-1},$$

and τ is the optical depth to reionization.

The scalar perturbations are characterized by the spectral index n_s and the amplitude A_s of the primordial curvature power spectrum.

The tensor sector is described by the tensor-to-scalar ratio r and the tensor spectral index n_t . The amplitude of the primordial tensor spectrum is related to the scalar amplitude through

$$A_t = r A_s. \tag{13.11}$$

In the simplest slow-roll inflation models the tensor spectral index satisfies the consistency relation $n_t = -r/8$. In this work, however, we do not impose this relation and instead treat n_t as an independent free parameter. This allows us to explore a wider class of early-Universe scenarios and to test both red-tilted ($n_t < 0$) and blue-tilted ($n_t > 0$) tensor spectra.

13.2.1 Blue-tilted tensor spectrum

While many slow-roll inflation models predict a slightly red-tilted tensor spectrum, a variety of early-Universe scenarios allow a positive tensor spectral index ($n_t > 0$). Examples include inflationary models with nonstandard dynamics, non-Bunch-Davies initial states, particle production during inflation, and alternative early-Universe scenarios such as ekpyrotic cosmology (see, e.g., Refs. [97, 32, 33]).

A positive tensor spectral index implies that the gravitational-wave energy density increases toward higher frequencies. Consequently, even a small tensor amplitude at cosmological scales can produce an enhanced signal in the frequency range probed by direct gravitational-wave detectors.

This property makes blue-tilted tensor spectra particularly well suited to tests using multi-band gravitational-wave observations. By combining measurements from CMB experiments and direct gravitational-wave detectors, it becomes possible to constrain the spectral tilt of primordial tensor perturbations across many orders of magnitude in scale.

In this work we therefore treat n_t as a free parameter and investigate the resulting constraints obtained from the combined analysis of CMB data and gravitational-wave observations.

13.3 Observables

Primordial tensor perturbations leave observable signatures both in the cosmic microwave background (CMB) and in the present-day stochastic gravitational-wave background.

In CMB observations, tensor modes manifest themselves primarily through the B-mode polarization generated by gravitational waves at the time of recombination. These measurements constrain the amplitude of primordial tensor perturbations at large cosmological scales and are commonly expressed in terms of the tensor-to-scalar ratio r .

In contrast, direct gravitational-wave detectors probe the present-day gravitational-wave energy density spectrum $\Omega_{\text{GW}}(f)$ at much higher frequencies. The strain sensitivity of interferometric detectors therefore translates into constraints on the stochastic gravitational-wave background.

The relation between the comoving wavenumber and the observed gravitational-wave frequency is

$$k = 2\pi f a_0, \tag{13.12}$$

which connects the primordial tensor spectrum defined at cosmological scales to the gravitational-wave energy density measured by interferometric detectors.

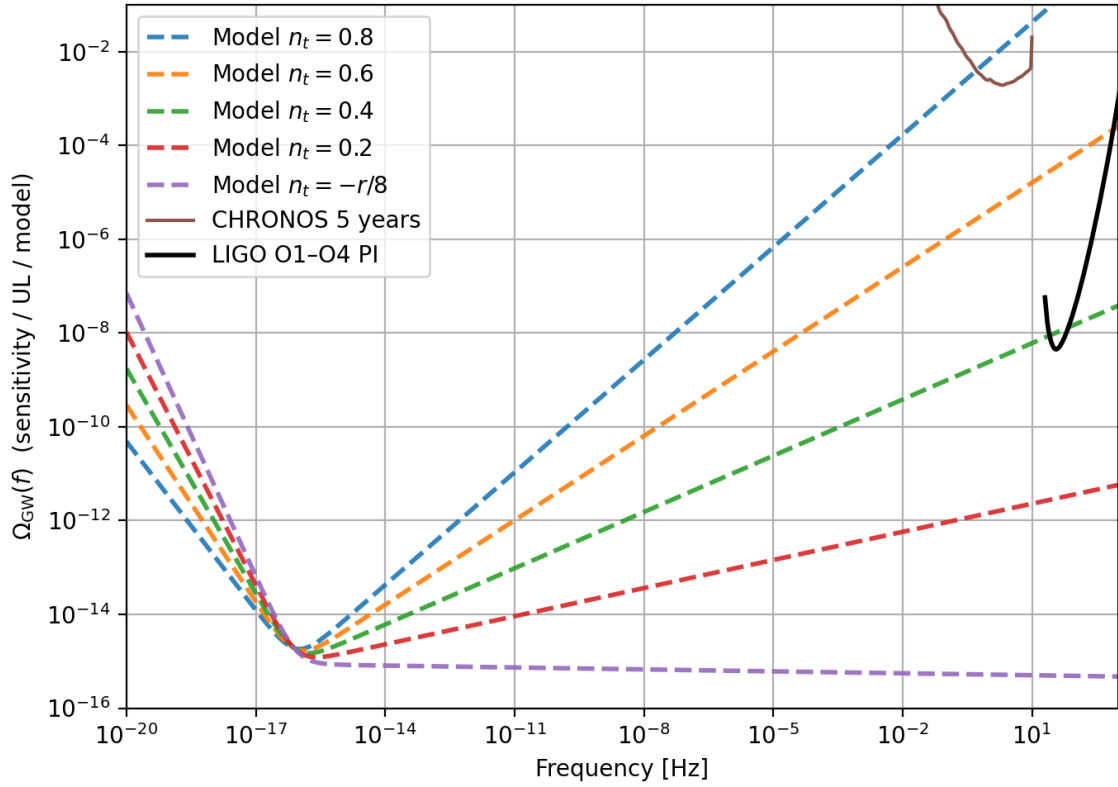


Figure 13.1: Predicted primordial gravitational-wave spectra together with observational constraints across multiple frequency bands. The shaded regions represent the posterior distributions obtained from the cosmological analysis. Combining measurements of the stochastic gravitational-wave background across different experiments enables strong constraints to be placed on the tensor spectral index (n_t) and the amplitude of primordial tensor perturbations.

By combining CMB measurements of the tensor amplitude with constraints on the stochastic gravitational-wave background at interferometer frequencies, it becomes possible to probe the scale dependence of primordial tensor perturbations across a very wide range of scales.

Figure 13.1 illustrates the predicted primordial gravitational-wave spectra together with the observational constraints considered in this work.

13.3.1 Bayesian framework and data combination

The cosmological parameters are inferred within a Bayesian statistical framework. For a given observational data set D and a set of cosmological parameters Θ , the likelihood function is defined as

$$\mathcal{L}(D|\Theta). \quad (13.13)$$

The posterior probability distribution of the parameters is obtained using Bayes' theorem,

$$P(\Theta|D) \propto \mathcal{L}(D|\Theta) P(\Theta), \quad (13.14)$$

where $P(\Theta)$ denotes the prior distribution of the model parameters.

In this work we combine two classes of observational data: measurements of the cosmic microwave background (CMB) and constraints on the stochastic gravitational-wave background obtained from direct gravitational-wave experiments. Assuming that the two data sets are statistically independent, the total likelihood can be written as

$$\mathcal{L}_{\text{total}} = \mathcal{L}_{\text{CMB}} \mathcal{L}_{\text{GW}}. \quad (13.15)$$

The CMB likelihood \mathcal{L}_{CMB} is evaluated using publicly available likelihood packages for the *Planck* 2018 temperature and polarization data together with the BICEP/Keck B-mode measurements. These data primarily constrain the tensor-to-scalar ratio r , which probes primordial gravitational waves at cosmological scales.

The second component of the likelihood, \mathcal{L}_{GW} , incorporates observational constraints on the stochastic gravitational-wave background measured by interferometric detectors. These measurements probe the present-day gravitational-wave energy density spectrum $\Omega_{\text{GW}}(f)$ at interferometer frequencies.

13.3.2 Sensitivity and statistical uncertainty

The estimation of the stochastic gravitational-wave background is performed in the frequency domain using Fourier-transformed strain data. For a finite observation time T , the fundamental frequency resolution is

$$\Delta f_{\text{FFT}} = \frac{1}{T}. \quad (13.16)$$

To obtain statistically meaningful measurements, the Fourier samples are averaged within frequency bins of width Δf_{bin} centered at frequency f_i . Using the two-sided Fourier convention adopted here, the number of statistically independent Fourier modes contained in a given bin is

$$N_{\text{mode},i} = 2T \Delta f_{\text{bin},i}. \quad (13.17)$$

Using the relation between the strain spectrum and the gravitational-wave energy density, the estimator of the energy density in the i -th bin can be written as

$$\hat{\Omega}_{\text{GW}}(f_i) = \frac{2\pi^2}{3H_0^2} f_i^3 \hat{S}_h(f_i). \quad (13.18)$$

Assuming stationary Gaussian noise, the variance of the strain spectral density estimator is

$$\text{Var}[\hat{S}_h(f_i)] = \frac{S_h(f_i)^2}{N_{\text{mode},i}}. \quad (13.19)$$

The variance of the gravitational-wave energy density estimator therefore becomes

$$\text{Var}[\hat{\Omega}_{\text{GW}}(f_i)] = \left(\frac{2\pi^2}{3H_0^2} f_i^3 \right)^2 \frac{S_h(f_i)^2}{N_{\text{mode},i}}. \quad (13.20)$$

Introducing the sensitivity curve

$$\Omega_{\text{sens}}(f) = \frac{2\pi^2}{3H_0^2} f^3 S_h(f), \quad (13.21)$$

the variance can be written as

$$\sigma_i^2 = \frac{\Omega_{\text{sens}}(f_i)^2}{2T \Delta f_{\text{bin},i}}. \quad (13.22)$$

The corresponding statistical uncertainty is

$$\sigma_i = \frac{\Omega_{\text{sens}}(f_i)}{\sqrt{2T \Delta f_{\text{bin},i}}}. \quad (13.23)$$

These expressions show that the statistical uncertainty is reduced by increasing either the observation time T or the effective bandwidth $\Delta f_{\text{bin},i}$ over which independent Fourier modes are averaged.

13.3.3 Likelihood for stochastic gravitational-wave constraints

The stochastic gravitational-wave spectrum is represented by estimators

$$\hat{\Omega}_{\text{GW}}(f_i), \quad (13.24)$$

with statistical uncertainties σ_i .

For a given cosmological parameter set Θ , the theoretical prediction is

$$\Omega_{\text{GW}}^{\text{th}}(f_i; \Theta). \quad (13.25)$$

Assuming independent Gaussian errors in each frequency bin, the likelihood for the gravitational-wave data is

$$\mathcal{L}_{\text{GW}} = \prod_i \frac{1}{\sqrt{2\pi}\sigma_i} \exp \left[-\frac{(\hat{\Omega}_{\text{GW}}(f_i) - \Omega_{\text{GW}}^{\text{th}}(f_i; \Theta))^2}{2\sigma_i^2} \right]. \quad (13.26)$$

Equivalently,

$$\chi^2 = \sum_i \frac{[\hat{\Omega}_{\text{GW}}(f_i) - \Omega_{\text{GW}}^{\text{th}}(f_i; \Theta)]^2}{\sigma_i^2}, \quad (13.27)$$

such that

$$\mathcal{L}_{\text{GW}} \propto \exp\left(-\frac{\chi^2}{2}\right). \quad (13.28)$$

In the absence of a significant detection, $\hat{\Omega}_{\text{GW}}(f_i) \simeq 0$, leading to

$$\chi^2 = \sum_i \frac{\Omega_{\text{GW}}^{\text{th}}(f_i; \Theta)^2}{\sigma_i^2}. \quad (13.29)$$

13.3.4 Parameter inference

The cosmological parameters are inferred using a Bayesian parameter estimation framework. Given the observational data D and the model parameters Θ , the posterior probability distribution is obtained from Bayes' theorem,

$$P(\Theta|D) \propto \mathcal{L}_{\text{total}}(D|\Theta) P(\Theta), \quad (13.30)$$

where $\mathcal{L}_{\text{total}}$ is the total likelihood defined in Sec. 13.3.3 and $P(\Theta)$ denotes the prior distribution of the model parameters.

The posterior distribution is explored using a Markov Chain Monte Carlo (MCMC) sampling method. In this work we employ the publicly available inference framework `Cobaya`, which interfaces with the Boltzmann solver `CLASS` to compute the cosmological observables for each point in parameter space.

For each proposed parameter set Θ , the predicted gravitational-wave energy density spectrum $\Omega_{\text{GW}}^{\text{th}}(f)$ is evaluated and compared with the observational constraints through the likelihood function described in Sec. 13.3.3. The CMB likelihood is evaluated simultaneously, allowing the primordial tensor parameters to be constrained using both cosmological and gravitational-wave observations.

Convergence of the MCMC chains is assessed using the Gelman–Rubin statistic. The

sampling is considered converged once the condition

$$R - 1 < 0.01 \tag{13.31}$$

is satisfied for all sampled parameters.

13.4 Conclusion

Primordial gravitational waves provide a unique probe of the physical processes that occurred in the earliest moments of the Universe. Their spectrum encodes information about the dynamics of inflation and other possible mechanisms of gravitational-wave generation in the early Universe.

In this chapter we have investigated cosmological constraints on primordial gravitational waves using a multi-band observational approach that combines cosmic microwave background (CMB) measurements with constraints on the stochastic gravitational-wave background from direct gravitational-wave experiments.

While CMB observations probe tensor perturbations at extremely large cosmological scales, gravitational-wave detectors provide complementary sensitivity at much higher frequencies. Combining these observations therefore allows the primordial tensor spectrum to be tested across an exceptionally wide range of scales.

Particular attention has been given to blue-tilted tensor spectra characterized by a positive tensor spectral index ($n_t > 0$). Such spectra arise in a variety of early-Universe scenarios and can produce enhanced gravitational-wave signals at interferometer frequencies.

Future gravitational-wave detectors operating in the sub-Hz to Hz frequency range will play a particularly important role in this program. Experiments such as CHRONOS will explore a frequency band that bridges the gap between space-based and ground-based detectors, providing a key window for probing blue-tilted primordial spectra.

The combination of cosmological observations and gravitational-wave experiments therefore opens a new observational window onto the physics of the early Universe.

By probing the primordial tensor spectrum over an unprecedented range of scales, future observations have the potential to reveal new insights into the origin of cosmic structure and the fundamental physics governing the earliest stages of cosmic history.

Summary

The CHRONOS initiative — the Cryogenic sub-Hz cROss torsion-bar detector with quantum Non-demolition Speed meter — represents a systematic effort to establish a cryogenic, precision interferometric platform operating in the sub-Hz frequency regime.

This White Paper has presented the CHRONOS Science Program as a coherent roadmap integrating scientific objectives, technical development, and phased implementation milestones. Sensitivity projections, instrument architecture, interferometer control strategies, input optics design, cryogenic technologies, data analysis methodologies, and calibration frameworks have been described as interconnected components of a unified system.

The CHRONOS Collaboration has been structured to ensure that all implementation activities remain traceable to the defined scientific objectives. Subsystem-based responsibility allocation guarantees clarity of accountability, while the three-tier governance model provides operational agility, strategic coherence, and executive oversight. The annual CHRONOS International Workshop enables systematic scientific review and alignment, while the Management Meeting ensures disciplined decision-making and resource allocation.

A formal revision policy distinguishes between minor technical updates and major strategic modifications of the White Paper. Transparent publication practices, opt-in authorship principles, and public dissemination through the CHRONOS website reinforce international visibility and scientific integrity. Structured membership and compliance procedures provide a stable yet expandable framework for future multi-

national collaboration.

Through this integrated scientific and organizational approach, CHRONOS establishes a scalable foundation for advancing cryogenic interferometry and quantum measurement technologies in the sub-Hz regime. The framework presented here enables both immediate implementation and long-term international growth, positioning CHRONOS as a robust platform for next-generation precision measurement research.

Bibliography

- [1] J. Aasi and others (LIGO Scientific Collaboration). Advanced ligo. *Class. Quantum Grav.*, 32:074001, 2015.
- [2] Junaid Aasi, Joan Abadie, BP Abbott, Richard Abbott, TD Abbott, MR Abernathy, Carl Adams, Thomas Adams, Paolo Addesso, RX Adhikari, et al. Enhanced sensitivity of the ligo gravitational wave detector by using squeezed states of light. *Nature Photonics*, 7(8):613–619, 2013.
- [3] J. Abadie et al. Calibration of the ligo gravitational wave detectors in the fifth science run. *Nucl. Instrum. Methods Phys. Res. A*, 624:223–240, 2010.
- [4] B. P. Abbott et al. Ligo: the laser interferometer gravitational-wave observatory. *Rep. Prog. Phys.*, 72:076901, 2009.
- [5] B. P. Abbott et al. Observation of gravitational waves from a binary black hole merger. *Phys. Rev. Lett.*, 116:061102, 2016.
- [6] R. Abbott et al. Open data from the first and second observing runs of advanced ligo and advanced virgo. *Living Reviews in Relativity*, 24:1, 2021.
- [7] R. Abbott et al. Upper limits on the isotropic stochastic gravitational-wave background. *Physical Review D*, 104:022004, 2021.
- [8] F. Acernese et al. Advanced virgo: a second-generation interferometric gravitational wave detector. *Classical and Quantum Gravity*, 32:024001, 2015.
- [9] Rana X. Adhikari. Gravitational radiation detection with laser interferometry. *Rev. Mod. Phys.*, 86:121–151, 2014.

- [10] Rana X. Adhikari et al. A cryogenic silicon interferometer for gravitational-wave detection. *Class. Quantum Grav.*, 34:044001, 2017.
- [11] T. Akutsu et al. Overview of kagra. *Prog. Theor. Exp. Phys.*, 2021:05A101, 2021.
- [12] T. Akutsu and others (KAGRA Collaboration). Kagra: 2.5 generation interferometric gravitational wave detector. *Nature Astronomy*, 3:35–40, 2019.
- [13] K. F. Albertin et al. Study of pecvd SiO_xN_y films dielectric properties with different nitrogen concentration utilizing mos capacitors. *Microelectronic Engineering*, 77(2):144–149, 2005.
- [14] B. Allen and J. D. Romano. Detecting a stochastic background of gravitational radiation. *Physical Review D*, 59:102001, 1999.
- [15] P. Amaro-Seoane et al. Laser interferometer space antenna. *arXiv:1702.00786*, 2017.
- [16] M. Ando et al. Torsion-bar antenna for low-frequency gravitational-wave detection. *Phys. Rev. Lett.*, 105:161101, 2010.
- [17] Stuart M. Aston et al. Update on quadruple suspension design for advanced ligo. *Classical and Quantum Gravity*, 29:235004, 2012.
- [18] Eric D. Black. An introduction to pound–drever–hall laser frequency stabilization. *American Journal of Physics*, 69(1):79–87, 2001.
- [19] V. B. Braginsky and F. Ya. Khalili. *Quantum Measurement*. Cambridge University Press, 1992.
- [20] A. Buonanno and Y. Chen. Quantum noise in second generation gravitational-wave interferometers. *Physical Review D*, 64:042006, 2001.
- [21] Alessandra Buonanno and Yanbei Chen. Quantum noise in second generation, signal-recycled laser interferometric gravitational-wave detectors. *Phys. Rev. D*, 64:042006, 2001.
- [22] H. B. Callen and T. A. Welton. Irreversibility and generalized noise. *Phys. Rev.*, 83:34–40, 1951.

- [23] E. Capote et al. Advanced LIGO detector performance in the fourth observing run. *Phys. Rev. D*, 111:062002, 2025.
- [24] C. Caprini and D. G. Figueroa. Cosmological backgrounds of gravitational waves. *Classical and Quantum Gravity*, 35:163001, 2018.
- [25] C. M. Caves. Quantum limits on noise in linear amplifiers. *Reviews of Modern Physics*, 52:341, 1980.
- [26] C. M. Caves. Quantum-mechanical noise in an interferometer. *Physical Review D*, 23:1693, 1981.
- [27] Y. Chen. Sagnac interferometer as a speed-meter-type, quantum-nondemolition gravitational-wave detector. *Phys. Rev. D*, 67:122004, 2003.
- [28] N. Christensen. Measuring the stochastic gravitational radiation background with laser interferometric antennas. *Phys. Rev. D*, 46:5250, 1992.
- [29] F. Cleva et al. Laser power stabilization for advanced virgo. *CLEO/Europe-EQEC*, pages 1–1, 2021.
- [30] G. D. Cole et al. Tenfold reduction of brownian noise in high-reflectivity optical coatings. *Nature Photonics*, 7:644–650, 2013.
- [31] COMSOL, Inc. COMSOL Software Version 5.4 Release Highlights, 2025. <https://www.comsol.com/release/5.4>.
- [32] C. R. Contaldi. Anisotropies of gravitational wave backgrounds: a line of sight approach. *Physical Review D*, 76:104016, 2007.
- [33] J. L. Cook, E. Dimastrogiovanni, D. A. Easson, and L. M. Krauss. Reheating predictions in single field inflation. *Journal of Cosmology and Astroparticle Physics*, 2015:047, 2015.
- [34] M. Coughlin et al. Subtraction of newtonian noise using optimized sensor arrays. *Class. Quantum Grav.*, 31:215003, 2014.
- [35] S. L. Danilishin and F. Ya. Khalili. Quantum measurement theory in gravitational-wave detectors. *Living Rev. Relativity*, 15:5, 2012.

- [36] R. W. P. Drever, J. L. Hall, F. V. Kowalski, J. Hough, G. M. Ford, A. J. Munley, and H. Ward. Laser phase and frequency stabilization using an optical resonator. *Applied Physics B*, 31:97–105, 1983.
- [37] D Estevez, P Lagabbe, A Masserot, et al. The Advanced Virgo photon calibrators. *Classical and Quantum Gravity*, 38(7):075007, February 2021.
- [38] Matthew Evans et al. Observation of parametric instability in advanced ligo. *Physical Review Letters*, 114:161102, 2015.
- [39] L. S. Finn. Detection, measurement, and gravitational radiation. *Physical Review D*, 46:5236, 1992.
- [40] Robert L. Forward. Wideband laser-interferometer gravitational-radiation experiment. *Phys. Rev. D*, 17(2):379–390, 1978.
- [41] Gene F. Franklin, J. David Powell, and Abbas Emami-Naeini. *Feedback Control of Dynamic Systems*. Pearson, 2015.
- [42] A. Freise et al. Frequency-domain interferometer simulation with higher-order spatial modes. *Classical and Quantum Gravity*, 27:084003, 2010.
- [43] T. T. Fricke et al. Dc readout experiment in enhanced ligo. *Classical and Quantum Gravity*, 29:065005, 2012.
- [44] Peter Fritschel. Output mode cleaner design. Technical report, LIGO-T040018-00-D, 2004.
- [45] J. G. E. Gardeniers et al. Lpcvd silicon-rich silicon nitride films for applications in micromechanics, studied with statistical experimental design. *Journal of Vacuum Science & Technology A*, 14:2879–2892, 1996.
- [46] P. W. Graham et al. New method for gravitational wave detection with atomic sensors. *Physical Review Letters*, 110:171102, 2013.
- [47] J. E. Greene et al. Intermediate-mass black holes. *Annual Review of Astronomy and Astrophysics*, 58:257–312, 2020.
- [48] H. Grote et al. First long-term application of squeezed states of light in a gravitational-wave observatory. *Physical Review Letters*, 110:181101, 2013.

- [49] D. H. Gwo. Ultra-precision bonding for cryogenic fused silica optics. *Proceedings of SPIE*, 4448:148–155, 2001.
- [50] Jan Harms. Terrestrial gravity fluctuations. *Living Rev. Relativ.*, 18:3, 2015.
- [51] G. M. Harry et al. Thermal noise in interferometric gravitational wave detectors due to dielectric optical coatings. *Class. Quantum Grav.*, 19:897–917, 2002.
- [52] G. M. Harry et al. Titania-doped tantala/silica coatings for gravitational-wave detection. *Class. Quantum Grav.*, 24:405–415, 2007.
- [53] Joscha Heinze, Karsten Danzmann, Benno Willke, and Henning Vahlbruch. 10 db quantum-enhanced michelson interferometer with balanced homodyne detection. *Physical Review Letters*, 129(3):031101, 2022.
- [54] Tianqi Hong et al. Brownian thermal noise in multilayer coated mirrors. *Phys. Rev. D*, 87:082001, 2013.
- [55] Paul Horowitz and Winfield Hill. *The Art of Electronics*. Cambridge University Press, 2015.
- [56] Y. Inoue et al. Development of advanced photon calibrator for Kamioka gravitational wave detector (KAGRA). *Rev. Sci. Instrum.*, 94(7):074502, 2023.
- [57] Yuki Inoue et al. Chronos: Cryogenic sub-hz cross torsion bar detector with quantum non-demolition speed meter. 2025.
- [58] Yuki Inoue et al. Optical design and sensitivity optimization of cryogenic sub-hz cross torsion bar detector with quantum non-demolition speed meter (chronos). 2026.
- [59] Yuki Inoue, Sadakazu Haino, Nobuyuki Kanda, Yujiro Ogawa, Toshikazu Suzuki, Takayuki Tomaru, Takahiro Yamanmoto, and Takaaki Yokozawa. Improving the absolute accuracy of the gravitational wave detectors by combining the photon pressure and gravity field calibrators. *Phys. Rev. D*, 98:022005, Jul 2018.
- [60] Yuki Inoue, Daiki Tanabe, and Vivek Kumar. Improving calibration accuracy with torque coupled gravity field calibrator for sub-hz gravitational wave observation in chronos. 2026.

- [61] M. Kamionkowski and E. D. Kovetz. The quest for b modes from inflationary gravitational waves. *Annual Review of Astronomy and Astrophysics*, 54:227–269, 2016.
- [62] S. Karki et al. The advanced ligo photon calibrators. *Rev. Sci. Instrum.*, 87:114503, 2016.
- [63] W. Kern and R. S. Rosler. *Thin Film Processes II*. Academic Press, New York, 1990.
- [64] F. Ya. Khalili. Quantum variational measurement in gravitational-wave detectors. *Physical Review D*, 66:102003, 2002.
- [65] K. S. Kim et al. Deposition of very-low-hydrogen-containing silicon at a low temperature using very-high-frequency (162 mhz) sih_4 plasma. *Micromachines*, 13:173, 2022.
- [66] H. J. Kimble, Y. Levin, A. B. Matsko, K. S. Thorne, and S. P. Vyatchanin. Conversion of conventional gravitational-wave interferometers into quantum nondemolition interferometers. *Phys. Rev. D*, 65:022002, 2001.
- [67] H. Kogelnik and T. Li. Laser beams and resonators. *Applied Optics*, 5:1550–1567, 1966.
- [68] Ayaka Kumeta, Charlotte Bond, and Kentaro Somiya. Design study of the kagra output mode cleaner. *Optical Review*, 22(1):149–152, 2015.
- [69] Patrick Kwee and B. Willke. Automatic laser beam alignment for gravitational wave detectors. *Applied Optics*, 51(26):6029–6039, 2012.
- [70] Lake Shore Cryotronics. Silicon diode temperature sensors dt-680 series, 2023. Technical documentation.
- [71] Yuri Levin. Internal thermal noise in the ligo test masses: A direct approach. *Phys. Rev. D*, 57:659–663, 1998.
- [72] K. Luke et al. Overcoming si_3n_4 film stress limitations. *Optics Express*, 21:22829–22833, 2013.
- [73] M. Maggiore. Gravitational wave experiments and early universe cosmology. *Physics Reports*, 331:283–367, 2000.

- [74] Michele Maggiore. *Gravitational Waves, Volume 1: Theory and Experiments*. Oxford University Press, 2008.
- [75] D. J. McManus, , et al. Mechanical newtonian noise cancellation for gravitational wave detectors. *Phys. Rev. Lett.*, 118(23):231101, 2017.
- [76] B. J. Meers. Recycling in laser-interferometric gravitational-wave detectors. *Physical Review D*, 38:2317–2326, 1988.
- [77] M. C. Miller and E. J. M. Colbert. Intermediate-mass black holes. *International Journal of Modern Physics D*, 13:1–64, 2004.
- [78] J. Mizuno. Comparison of optical configurations for laser-interferometric gravitational-wave detectors. *Physics Letters A*, 175:273–276, 1993.
- [79] J.P. Montagner et al. Prompt gravity signal induced by the 2011 tohoku-oki earthquake. *Nature Communications*, 7:13349, 2016.
- [80] M. Ozawa. Universally valid reformulation of the heisenberg uncertainty principle. *Physical Review A*, 67:042105, 2003.
- [81] M. Ozawa. Uncertainty relations for noise and disturbance. *Annals of Physics*, 311:350, 2004.
- [82] H. R. Philipp. Optical properties of silicon oxynitride films. *Journal of The Electrochemical Society*, 120:295, 1973.
- [83] Frank Pobell. *Matter and Methods at Low Temperatures*. Springer, 2007.
- [84] M. Punturo et al. The einstein telescope: A third-generation gravitational wave observatory. *Class. Quantum Grav.*, 27:194002, 2010.
- [85] P. Purdue and Y. Chen. Practical speed-meter designs for quantum nondemolition interferometers. *Physical Review Letters*, 89:231101, 2002.
- [86] D. Reitze et al. Cosmic explorer: The u.s. contribution to gravitational-wave astronomy beyond ligo. *Bulletin of the AAS*, 51:035, 2019.
- [87] J. D. Romano and N. J. Cornish. Detection methods for stochastic gravitational-wave backgrounds. *Living Rev. Relativity*, 20:2, 2017.

- [88] S. Rowan et al. Q-factor measurements of hydroxy-catalysis bonds. *Physics Letters A*, 246:471–478, 1998.
- [89] S. Rowan et al. Thermal noise and material issues for gravitational wave detectors. *Classical and Quantum Gravity*, 22:S183–S190, 2005.
- [90] Peter R. Saulson. Terrestrial gravitational noise on a gravitational wave antenna. *Phys. Rev. D*, 30:732–736, 1984.
- [91] Peter R. Saulson. Thermal noise in mechanical experiments. *Phys. Rev. D*, 42:2437–2445, 1990.
- [92] Peter R. Saulson. *Fundamentals of Interferometric Gravitational Wave Detectors*. World Scientific, 1994.
- [93] R. Schnabel et al. Building blocks for future gravitational wave detectors. *Nature Communications*, 1:121, 2010.
- [94] A. Sesana. Systematic investigation of the expected gravitational wave signal from supermassive black hole binaries. *Monthly Notices of the Royal Astronomical Society*, 433:L1–L5, 2013.
- [95] A. Sesana. Prospects for multi-band gravitational-wave astronomy. *Physical Review Letters*, 116:231102, 2016.
- [96] A. E. Siegman. *Lasers*. University Science Books, 1986.
- [97] T. L. Smith, M. Kamionkowski, and A. Cooray. Direct detection of the inflationary gravitational wave background. *Physical Review D*, 73:023504, 2006.
- [98] K. Somiya et al. Frequency noise and intensity noise of next-generation gravitational-wave detectors with RF/DC readout schemes. *Phys. Rev. D*, 73:122005, 2006.
- [99] M S Stefszky, C M Mow-Lowry, S S Y Chua, D A Shaddock, B C Buchler, H Vahlbruch, A Khalaidovski, R Schnabel, P K Lam, and D E McClelland. Balanced homodyne detection of optical quantum states at audio-band frequencies and below. *Classical and Quantum Gravity*, 29(14):145015, jun 2012.

- [100] J. Steinlechner. Optical coating research for gravitational-wave detectors. *Living Rev. Relativ.*, 21:4, 2018.
- [101] Sebastian Steinlechner, Bryan W Barr, Angus S Bell, Stefan L Danilishin, Andreas Gläfke, Christian Gräf, Jan-Simon Hennig, E Alasdair Houston, Sabina H Huttner, Sean S Leavey, et al. Local-oscillator noise coupling in balanced homodyne readout for advanced gravitational wave detectors. *Physical Review D*, 92(7):072009, 2015.
- [102] R. A. Street. *Hydrogenated Amorphous Silicon*. Cambridge University Press, Cambridge, 1991.
- [103] L. Sun et al. Characterization of systematic error in advanced ligo calibration. *Class. Quantum Grav.*, 37:225008, 2020.
- [104] Daiki Tanabe, Yuki Inoue, Vivek Kumar, Miftahul Ma'arif, and T. C. Yu. Torque cancellation effect of intensity noise for cryogenic sub-hz cross torsion bar detector with quantum non-demolition speed meter (chronos). 2025.
- [105] Tanabe, D. and others. Photon-pressure actuator design for torsion-bar-based gravitational wave detector, 2026. In preparation.
- [106] E. Thrane and C. Talbot. An introduction to bayesian inference in gravitational-wave astronomy. *Publications of the Astronomical Society of Australia*, 36:e010, 2019.
- [107] Kenji Tsuji, Tomohiro Ishikawa, Kentaro Komori, Yutaro Enomoto, Yuta Michimura, Kurumi Umemura, Shoki Iwaguchi, Keiko Kokeyama, and Seiji Kawamura. Quantum noise reduction in the space-based gravitational wave antenna decigo using optical springs and homodyne detection scheme. *arXiv preprint arXiv:2509.17372*, 2025.
- [108] Kenji Uchino. *Piezoelectric Actuators and Ultrasonic Motors*. Springer, 1997.
- [109] S. A. Usman et al. The pycbc search for gravitational waves from compact binary coalescence. *Class. Quantum Grav.*, 33:215004, 2016.
- [110] H. Vahlbruch et al. Observation of squeezed light with 10-db quantum-noise reduction. *Physical Review Letters*, 100:033602, 2008.

- [111] M. Vallée et al. Observations and modeling of prompt gravity signals from earthquakes. *Science Advances*, 3:e1700606, 2017.
- [112] J. Veitch et al. Parameter estimation for compact binaries with ground-based gravitational-wave observations. *Phys. Rev. D*, 91:042003, 2015.
- [113] S. S. Verbridge et al. High quality factor resonance at room temperature. *Journal of Applied Physics*, 99:124304, 2006.
- [114] A. D. Viets et al. Reconstructing the calibrated strain signal in the advanced ligo detectors. *Class. Quantum Grav.*, 35:095015, 2018.
- [115] A. Vilenkin and E. P. S. Shellard. *Cosmic Strings and Other Topological Defects*. Cambridge University Press, 2000.
- [116] S. Vitale et al. Reconstruction of the gravitational wave signal in the virgo detector. *Phys. Rev. D*, 85:062002, 2012.
- [117] C. Wang et al. Low-vibration pulse tube cryocooler. *Cryogenics*, 47:574–580, 2007.
- [118] K. Yamamoto et al. Thermal noise reduction in cryogenic mirrors for interferometric gravitational wave detectors. *Phys. Rev. D*, 74:022002, 2006.